

CHARACTERIZATION OF CREEP AND MICROSTRUCTURE OF NOVEL HIGH-TEMPERATURE MAGNESIUM ALLOYS

by

Michelle Lynn Fletcher

B.Sc., The University of Calgary, 2010

THESIS SUBMITTED IN PARTIAL FULFILLMENT OF
THE REQUIREMENTS FOR THE DEGREE OF

MASTER OF APPLIED SCIENCE

in

The College of Graduate Studies

(Mechanical Engineering)

THE UNIVERSITY OF BRITISH COLUMBIA

(Okanagan)

April 2012

© Michelle Lynn Fletcher, 2012

Abstract

The desire for fuel efficient, yet high performance, vehicles in the automotive industry has resulted in a high demand for light weight structural materials. Magnesium alloys are one of the lightest structural materials available to engineering designers. Wrought magnesium alloy bars, sections and tubes have been used in the aerospace, electronics and automotive industries, where component weight is of concern. The operating temperature of these components is typically limited to below 100°C, since creep resistance begins to deteriorate above this temperature. Creep deformation in magnesium alloys has been generally contributed to grain boundary sliding and plastic deformation leading to inter-granular failure.

This research investigated the creep resistance of five wrought magnesium alloys (AE42, AJ32, AX30, EZ33 and ZE10) developed for elevated temperature automotive applications. Non-conventional techniques were utilized to study the creep resistance of these alloys on the micro and macro scale at temperatures ranging from 25°C to 175°C. Neutron diffraction techniques were utilized to measure alloy texture, total strain and elastic creep strain. Metallographic techniques were subsequently used to analyze microstructural constituents in each alloy. The alloy microstructure was then correlated to the alloy's creep resistance.

The results indicate that the aluminum free magnesium alloys (i.e., EZ33 and ZE10) had higher creep resistance compared to aluminum containing alloys (i.e., AE42, AJ32 and AX30). For the aluminum containing alloys, twinning and formation of a large amount of the $Mg_{17}Al_{12}$ intermetallic compound likely contributed to a decreased creep resistance. Strontium and calcium were both seen to limit $Mg_{17}Al_{12}$ formation, thus improving creep resistance of the AJ32 and AX30 alloys with respect to the AE42 alloy, respectively. Both the EZ33 and ZE10 alloys contained nanoprecipitates uniformly dispersed throughout the matrix, possibly contributing to dispersion strengthening and improved creep resistance. The results of neutron diffraction studies suggest that the aluminum containing alloys have experienced unique lattice structure changes on different crystallographic planes. In contrast, the aluminum free alloys had very stable crystallographic lattice strains throughout the duration of creep testing.

Table of Contents

Abstract	ii
Table of Contents	iii
List of Tables	vi
List of Figures	vii
Nomenclature	xii
Acknowledgements	xiv
Dedication	xv
1.0 Introduction	1
2.0 Literature Review	4
2.1 Background on Creep and Plastic Deformation Mechanisms	4
2.1.1 Effect of Slip and Twinning on Plastic Deformation	5
2.1.2 Effect of Grain Boundaries on Plastic Deformation	6
2.1.3 Effect of Precipitates on Plastic Deformation	7
2.1.4 Effect of Extrusion Process on Plastic Deformation	8
2.2 Creep Performance of Aluminum Containing Magnesium Alloys	8
2.2.1 Al-Mg Magnesium Alloys	8
2.2.2 Al-RE Magnesium Alloys	10
2.2.3 Al-Ca Magnesium Alloys	12
2.2.4 Al-Sr Magnesium Alloys	12
2.3 Creep Performance of Aluminum Free Magnesium-Rare Earth Alloys	14
3.0 Principles of Neutron Diffraction	17
4.0 Experimental Procedure	19
4.1 Material Selection	19
4.2 Neutron Diffraction	22
4.2.1 Neutron Diffraction Experimental Conditions	22
4.2.2 L3 Spectrometer Setup	23
4.2.3 Neutron Diffraction Experimental Procedure	26

4.2.4 Neutron Diffraction Data Analysis.....	30
4.3 Microscopy	31
4.3.1 Sample Preparation.....	31
4.3.2 Scanning Electron Microscopy.....	33
4.3.3 Optical Microscopy	36
5.0 Results and Discussion.....	40
5.1 Neutron Diffraction	40
5.1.1 Texture Evolution and Analysis	40
5.1.2 Total Creep Strain Measured Using an Extensometer.....	43
5.1.2.1 Comparison of Total Tensile-Creep Strain at 150°C to that at 175°C	43
5.1.2.2 Comparison of Total Tensile to Total Compressive-Creep Strain at 150°C	44
5.1.2.3 Comparison of Total Compressive-Creep Strain at 150°C to that at 175°C	46
5.1.2.4 Comparison of Total Tensile to Total Compressive-Creep Strain at 175°C	48
5.1.2.5 Summary of Total Strain Measurements	49
5.1.3 Elastic Creep Microstrain Measured Using Neutron Diffraction	50
5.1.3.1 Tensile-Creep Elastic Microstrain at 150°C and 175°C.....	50
5.1.3.2 Compressive-Creep Elastic Microstrain at 175°C.....	52
5.1.3.3 Summary of Elastic Microstrain Measurements.....	55
5.2 Metallographic Analysis.....	56
5.2.1 Grain Boundary Analysis Using Optical Microscopy	56
5.2.2 Subgrain Size Analysis Using Optical Microscopy.....	59
5.2.3 Twinning Analysis Using Optical Microscopy	61
5.2.4 Characterization of Intermetallic Compounds.....	65
5.2.4.1 Intermetallics in the AE42 Alloy.....	67
5.2.4.2 Intermetallics in the AJ32 Alloy.....	69
5.2.4.3 Comparison of Intermetallics in the AX30 Alloy to AE42 and AJ32 Alloys	72
5.2.4.4 Intermetallics in the ZE10 Alloy	73
5.2.4.5 Intermetallics in the EZ33 and ZE10 Alloys	76

5.2.5 Al Segregation Analysis Using SEM and Optical Microscopy	78
5.2.5.1 Segregation of Al in the AE42 Alloy	78
5.2.5.2 Segregation of Al in the AJ32 Alloy	85
5.2.5.3 Comparison of Al Segregation in AE42 and AJ32 Alloys	92
5.2.6 β -phase Analysis Using Optical Microscopy	93
5.2.7 Zn and Zr Segregation Analysis Using an SEM.....	96
6.0 Conclusions	100
6.1 Neutron Diffraction	100
6.2 Metallographic Analysis.....	100
6.3 Recommendations for Future Work	101
References	102
Appendices	106
Appendix A – Phase Diagrams.....	106
Appendix B – Optical Microscopy Routines.....	109
Appendix C – Metallographic Analysis	111
Appendix C.1 – Optical Microscopy	111
Appendix C.2 – Scanning Electron Microscopy	114
Appendix C.2.1 – General Microstructure	114
Appendix C.2.2 – AE42 Alloy Intermetallics	119
Appendix C.2.3 – AJ32 Alloy Intermetallics	122
Appendix C.2.4 – ZE10 Alloy Intermetallics.....	124

List of Tables

Table 1. Summary of testing performed for the AE42, AJ32, ZE10, EZ33 and AX30 alloys	21
Table 2. Nominal alloy compositions for AE42, AJ32, AX30, EZ33 and ZE10 [51].....	21
Table 3. Neutron diffraction sample dimensions before testing.....	26
Table 4. Theoretical diffraction angles for Mg.....	27
Table 5. Measured diffraction angles for ZE10 during neutron diffraction	28
Table 6. Glycol etchant composition.....	36
Table 7. Summary of the time required for alloy etching using glycol.....	36
Table 8. ANOVA analysis of the effect of alloy composition and creep on the alloy grain width ...	58
Table 9. ANOVA analysis of the effect of alloy composition and creep on the alloy subgrain sizes	61
Table 10. Theoretical twinning angles	64
Table 11. General morphology of intermetallic compounds in the AE42, AJ32, AX30, EZ33 and ZE10 alloys.....	65
Table 12. Raw data for average grain widths	112

List of Figures

Figure 1.	Specific plate bending stiffness of various structural materials [5]	1
Figure 2.	Scope of present research.....	3
Figure 3.	Mechanical twins in magnesium [3]	5
Figure 4.	Twinning in the AE42 alloy: a) Post-compressive creep and b) Post-tensile creep [9]	6
Figure 5.	Mg-Al phase diagram [35].....	9
Figure 6.	β -phase in the AZ91 alloy post-creep [33].....	10
Figure 7.	Mg-Nd phase diagram [38]	11
Figure 8.	AE42 alloy microstructure with Al-RE-Mn particulates (A) and $Al_{11}RE_3$ intermetallics (B) [9]	11
Figure 9.	Mg-Sr phase diagram [44]	13
Figure 10.	SEM micrographs of various Mg alloys: a) AJ51, b) AJ52, c) AJ62 and d) AJ62L [47]	13
Figure 11.	Microstructure of as-extruded AJC421 alloy: a) Bulk grain structure and b) Mg-Al-Sr intermetallic phase [25]	14
Figure 12.	Mg-Zn phase diagram [49].....	15
Figure 13.	SEM micrograph of EZ33 intermetallic morphology [51].....	16
Figure 14.	Micrographs depicting: a) Nanoparticle dispersion in EZ alloy, b) Dispersed nanoparticles and c) Precipitates along grain boundaries [52]	16
Figure 15.	Neutron diffraction schematic.....	18
Figure 16.	Tensile-creep strain for the AE42, AE33, AX30, AZX310, AJ32, ZE10 and EZ33 alloys at 150°C and 175°C [51].....	19
Figure 17.	Tension-compression asymmetry in resistance to creep for the AE42, AE33, AX30, AZX310, AJ32, ZE10 and EZ33 alloys at 150°C [51].....	20
Figure 18.	Dimensions of samples used for compressive strain measurement using neutron diffraction	22
Figure 19.	L3 spectrometer setup for neutron diffraction testing.....	23
Figure 20.	Neutron diffraction incident and diffracted beam paths.....	24
Figure 21.	Neutron diffraction compression apparatus	24
Figure 22.	Specimen setup for neutron diffraction testing	25
Figure 23.	Extensometer calibration: voltage vs. displacement	27
Figure 24.	Neutron count vs. diffraction angle.....	28
Figure 25.	Compressive creep testing experimental conditions performed during neutron diffraction	29
Figure 26.	Neutron count vs. diffraction angle (with outlier data points)	30

Figure 27. Profile of applied load and temperature during neutron diffraction testing. Corresponding experiment steps are presented in Figure 25	31
Figure 28. As-extruded alloy samples: a) Torus and b) Sample surfaces examined	32
Figure 29. Post-creep alloy samples: a) Machined sample, b) Cross-section and c) Radial section	32
Figure 30. Representative example of the mounted and polished sample.....	33
Figure 31. The SEM chamber of the Tescan MIRA3 XMU SEM	34
Figure 32. Examples of XEDS analysis: a) Point and area scans, b) Linescans and c) Smartmaps..	35
Figure 33. AE42 alloy micrographs in the: a) Bright field and b) DIC modules	37
Figure 34. Cross-section of the AE42 alloy (100x magnification): a) Captured and b) Delineated.	37
Figure 35. Grain boundaries and matrix in the AE42 alloy cross-section.....	38
Figure 36. Location of grain width measurements in the AE42 alloy (100x magnification)	38
Figure 37. Representative example of subgrain measurements in the ZE10 alloy: a) Captured micrograph and b) Measurements	39
Figure 38. Twinning measurements in the AJ32 alloy: a) Captured micrograph and b) Measurements	39
Figure 39. $\{1010\}$ pole figures for the: a) AE42 alloy and b) EZ33 alloy [51].....	40
Figure 40. $\{0002\}$ pole figures for the AE42, AJ32, AX30 and EZ33 alloys [55]	41
Figure 41. Texture evolution in the $\{1010\}$ reflection for the AE42, AJ32, AX30 and EZ33 alloys: a) As-extruded, b) Post compression-creep at 150°C and c) Post tensile- creep at 175°C conditions [55]	42
Figure 42. Tensile-creep strain vs. time at: a) 150°C and b) 175°C for the AE42, AX30, AJ32, ZE10 and EZ33 alloys.....	44
Figure 43. Total strain vs. time at 150°C under: a) Tensile loading and b) Compressive loading for the AE42, AX30, AJ32, EZ33 and ZE10 alloys	45
Figure 44. Total compressive-creep strain vs. time at: a) 150°C and b) 175°C for the AE42, AJ32 and ZE10 alloys	47
Figure 45. Onset of secondary creep in the AJ32 alloy	48
Figure 46. Total creep strain vs. time at 175°C for AE42, AJ32 and ZE10 alloys: a) Tensile creep and b) Compressive creep	49
Figure 47. Normalized creep strains of the AX30, AJ32, ZE10 and EZ33 alloys with respect to the AE42 alloy.....	50
Figure 48. In-situ strain evolution for $\{1010\}$ crystallographic plane in: a) AE42 alloy and b) The EZ33 alloy [51]	51
Figure 49. The $\{1012\}$, $\{0002\}$ and $\{2110\}$ microstrain in the AE42 alloy	52

Figure 50. Lattice strains for the {1010}, {1011} and {2110} planes for the: a) AE42 alloy, b) AJ32 alloy and c) ZE10 alloy.....	54
Figure 51. Representative microstructure in: a) Cross-section direction and b) Radial direction (AJ32 alloy at 50x magnification).....	56
Figure 52. Representative micrographs for the cross-section samples of the: a) AE42 alloy, b) AJ32 alloy, c) AX30 alloy, d) EZ33 alloy and e) ZE10 alloy.....	57
Figure 53. Average grain widths for the AE42, AJ32, AX30, EZ33 and ZE10 alloys in their as-extruded and post-creep conditions	58
Figure 54. Subgrains in the as-extruded: a) AE42 alloy, b) AJ32 alloy, c) AX30 alloy, d) EZ33 alloy and e) ZE10 alloy	60
Figure 55. Average subgrain radii in the AE42, AJ32, AX30, EZ33 and ZE10 alloys in their as-extruded and post-creep conditions	61
Figure 56. As-extruded and post-creep twinning in the: a) AE42 alloy, b) AJ32 alloy, c) AX30 alloy and d) EZ33 alloy	62
Figure 57. Twinning angles relative to extrusion direction in the AE42, AJ32 and AX30 alloys	63
Figure 58. General microstructure of the: a) AE42 alloy, b) AJ32 alloy, c) AX30 alloy, d) EZ33 alloy and e) ZE10 alloy (500x magnification)	66
Figure 59. SEM micrographs of the intermetallics in the as-extruded AE42 alloy.....	67
Figure 60. SEM micrographs of the intermetallics in the post-creep AE42 alloy.....	68
Figure 61. SEM micrographs of the intermetallics in the as-extruded AJ32 alloy.....	69
Figure 62. SEM micrograph of Al ₅ Sr ₃ in the as-extruded AJ32 alloy.....	70
Figure 63. SEM micrographs of the intermetallics in the post-creep AJ32 alloy.....	71
Figure 64. SEM micrograph showing fracturing of Al ₅ Sr ₃ in the post-creep AJ32 alloy.....	72
Figure 65. General microstructure of the as-extruded: a) AE42 alloy, b) AJ32 alloy and c) AX30 alloy	73
Figure 66. SEM micrographs of the intermetallics in the as-extruded ZE10 alloy	74
Figure 67. SEM micrograph of the Zr ₃ Si nanoprecipitate in the ZE10 alloy	75
Figure 68. SEM micrograph of the Zn ₄ RE nanoprecipitate in the ZE10 alloy.....	75
Figure 69. SEM micrographs of the intermetallics in the post-creep ZE10 alloy	76
Figure 70. General microstructure of the as-extruded: a) EZ33 alloy and b) ZE10 alloy	77
Figure 71. Nanoprecipitate flow bands in the: a) As-extruded and b) Post-creep EZ33 alloy	78
Figure 72. XEDS maps of as-extruded AE42 alloy: a) SEM micrograph and b) Elemental maps ...	79
Figure 73. Fibrous β-phase in the as-extruded AE42 alloy.....	80
Figure 74. Al segregation in the as-extruded AE42 alloy showing the: a) Location of the linescan and b) Atomic composition along the linescan	81

Figure 75. XEDS maps of post-creep AE42 alloy: a) SEM micrograph and b) Elemental maps	82
Figure 76. Fibrous β -phase in the post-creep AE42 alloy	83
Figure 77. Al segregation in post-creep AE42 alloy showing the: a) Location of the linescan and b) Atomic composition	84
Figure 78. Comparison of the Al segregation in the as-extruded and post-creep AE42 alloy showing the: a) Peak:background ratio and b) Al band width.....	85
Figure 79. XEDS maps of as-extruded AJ32 alloy: a) SEM micrograph and b) Elemental maps	86
Figure 80. Al segregation in as-extruded AJ32 alloy showing the: a) Location of the linescan and b) Atomic composition	87
Figure 81. Absence of β -phase in the as-extruded AJ32 alloy	88
Figure 82. Post-creep AJ32 alloy: a) SEM micrograph and b) Elemental maps.....	89
Figure 83. Fibrous β -phase in the post-creep AJ32 alloy	90
Figure 84. Al segregation in post-creep AJ32 alloy showing the: a) Location of the linescan and b) Atomic composition	91
Figure 85. Comparison of the Al segregation in the as-extruded and post-creep AJ32 alloy showing the: a) Peak:background ratio and b) Al band width.....	92
Figure 86. Peak and background Al At% for the AE42 and AJ32 alloy in their as-extruded and post-creep conditions.....	93
Figure 87. β -phase in the: a) AE42 alloy, b) AJ32 alloy and c) AX30 alloy	94
Figure 88. Location of β -phase in the: a) AE42 alloy, b) AJ32 alloy and c) AX30 alloy	95
Figure 89. Formation of β -phase along subgrain boundaries in the AE42 alloy.....	96
Figure 90. Solute segregation of Zr in the ZE10 alloy: a) As-extruded and b) Post-creep	97
Figure 91. Zn and Zr segregation in as-extruded ZE10 showing the: a) Location of linescan and b) Atomic composition	98
Figure 92. Segregation in ZE10 alloy: a) Zr and b) Zn	99
Figure 93. Mg-Ce phase diagram [46].....	106
Figure 94. Mg-La phase diagram [46].....	107
Figure 95. Mg-Pr phase diagram [40]	108
Figure 96. Buehler OmniMet routine for alloy grain width	109
Figure 97. Buehler OmniMet routine for intermetallic area percent	110
Figure 98. As-extruded and post-creep microstructure of AE42 (500x magnification).....	114
Figure 99. As-extruded and post-creep microstructure of AJ32 (500x magnification).....	115
Figure 100. As-extruded microstructure of AX30 at 500x and 1000x magnification.....	116
Figure 101. As-extruded microstructure of EZ33 at 500x and 1000x magnification.....	117
Figure 102. As-extruded and post-creep microstructure of ZE10 at 500x magnification	118
Figure 103. Structure of Al1RE3 in the as-extruded AE42 alloy.....	119

Figure 104. Structure of Al ₆ Mn ₃ RE in the as-extruded AE42 alloy	120
Figure 105. Structure of the post-creep intermetallics in the AE42 alloy	121
Figure 106. Structure of the as-extruded intermetallics in the AJ32 alloy	122
Figure 107. Structure of the post-creep intermetallics in the AJ32 alloy	123
Figure 108. Structure of the as-extruded intermetallics in the ZE10 alloy.....	124
Figure 109. Structure of the post-creep intermetallics in the ZE10 alloy.....	125

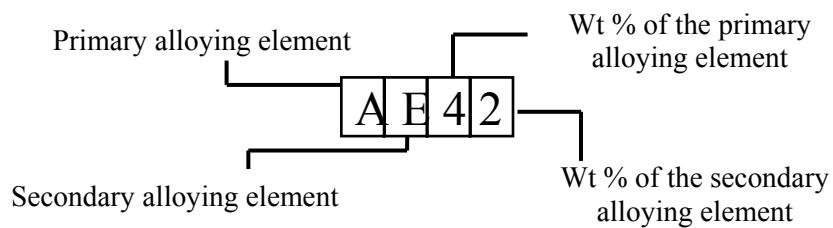
Nomenclature

Symbol	Definition
d	Atomic lattice spacing
d_0	Initial atomic lattice spacing
D	Sample diameter
ε	Creep strain
E	Elastic modulus
λ	Neutron wavelength
n	Neutron diffraction order
ν	Poissons ratio
\emptyset	Twinning angle
φ	Analyzer orientation angle
σ	Applied stress
θ	Neutron scattering angle
θ_m	Monochromating crystal orientation angle

Element	Definition
Al	Aluminum
C	Carbon
Ca	Calcium
Ce	Cerium
La	Lanthanum
Mg	Magnesium
Mn	Manganese
Nd	Neodymium
Pr	Praseodymium
Si	Silicon
Sr	Strontium
Zn	Zinc
Zr	Zirconium

Acronyms	Definition
<i>ANOVA</i>	Analysis of Variance
<i>DIC</i>	Differential Interference Contrast
<i>EBSD</i>	Electron Backscatter Diffraction
<i>HCP</i>	Hexagonal Close-Packed
<i>NRC-CNBC</i>	National Research Council-Canadian Neutron Beam Center
<i>NRU</i>	National Research Universal
<i>RE</i>	Rare Earth element
<i>SEM</i>	Scanning Electron Microscope
<i>XEDS</i>	X-Ray Energy Dispersive Spectroscopy

Alloy Nomenclature



Element	Alloy Nomenclature
<i>Aluminum</i>	A
<i>Rare Earths</i>	E
<i>Calcium</i>	X
<i>Strontium</i>	J
<i>Zinc</i>	Z

Acknowledgements

I first wish to acknowledge my supervisor, Dr. Bichler, who provided me with excellent guidance and assistance throughout my research. Through his guidance I was able to thrive as a graduate student, expanding upon my research and literary skills. I will forever appreciate the support he has given me throughout my studies.

I would also like to thank Dr. Sediako from the Canadian Neutron Beam Center – National Research Council Canada, for his supervision, guidance and support of my research and especially my neutron diffraction testing. His knowledge and support was invaluable.

I would like to also acknowledge Mr. Shook from Applied Magnesium International for providing materials and resources for my research.

In addition, I would like to thank Dr. Klassen from the University of Western Ontario for his collaboration throughout my research.

I sincerely appreciate the assistance and guidance of Dr. Milani throughout my research, especially in assisting my results analysis and interpretation.

I would also like to sincerely thank Ms. Siebert-Timmer and Mr. Porritt for their excellent assistance in data collection and literature review.

Finally, I would like to thank my friends and family for their care and support, without which I would not have been able to complete my research.

Dedication

I dedicate this to my family: Ray, Lynn, Dan and Brian

I could not have done this without your love and support.

1.0 Introduction

The recent efforts to enhance the fuel efficiency of vehicles, while maintaining their performance, have resulted in a renewed interest and vigorous research in light weight structural materials. As a result, magnesium (Mg) alloys have received much attention over the past decades as a potential material of choice to significantly reduce vehicle weight. Magnesium alloys are ~30% lighter than aluminum (Al) alloys, and 70% lighter than steel. As a result, magnesium alloys have a desirable and high stiffness to weight ratio (Figure 1), thus being attractive for many structural components [1]. Mg is also the 8th most abundant element on the Earth, is easy to machine and is potentially recyclable [2]. In the 1930's, Volkswagen was one of the first to use Mg in their automobiles [4]. Today, for example, Mg alloys are used as the steering wheel core for the Toyota Camry, in the seat support for Jaguars and for the cam cover in the Ford Zetec [5].

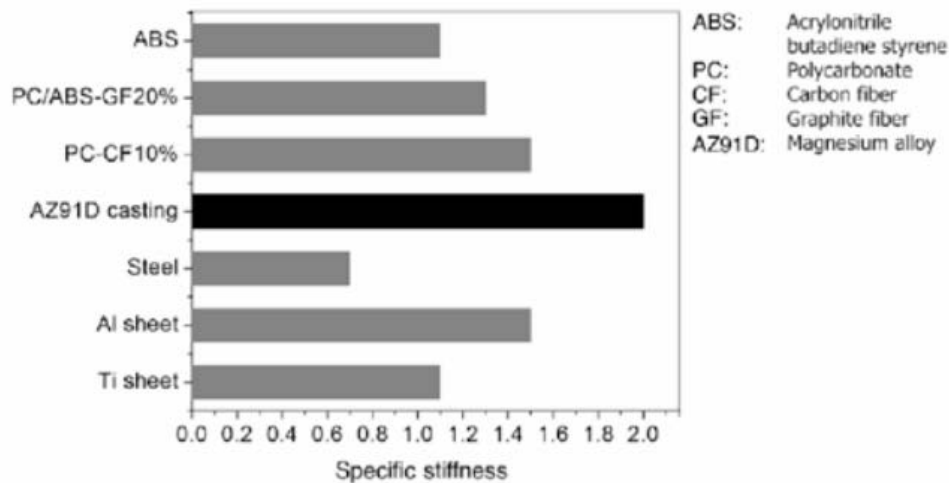


Figure 1. Specific plate bending stiffness of various structural materials [5]

The primary challenge with utilizing more Mg alloys in vehicles stems mainly from their relatively high cost (~50% higher than that of aluminum alloys) and their poor creep resistance above 120 °C. The loss of strength at elevated temperatures has been attributed to grain boundary movement and plastic deformation, which ultimately lead to inter-granular failure [4]. Enhancing the creep resistance of magnesium alloys has therefore been the subject of intense international research efforts [3]. Primarily, industrial and scientific studies focused on manipulation of alloy composition with a view of enhancing creep resistance.

Current commercial Mg alloys are classified into two categories: i) magnesium alloys containing aluminum, and ii) magnesium alloys free of aluminum [4]. Aluminum, zinc, rare earth metals, strontium and calcium have been some of the most significant alloying elements to influence creep resistance of Mg alloys. As a result, this thesis research focused on the characterization of

representative magnesium alloys containing these elements. Specifically, the creep resistance of the AE42, AJ32, AX30, EZ33 and ZE10 alloys was investigated.

The AE42 alloy is currently the industrial benchmark for creep resistant Mg alloys. The AJ32 and AX30 alloys were created to examine the effect of adding strontium and calcium to aluminum-containing magnesium alloys, while the EZ33 and ZE10 alloys both contain zinc and rare earth metals, without any addition of aluminum in the alloy system.

Conventional creep tests usually measure dimensional changes of a material with respect to time under a constant applied stress at elevated temperatures. Although this method measures the total material deformation, it fails to provide detailed information on elastic and plastic contributions, which are needed in order to understand the fundamental mechanisms behind alloy's creep resistance. In this research, neutron diffraction was utilized to quantify the elastic and plastic strain evolution during creep testing. Metallographic analysis was also performed to relate the effect of microstructure characteristics to the material's creep resistance. Thus, the objectives of this thesis were to study five magnesium alloys (AE42, AJ32, AX30, EZ33 and ZE10) and their behaviour during compressive creep testing using neutron diffraction techniques, coupled with an analysis of their microstructural constituents, to analyze the fundamental mechanisms behind the creep resistance of these five alloys.

The structure of this thesis document is as follows:

Chapter 2 presents a comprehensive literature review of fundamental mechanisms influencing material creep, followed by a review of literature pertinent to the alloys under investigation in this research.

Chapter 3 presents the theory of neutron diffraction.

Chapter 4 provides the details of experiments carried out in this research. Details of material selection, neutron diffraction and microscopy analyses are presented.

The results are presented and discussed in Chapter 5.

Chapter 6 presents the final conclusions of this research, while the recommendations for future work are summarized in Chapter 7.

A schematic of the scope of this research is provided in Figure 2.

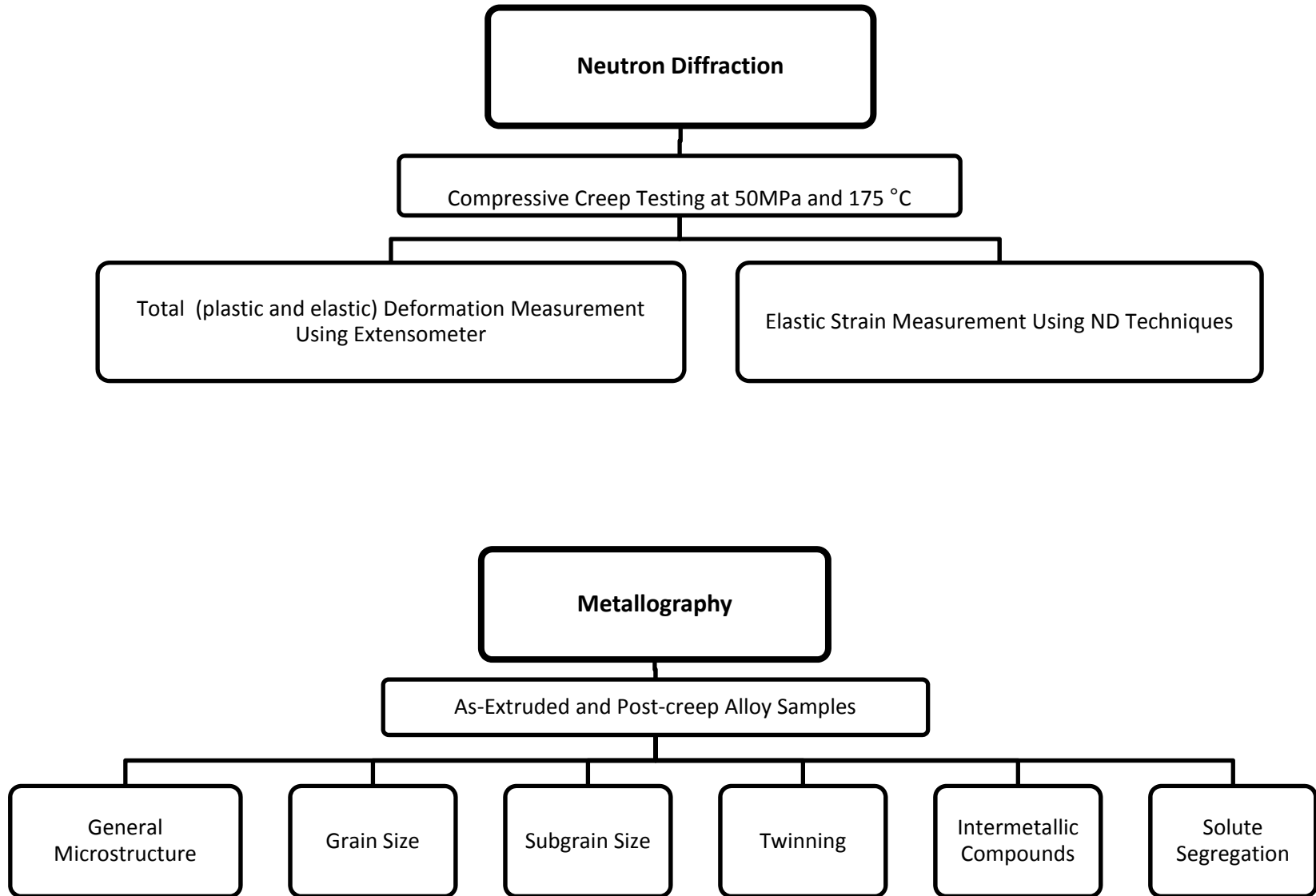


Figure 2. Scope of present research

2.0 Literature Review

A general background briefly summarizing the fundamental creep mechanisms pertinent to this research are introduced. This is followed by a review of the literature available on the AE42, AJ32, AX30, EZ33 and ZE10 alloys, which were the focus of this thesis.

2.1 Background on Creep and Plastic Deformation Mechanisms

Creep represents time-dependent plastic deformation of a material subjected to a constant load at elevated temperature [7, 1]. Creep is affected by a material's microstructural properties, such as grain size, subgrain size, intermetallic compounds, as well as the creep strain rate and environment temperature.

Creep deformation occurs at elevated temperatures due to an increase in atom mobility and diffusion. Classical theories of creep attribute high-temperature plastic deformation to dislocation glide, dislocation creep and grain boundary sliding. These processes are competitive in nature, but may also occur simultaneously. At temperatures above approximately half of the melting temperature the dominating creep mechanism may be dislocation creep or diffusional flow, depending upon the applied stress level [6].

Creep tests usually measure dimensional changes of a material with respect to time under a constant applied stress and temperature. For example, the standard procedures for creep testing of Mg alloys are available in ASTM E139-70 [1, 7]. Based on industrial considerations, the duration of a creep test should range from several months to years. However, to apply constant stress and temperature accurately for extended periods of time requires extensive lab equipment and expenditures. Consequently, a variety of non-standard creep experiments were developed to obtain the creep strain vs. time data in order to help understanding of the fundamental mechanisms responsible for creep.

The creep strain versus time plot consists of primary, secondary and tertiary creep regions. Primary creep is generally elastic (i.e., recoverable) and results in a rapid deformation of the material, followed by a steadily decreasing strain rate due to microstructural changes. Primary creep deformation does not tend to be homogeneous across the material and may result in localized subgrain formation and/or grain boundary sliding. The stress levels and temperature ultimately control the size of the subgrains (i.e., high temperature and low stress results in a large subgrain formation). The newly formed subgrains remain in the material during secondary creep until general recrystallization takes place. Secondary creep is represented by a steady-state creep rate and this rate

is independent of time. Tertiary creep consists of the sudden increase in strain rate, followed by material failure [1].

During creep of magnesium alloys, several plastic deformation processes may be activated. These include slip, twinning or grain boundary sliding. The fundamental aspects of these mechanisms are discussed next.

2.1.1 Effect of Slip and Twinning on Plastic Deformation

Magnesium with its HCP crystal structure is known to have only a limited number of slip systems. In general, slip may occur on the basal, prism, 1st order pyramidal and 2nd order pyramidal planes, and most readily takes place on the close-packed planes (ie., the (0001) basal plane), followed by secondary slip on the (10 $\bar{1}$ 1) planes [4]. In cases when crystal orientation is not favorable for slip, twinning may occur [8]. Thus, twinning and slip deformation are competitive processes [6, 7]. However, twinning effectively changes the local crystal orientation by creating a mirror lattice with respect to the twin plane. Similar to slip, twinning in HCP crystals takes place on preferred planes. For Mg, twinning tends to occur on the (10 $\bar{1}$ 2) plane in the $\langle\bar{1}011\rangle$ direction [6, 7, 10, 11, 12], followed by twinning on (10 $\bar{1}$ 1) plane [10]. The total deformation due to twinning alone tends to be small; however, reorientation of the crystal lattice may result in favorable re-orientation of grains for slip, resulting in subsequent accelerated slip deformations.

Mechanical twins resulting from shock loading at low temperatures have a lens shape, as seen in Figure 3 [7], while slow strain rates produce thicker twins. Twins usually terminate at grain boundaries or at secondary phases due to the change in crystal orientation and structure, respectively [4, 7].



Figure 3. Mechanical twins in magnesium [3]

An example of twinning in a die-cast AE42 magnesium alloy at 200°C under a 60 MPa load is illustrated in Figure 4. It was noted, that cyclic loading of the alloy resulted in multiple twinning on primary and secondary twin planes. With respect to creep performance, creep testing of pure Mg has shown that at temperatures between 90 and 300°C, with applied stresses ranging from 8-10 MPa, plastic deformation is accommodated by slip on the basal plane followed by twinning and subgrain formation. Additional non-basal slip was also initiated above 250°C on prismatic and pyramidal planes [14].

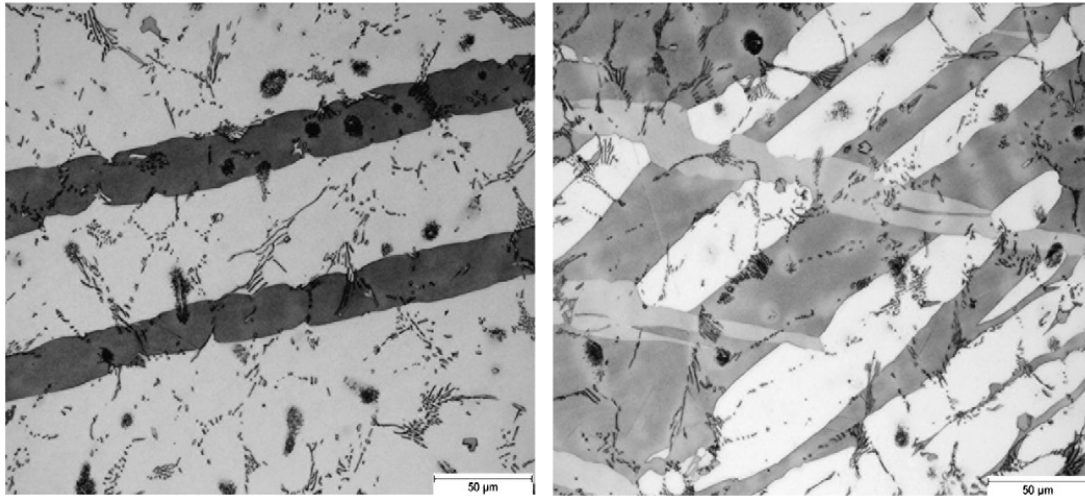


Figure 4. Twinning in the AE42 alloy: a) Post-compressive creep and b) Post-tensile creep [9]

The magnitude of plastic deformation due to slip or twinning can be manipulated by controlling the grain morphology or composition of an alloy. Specifically, introducing obstacles to dislocation motion via formation of high angle grain boundaries, or by the formation of uniformly dispersed precipitates, may significantly reduce plastic deformation of a material.

2.1.2 Effect of Grain Boundaries on Plastic Deformation

For materials operating in room temperature environments, a fine grain size is desirable. A fine grain size results in a high volume of grain boundaries, which effectively act as a crystallographic barrier to dislocation movement. The effect of grain size on the strength of materials has been extensively studied and is well described by the classical Hall-Petch relationship. However, when a material is exposed to elevated temperature and reaches the equicohesive temperature (approximately half of the melting temperature), grain boundary sliding may be initiated and enables significant plastic deformation of the material [7]. Since a fine grain size would allow for greater relative movement of grains, materials operating in elevated temperature environments usually have a large grain size. The strain attributed to grain boundary sliding during creep can range from 1-50% of the total strain depending on material conditions and applied loads [7, 13].

A special case of grain boundaries are so-called subgrains, which form within a larger grain by having a crystallographic lattice misalignment by only a few degree offset with respect to the parent grain. Factors that affect subgrain formation include the amount of material's plastic deformation, rate of deformation and the duration of exposure to elevated temperature environment [7]. For example, one of the most common mechanisms responsible for subgrain formation is 1-10% tensile strain followed by annealing heat treatment. The annealing heat treatment rearranges the dislocations into subgrain boundaries. A second mechanism of subgrain formation is activated at high strain rates, wherein subgrains are formed in areas of inhomogeneous deformation. These subgrains may form from fractured grain boundaries, twinning boundaries, inclusions or secondary phases [7].

Subgrain formation and dislocation movement may result in strain hardening of the material during creep. In Mg alloys, precipitation of second phase particles also frequently contributes to strain hardening and modification of the creep response of an alloy [17].

2.1.3 Effect of Precipitates on Plastic Deformation

Strain hardening occurs when dislocations accumulate around precipitates in an alloy and prevent additional material slip [6, 7]. The precipitates may form in-situ during alloy solidification, or may be externally introduced into the material. Depending on the properties of the precipitates (e.g., their hardness or melting temperature) they may be able to bare a significant portion of the stress applied to the material. While this strengthening mechanism is frequently used to enhance the room temperature alloy mechanical properties, it also remains effective even at moderate elevated temperatures. For example, nanoscale calcium-based reinforcements added to the AZ91 magnesium alloy were seen to enhance creep resistance of the alloy at 150 °C by a factor of 100 [14, 17, 28, 29]. In contrast, formation of $Mg_{17}Al_{12}$ precipitates along grain boundaries in aluminum containing magnesium alloys is known to accelerate grain boundary sliding. In these alloys, the activation energy for grain boundary sliding became so low due to the presence of the precipitates, that this deformation process dominated the entire creep behavior of the alloy [16]. Clearly, formation of precipitates must be judiciously controlled to achieve the desired alloy properties.

Presence of precipitates in a material may give rise to the formation of dislocation accumulations which oppose additional slip. Due to requirements of mechanical equilibrium, a back stress is created on the opposing side of the precipitates. When stress is applied in the direction of the back stress, the yield stress of the material is reduced due to the back stress now contributing to the applied stress, causing strain softening of the material. This phenomenon is often referred to as the Bauschinger effect [7, 19]. The Bauschinger effect has been frequently observed in extruded Mg alloys due to their uni-directional deformation during extrusion [20].

2.1.4 Effect of Extrusion Process on Plastic Deformation

Extrusion is the process of forcing a material through a die to reduce the material cross-section and give it a desired shape. A large force is required to extrude material at room temperature and therefore, in industry, extrusion is usually performed at high temperatures where there is a lower resistance to deformation [7, 22]. Multiple studies have found that hot extrusion increases the tensile creep properties in Al containing Mg alloys because the matrix undergoes dynamic recrystallization [23, 24, 25, 26]. However, it is recognized that mechanical processing alone (e.g., by strain hardening) is not able to sufficiently enhance the creep resistance of magnesium alloys. Consequently, alloying routes were developed to introduce thermally stable precipitates into the magnesium alloys in order to enhance their creep resistance.

2.2 Creep Performance of Aluminum Containing Magnesium Alloys

Aluminum containing magnesium alloys are currently the most industrially-relevant magnesium alloys. They exhibit excellent castability and room temperature strength. The presence of aluminum in these magnesium alloys has a two-fold effect: i) Aluminum enhances the room temperature strength via precipitation hardening, and ii) Aluminum reduces the high temperature strength due to formation of $Mg_{17}Al_{12}$ (β) phase which accelerates grain boundary sliding. As a result, aluminum containing alloys have been traditionally developed for environment-specific applications. A review of available literature on the main alloy groups is presented in this section, followed by a discussion of Aluminum free magnesium alloys (Section 2.3).

2.2.1 Al-Mg Magnesium Alloys

The addition of Aluminum to Mg alloys has been widely studied due to the commercial relevance of these alloys. Al addition increases alloy castability, ductility and strength at room temperature [3, 4, 17]; however, the tensile strength is lost above 120°C [3]. The drop in strength has been attributed to dislocation climb and the presence of $Mg_{17}Al_{12}$ intermetallic compound (β -phase) along the grain boundaries. Also, the β -phase has a relatively low incipient melting temperature, thus it is the first alloy constituent that transforms during high temperature exposure [14, 31, 32, 33]. Further, at elevated temperatures, the β -phase coarsens which further accelerates dislocation movement [34]. The phase diagram of Mg-Al alloys (Figure 5) shows that the detrimental β -phase forms when as little as 1 wt% of aluminum is present [35].

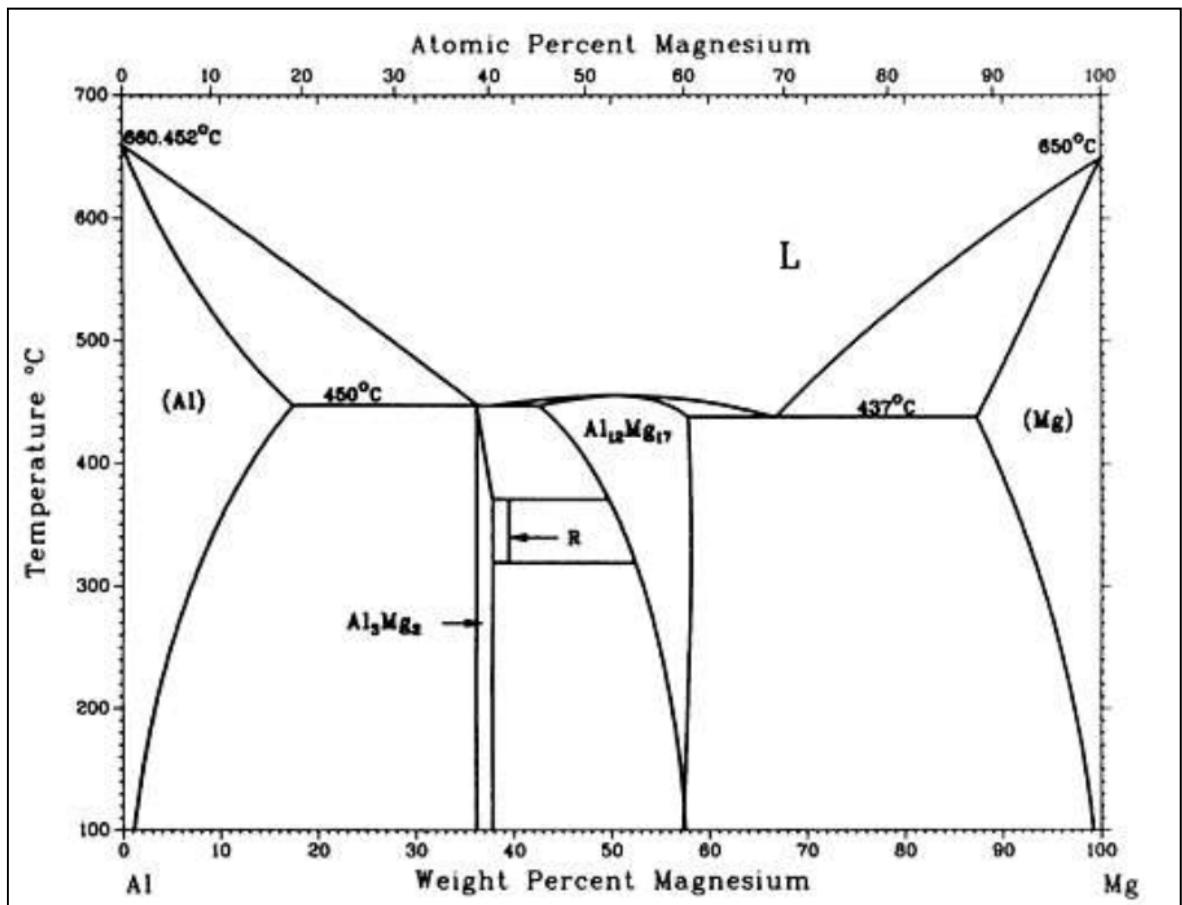


Figure 5. Mg-Al phase diagram [35]

The eutectic β -phase usually forms as a lamellar structure along grain boundaries, as can be seen in Figure 6 [18, 33]. In some studies on the AE42 alloys, the β -phase was not found at room temperature, but formed at higher temperatures (175°C) along the grain boundaries where Al saturation in the matrix was high [18, 36]. In this study, the mobility of Al in the matrix at elevated temperatures was determined to be critical for the alloy's performance. Therefore, decreasing the formation of β -phase in Al containing alloys will result in an increase in alloy creep resistance [14, 15].

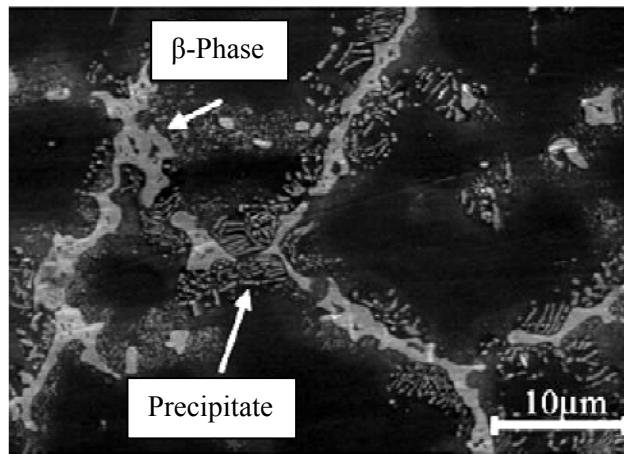


Figure 6. β -phase in the AZ91 alloy post-creep [33]

2.2.2 Al-RE Magnesium Alloys

The addition of rare earth elements (REs) such as cerium (Ce), lanthanum (La), neodymium (Nd) and praseodymium (Pr), to aluminum containing magnesium alloys was seen to significantly increase creep resistance. The Mg-Nd phase diagram is shown in Figure 7, while the phase diagrams for Mg-Ce, Mg-La and Mg-Pr are given in the appendix (Figure 93, Figure 94 and Figure 95). The increase in creep resistance due to REs addition has been attributed to the formation of thermally stable intermetallic compounds along the grain boundaries [32]. The low solubility of REs in Mg results in the formation of $(Mg,Al)_xRE_y$ intermetallic, which decreases the Al saturation in the matrix, thus decreasing the possibility of undesirable β -phase formation [14, 15, 36, 37].

The formation of the $Al_{11}RE_3$ (or Al_4RE) intermetallic compound is known to increase alloy creep resistance. $Al_{11}RE_3$ may be typically found along grain boundaries and has an acicular morphology, as seen in Figure 8. Moreover, with a melting temperature of approximately 1200°C, the $Al_{11}RE_3$ is one of the most thermally stable phases in the alloy, and remains effective in grain pinning at temperatures up to 150°C [15, 33, 39]. The high Al:RE ratio in this intermetallic compound also makes it very effective at decreasing the Al concentration in the matrix. However, $Al_{11}RE_3$ begins to degrade above 150°C after long high temperature exposures, with a concomitant release of Al and subsequent formation of the undesirable β -phase and metastable Al_2RE phase [36, 40].

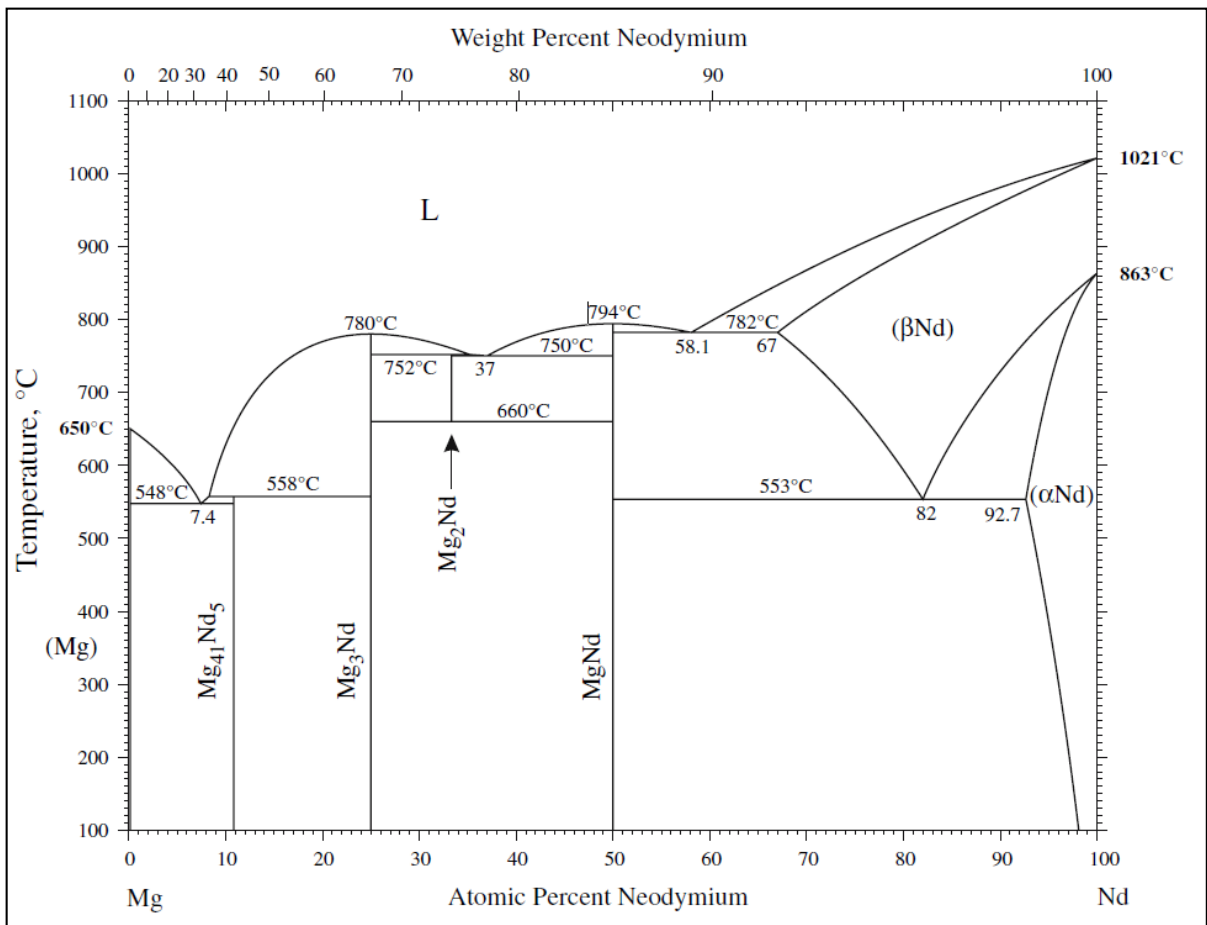


Figure 7. Mg-Nd phase diagram [38]

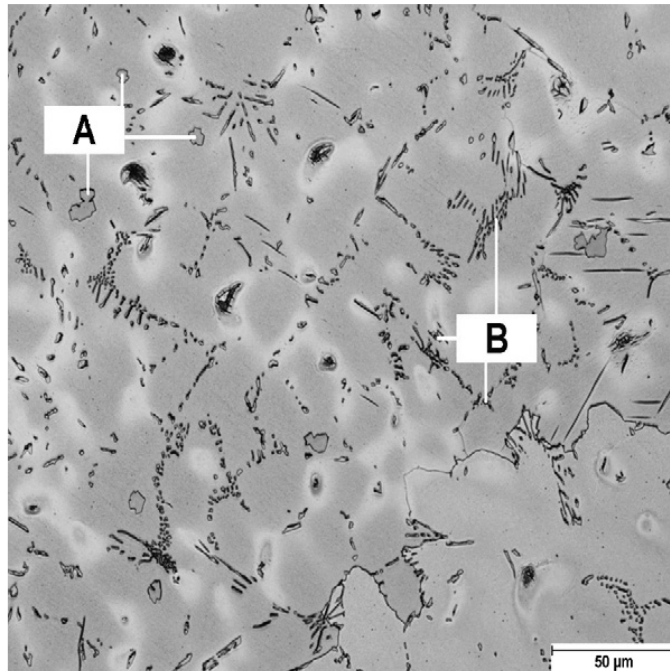


Figure 8. AE42 alloy microstructure with Al-RE-Mn particulates (A) and Al₁₁RE₃ intermetallics (B) [9]

The $Al_{11}RE_3$ phase is also sensitive to the strain rate experienced during material loading. Extensive fragmentation resulting from high creep strain rates or rapid extrusion processing was observed [26, 33, 39].

Specific to the AE42 alloy considered in this research, literature suggests that particulate and lamellar Al-RE intermetallics form concurrently [40]. The lamellar intermetallic particles consist of $Al_{11}RE_3$ and the particulate compounds are Al_2RE [15]. The $Al_{11}RE_3$ compounds have a La:Nd ratio higher than 0.7, whereas the Al_2RE particles have a La:Nd ratio less than 0.7 [36].

2.2.3 Al-Ca Magnesium Alloys

Adding calcium (Ca) to Al containing Mg alloys is known to increase alloy tensile strength, hardness, castability, resistance to oxidation and eutectic temperature, while decreasing alloy density [4]. Adding Ca promotes grain refinement and dynamic recrystallization through thermo-mechanical treatment [39]. Ca addition also increases creep resistance by raising the interdendritic volume fraction of thermally stable compounds, such as Mg_2Ca and Al_2Ca [26, 33, 41, 42]. Grain boundary sliding is the primary creep mechanism in Al-Ca alloys [43, 44].

The formation of lamellar Al_2Ca decreases the available Al for the formation of β -phase, thus enhancing the creep resistance of Al-Ca alloys [42, 43, 45]. Al_2Ca compounds are thermally stable and don't fragment during creep testing up to 150°C [28, 33]. Further, the Al_2Ca intermetallic compound is known to hinder dislocation annihilation and dislocation recovery at grain boundaries, thereby further contributing to the alloy's creep resistance [46]. However, Al_2Ca compounds break up during extrusion to form ultrafine particles along the grain boundaries [23, 26, 28].

2.2.4 Al-Sr Magnesium Alloys

Adding strontium (Sr) to Al containing Mg alloys promotes grain refinement and dynamic recrystallization through thermo-mechanical treatment [39]. The Mg-Sr phase diagram can be seen in Figure 9. The addition of Sr results in the creation of Mg-Al-Sr intermetallic compounds [47], which decreases the available Al in the matrix for the formation of β -phase and therefore increases the alloy creep resistance [25, 40, 47].

Typically, the intermetallic compounds that form in the Al-Sr alloys consist of lamellar, divorced and/or massive eutectic structures, as seen in Figure 10 [23, 25]. Al_4Sr was found in both lamellar and divorced structures in AJ62 and AJ52 alloys, whereas Al_3Sr had a massive eutectic structure [40, 47]. After creep testing at 175°C, these intermetallics show no visible morphological change, indicating their thermal stability [25].

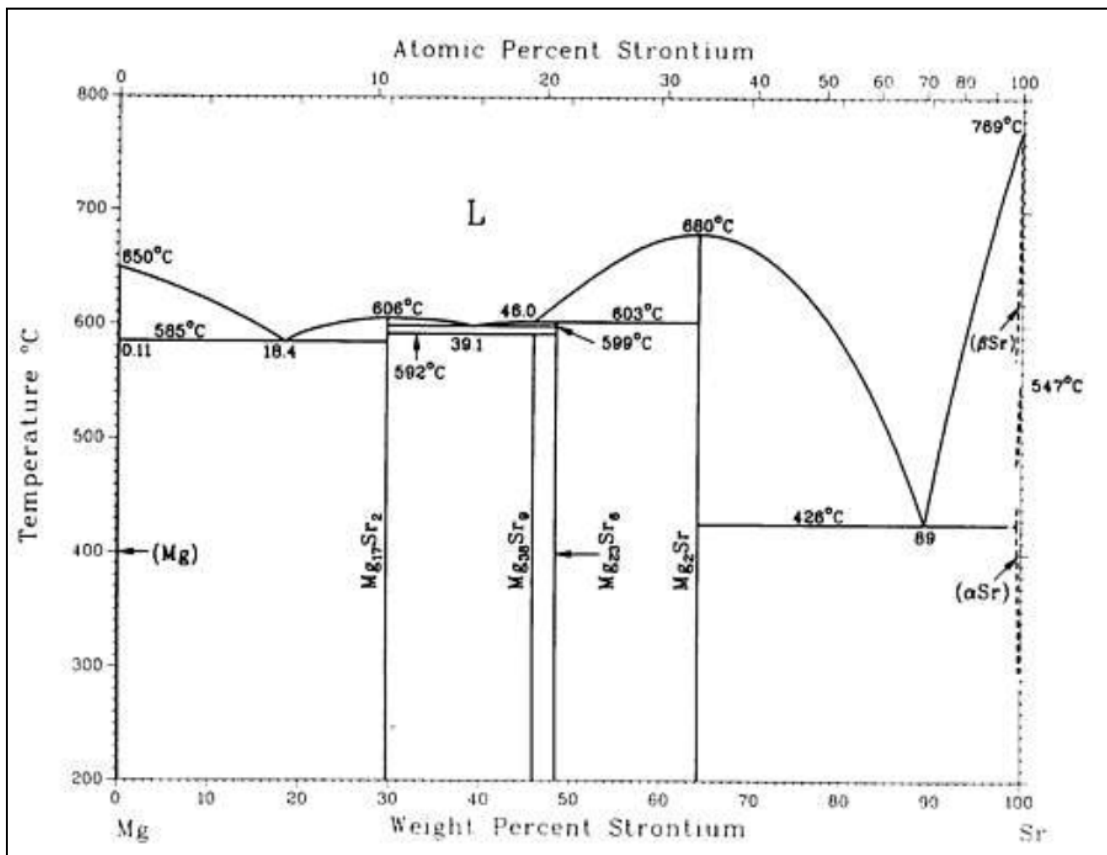


Figure 9. Mg-Sr phase diagram [44]

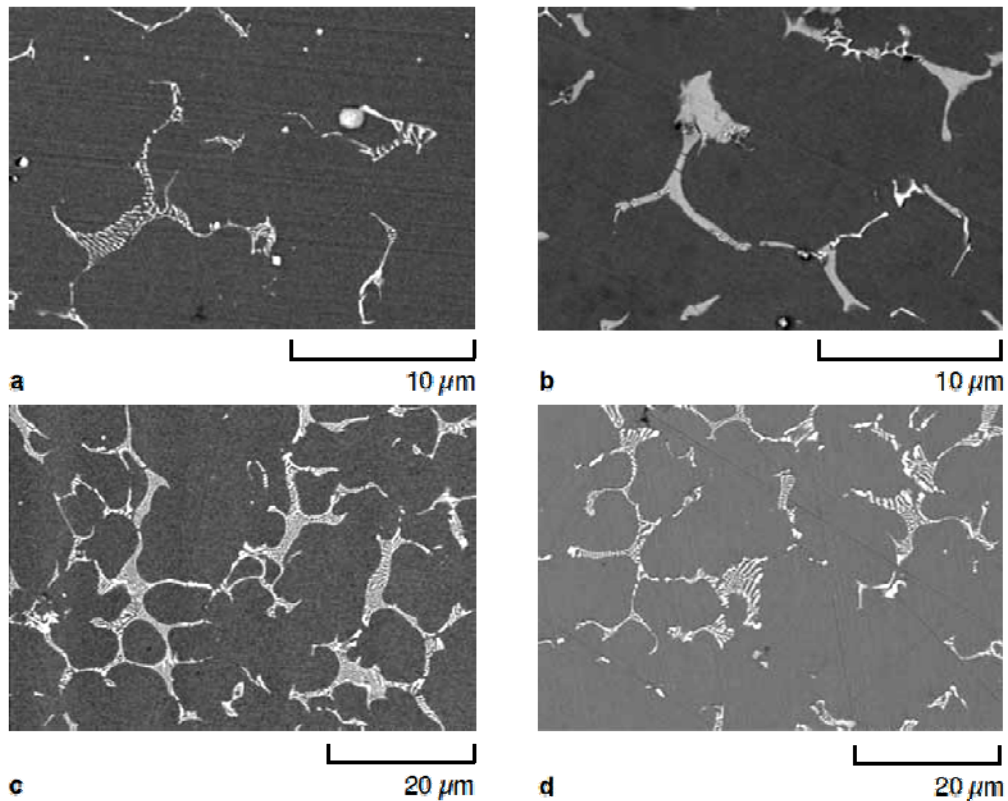


Figure 10. SEM micrographs of various Mg alloys: a) AJ51, b) AJ52, c) AJ62 and d) AJ62L [47]

In the case of the AJC421 alloy, bulky complex Mg-Al-Sr phases formed, as illustrated in Figure 11 [25]. Upon extrusion, the AJC421 alloy underwent dynamic recrystallization and the intermetallics formed bands parallel to the extrusion direction, as can be seen in Figure 11a. Upon extrusion, the creep resistance was 2-3 times worse than that of the as-cast AJC421, indicating that both grain morphology and intermetallic distribution were major contributors to creep resistance of this alloy system [25].

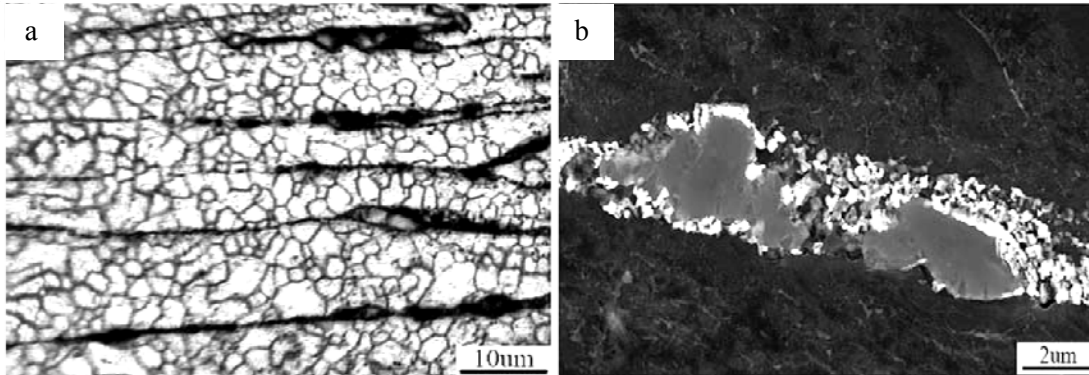


Figure 11. Microstructure of as-extruded AJC421 alloy: a) Bulk grain structure and b) Mg-Al-Sr intermetallic phase [25]

It was also reported that creep in Al-Sr magnesium alloys tends to occur via grain boundary sliding, despite the presence of stable intermetallics [25, 48]. However, existing literature on the exact mechanisms responsible for creep resistance of Al-Sr magnesium alloys is scarce [39].

2.3 Creep Performance of Aluminum Free Magnesium-Rare Earth Alloys

Magnesium alloys without aluminum are generally difficult to cast, but often exhibit excellent mechanical properties. As a result, these alloys are typically used in military and aerospace applications, where cost is not necessarily the determining factor of product viability.

Zinc (Zn) is a common alloying element for Mg alloys. The Mg-Zn phase diagram is presented in Figure 12. Adding Zn to magnesium increases the room temperature strength, eutectic temperature and alloy ductility [4]. The increase in eutectic temperature allows for these alloys to be used at higher service temperatures than in zinc-free magnesium alloys. Zn also promotes continuous dispersion of intermetallics along the grain boundaries, thereby reducing grain boundary sliding. However, Zn addition also increases the susceptibility to microporosity and alloy embrittlement [2].

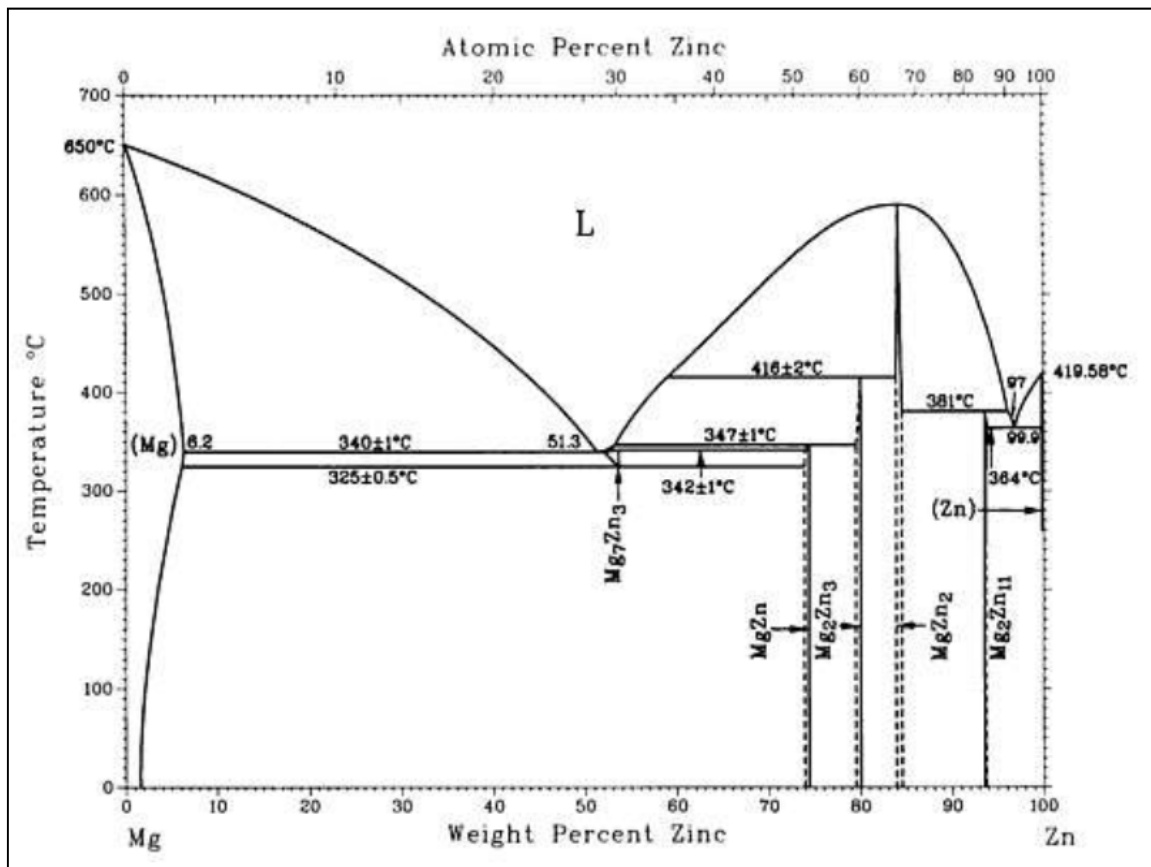


Figure 12. Mg-Zn phase diagram [49]

The addition of REs to Mg-Zn alloys has been shown to further increase alloy creep resistance due to precipitation hardening [4, 25, 37]. Mg_xRE_y and Mg_xZn_y intermetallic compounds readily form in EZ magnesium alloys due to the low solid solubility of REs in Mg [2]. These intermetallic compounds of the form RE_xZn_y were seen to remain stable at temperatures as high as 420°C [27, 50].

With the increasing concentration of rare earths, complex $Mg_xZn_yRE_z$ intermetallic compounds form (e.g., in the EZ33 alloy). As seen in Figure 13, these intermetallics form on the grain boundaries and have serrated edges. This morphology is believed to be very effective at pinning grains during creep [51]. EZ alloys were also observed to contain nanoprecipitates dispersed throughout the matrix, as shown in Figure 14. It is believed that these precipitates would contribute to dispersion strengthening of the alloy, particularly at elevated temperatures [52].

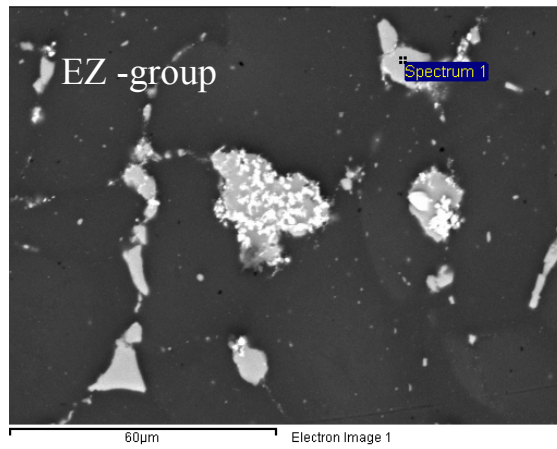


Figure 13. SEM micrograph of EZ33 intermetallic morphology [51]

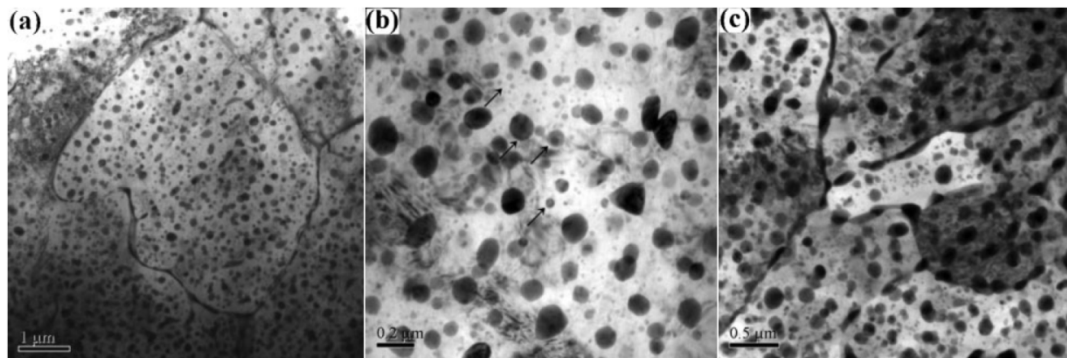


Figure 14. Micrographs depicting: a) Nanoparticle dispersion in EZ alloy, b) Dispersed nanoparticles and c) Precipitates along grain boundaries [52]

3.0 Principles of Neutron Diffraction

Neutron diffraction uses the wave properties of neutrons to obtain crystallographic data about a material. Elastic components of residual stresses, thermal strains and mechanical strains in the material can be measured using neutron diffraction techniques [10, 53].

Due to the ability to select the neutron beam sampling volume, the neutron diffraction method can provide strain data on the bulk deformation of the material. Thus, the contributions of the matrix and the intermetallics located on the grain boundaries are considered together.

A beam of neutrons can be produced and extracted from a nuclear reactor or a spallation source [54]. At the NRU (National Research Universal) reactor at NRC-CNRC, neutrons are created through fission of ^{235}U atoms in a heavy water moderator. The neutrons produced in the NRU reactor are produced at various wavelengths and are known as “white” neutrons [54].

A beam of “white” neutrons is usually directed from the nuclear reactor into a monochromator, which is used to acquire neutrons of a desired wavelength. The resulting monochromatic beam then becomes the incident beam for the sample, as shown in Figure 15. The neutrons are diffracted by crystallographic planes in the sample. The angle of the diffracted neutrons is subsequently measured using an analyzer. Once the diffraction angle, θ , is experimentally measured, Bragg’s Law (Equation 1) is used to calculate the instantaneous lattice spacing, d . In this equation, the wavelength of the neutron beam, λ , and the diffraction order, n , are also known. An incremental change of the lattice spacing is proportional to the applied stress (tensile or compressive). Thus, using the lattice spacing pre- and post-creep, the d_0 and d values can be measured, and the peak-shift method (Equation 2) can be used to calculate the lattice creep strain [1, 12, 10,53].

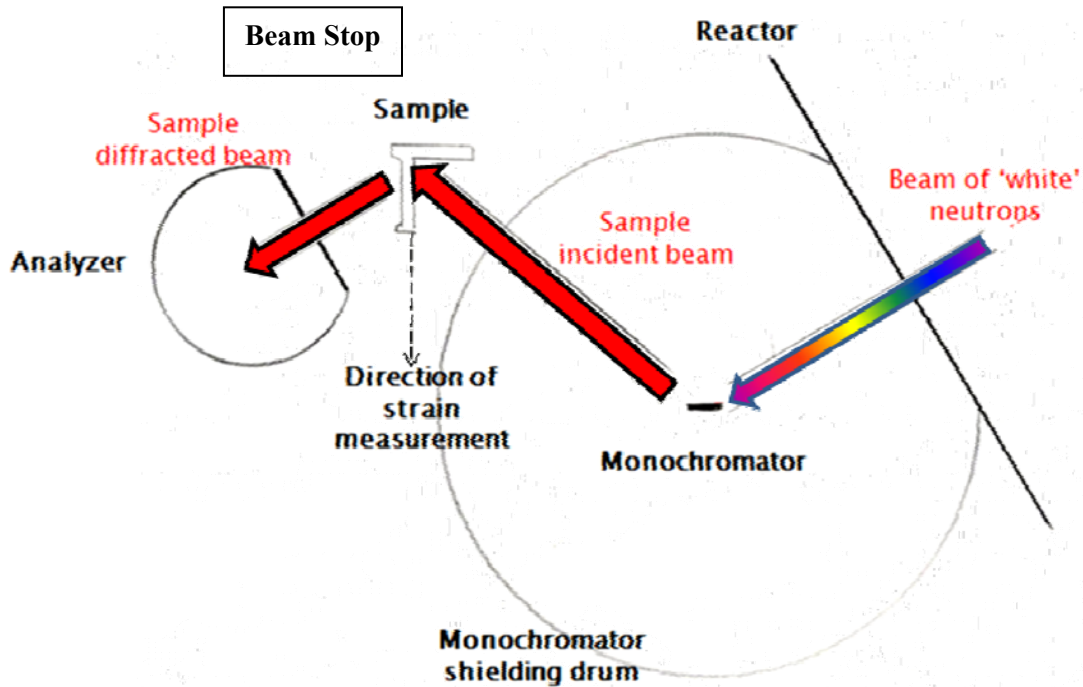


Figure 15. Neutron diffraction schematic

$$n\lambda = 2d \sin(\theta) \quad (1)$$

$$\varepsilon = \frac{(d_0 - d)}{d_0} \quad (2)$$

Neutron diffraction is a non-destructive testing technique and therefore repeated experiments are possible on the same specimen. The material texture, residual stress, surface properties, in-situ properties and magnetism can all be measured under different neutron diffraction testing conditions [12]. Neutrons penetrate deeply into any material and are therefore able to penetrate furnaces and other test apparatuses which maintain test samples in controlled environments [12, 54].

Although there are many advantages for using neutron diffraction in materials science research, the shortfall of this technique is the need to calculate lattice strain from neutron diffraction testing. The equations used are based on assumptions, which may be a source of experimental error [12]. For example, determination of the stress-free spacing, d_0 , can be done by several methods, each carrying distinct degree of error. Also, the intensity of neutrons scattered from a material is largely dependent on presence of crystallographic texture. Highly textured materials exhibit weaker diffraction signals for certain crystallographic planes, which results in long experimental times [53].

4.0 Experimental Procedure

A detailed description of the experimental techniques and procedures is provided in this chapter. This includes the material selection process, metallography techniques and the procedures used in neutron diffraction testing.

4.1 Material Selection

The extruded alloy samples used in this research were produced by Timminco Corporation, Canada. The alloys were created using a continuous direct chill casting process, followed by hot extrusion. The alloys were cast and formed without cracking or other processing defects. Detailed processing conditions are proprietary information of Timminco Corporation and therefore will not be listed.

The material selection for this research was based on the results of preliminary creep experiments [51]. The alloys studied previously included AE42, AE33, AX30, AZX310, AJ32, ZE10 and EZ33. The creep strain of these alloys after 200 hours under a 50MPa load can be seen in Figure 16 and Figure 17. Figure 16 shows a comparison of tensile creep at 150°C versus 175°C for each alloy listed above, whereas Figure 17 is a comparison of each alloy in tensile versus compressive creep at 150°C.

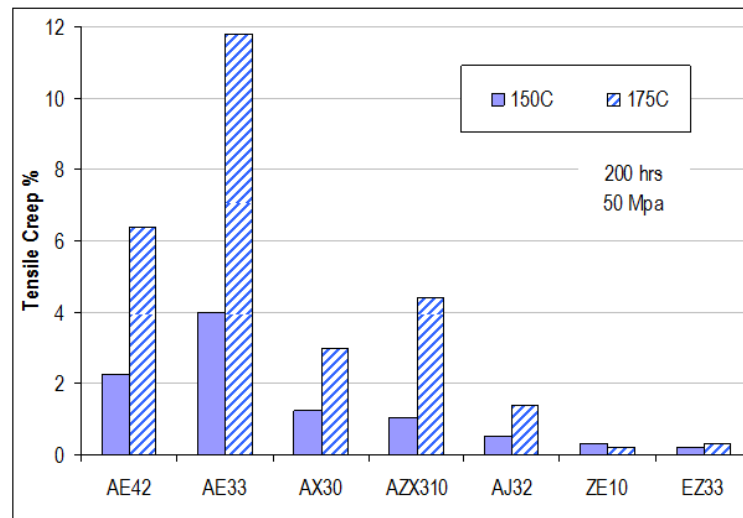


Figure 16. Tensile-creep strain for the AE42, AE33, AX30, AZX310, AJ32, ZE10 and EZ33 alloys at 150°C and 175°C [51]

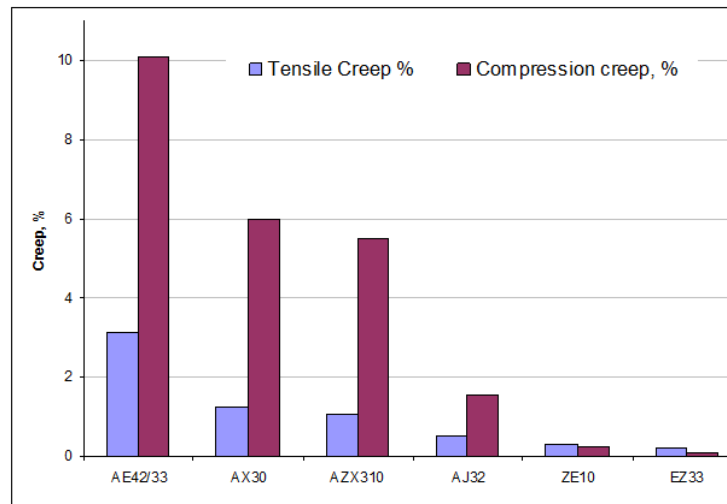


Figure 17. Tension-compression asymmetry in resistance to creep for the AE42, AE33, AX30, AZX310, AJ32, ZE10 and EZ33 alloys at 150°C [51]

In both figures, the lowest creep strains were observed for the aluminum (Al) free alloys, ZE10 and EZ33. With respect to the Al containing alloys, during tensile creep at both 150°C and 175°C (as seen in Figure 16), AJ32 had the lowest creep strain, followed by AX30. The present research therefore focused on investigating the AJ32, AX30, ZE10 and EZ33 alloys due to their superior creep resistance over the AE33 and AZX310 alloys. The AE42 alloy is an industrial benchmark alloy for creep resistance and was therefore included in this research as well.

Due to time and monetary constraints, complete testing was not feasible for all five alloys (AE42, AJ32, AX30, EZ33 and ZE10). Therefore, comprehensive testing was performed for AE42, AJ32 and ZE10 while partial testing was completed for AX30 and EZ33. A summary of the experiments performed on each alloy is given in Table 1. AE42 was chosen for comprehensive testing as it is an industrial benchmark. AJ32 was chosen over AX30 due to its superior creep resistance. Comprehensive testing was completed for ZE10 alloy and not EZ33 alloy due to the low percentage of REs in the ZE10 alloy. The low percentage of REs in ZE10 will decrease alloy cost and thus make it more attractive for industrial applications.

Table 1. Summary of testing performed for the AE42, AJ32, ZE10, EZ33 and AX30 alloys

Alloy	Condition	AE42	AJ32	ZE10	EZ33	AX30
Neutron Diffraction	As Extruded	✓	✓	✓	✗	✗
Scanning Electron Microscopy	As Extruded	✓	✓	✓	✗	✗
	Post-compressive creep (175°C)	✓	✓	✓	✗	✗
Optical Microscope Microscopy	As Extruded	✓	✓	✓	✓	✓
	Post-compressive creep (175°C)	✓	✓	✓	✓	✓

The five alloys chosen for analysis in this research were AE42, AJ32, AX30, EZ33 and ZE10; their nominal compositions are given in Table 2.

Table 2. Nominal alloy compositions for AE42, AJ32, AX30, EZ33 and ZE10 [51]

	AE42 (wt%)	AJ32 (wt%)	AX30 (wt%)	EZ33 (wt%)	ZE10 (wt%)
Al	3.5-4.5	3-3.5	3-3.5	≤0.05	≤0.05
Zn	≤0.2	≤0.2	≤0.2	2.5-3.1	0.8-1.2
Mn	0.2-0.5	0.2-0.5	0.2-0.5	0.2-0.5	0.2-0.5
Fe	≤0.01	≤0.01	≤0.01	≤0.01	≤0.01
Ni	≤0.005	≤0.005	≤0.005	≤0.005	≤0.005
Cu	≤0.05	≤0.05	≤0.05	≤0.05	≤0.05
Si	≤0.05	≤0.05	≤0.05	≤0.05	≤0.05
Ca			0.5-0.8		
Sr		1.5-2.5			
Zr				0.45-0.7	0.45-0.7
Ce	0.9			1.4	0.2
La	0.3			0.8	0.1
Nd	0.2			0.7	0.1
Pr	0.5			0.3	0.01
Mg	Balance	Balance	Balance	Balance	Balance

4.2 Neutron Diffraction

Neutron diffraction experiments were carried out at the National Research Council-Canadian Neutron Beam Center (NRC-CNBC) in Chalk River, ON. The experiments were performed using the L3 spectrometer. The details of the experiment are given below along with experimental conditions, set-up, procedures and the methods of raw data analysis.

4.2.1 Neutron Diffraction Experimental Conditions

Neutron diffraction experiments in this research consisted of compressive creep experiments under a 50MPa load at 175°C. Compressive creep testing was chosen since many automotive components tend to be loaded in compression (e.g., bolt loading areas of gear box housings in engines) [9]. A test temperature of 175°C was chosen because this temperature is of importance for gas and diesel combustion engine environments. These conditions of temperature and load would expose the material to the most extreme conditions expected to be present in vehicles.

The force required for a 50 MPa load was calculated from Equation 3, where F was the applied force, σ was the applied stress and D was the sample diameter. The geometry of test specimens used in this research is provided in Figure 18. Based on the cross-section of the sample, the applied force corresponding to a 50 MPa load was calculated to be 1411 N.

$$F = \sigma \pi \left(\frac{D}{2}\right)^2 \quad (3)$$

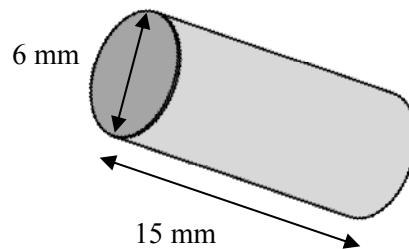


Figure 18. Dimensions of samples used for compressive strain measurement using neutron diffraction

4.2.2 L3 Spectrometer Setup

The L3 spectrometer setup is shown in Figure 19. The setup consisted of:

1. Nuclear reactor
2. Monochromator
3. Incident neutron beam
4. Beam stop
5. Sample
6. Diffracted beam
7. Diffracted beam analyzer
8. Stress rig

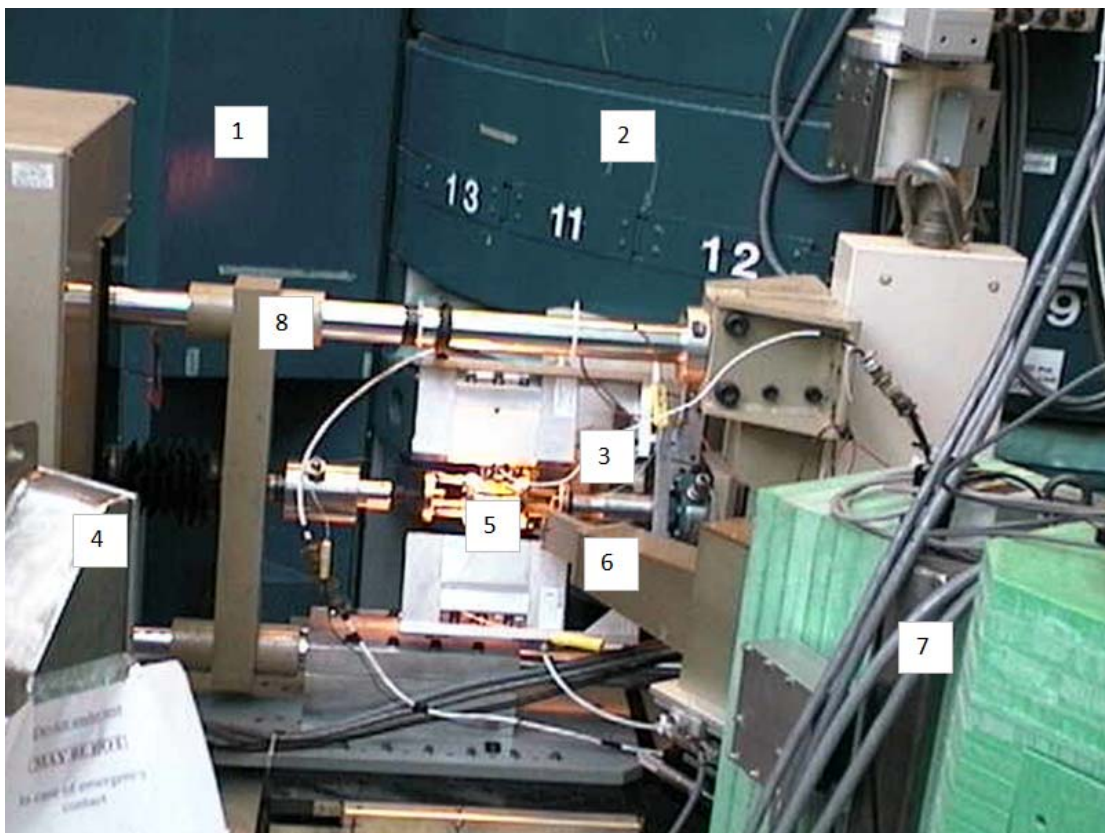


Figure 19. L3 spectrometer setup for neutron diffraction testing

The neutron path at the sample is shown in Figure 20. The majority of neutrons passed through the sample to the beam stop, while a fraction of the neutrons was diffracted by the atomic planes of the sample. The diffracted neutrons formed the diffracted beam and were collected by the diffracted beam analyzer.

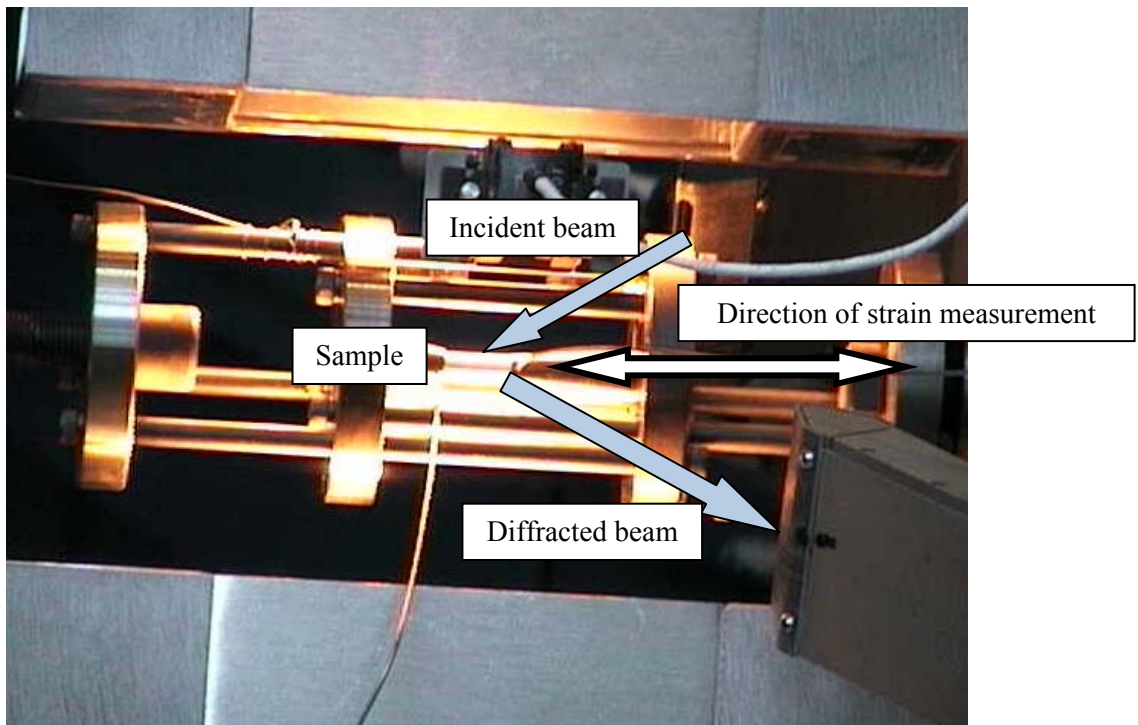


Figure 20. Neutron diffraction incident and diffracted beam paths

An illustration of the apparatus used to compress the sample is provided in Figure 21. The application of a tensile force couple aligned the apparatus, so that the force vector passed along the axis of the sample, and the applied tensile force was converted into a compressive force on the sample.

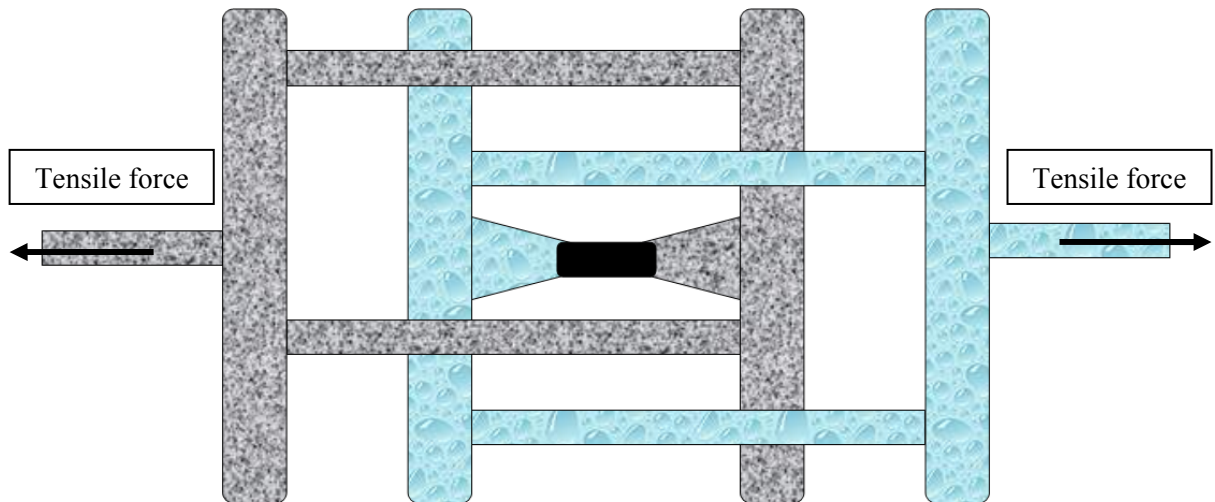


Figure 21. Neutron diffraction compression apparatus

The specimen setup and compression apparatus can be seen in Figure 22. The components of this setup were:

1. Infrared heater #1
2. Infrared heater #2
3. Extensometer
4. Sample
- 5 & 6. Tensile loader
- 7 & 8. Vise
9. Incident beam slit
10. Diffracted beam slit
11. Thermocouple #1
12. Thermocouple #2
13. Safety thermocouple

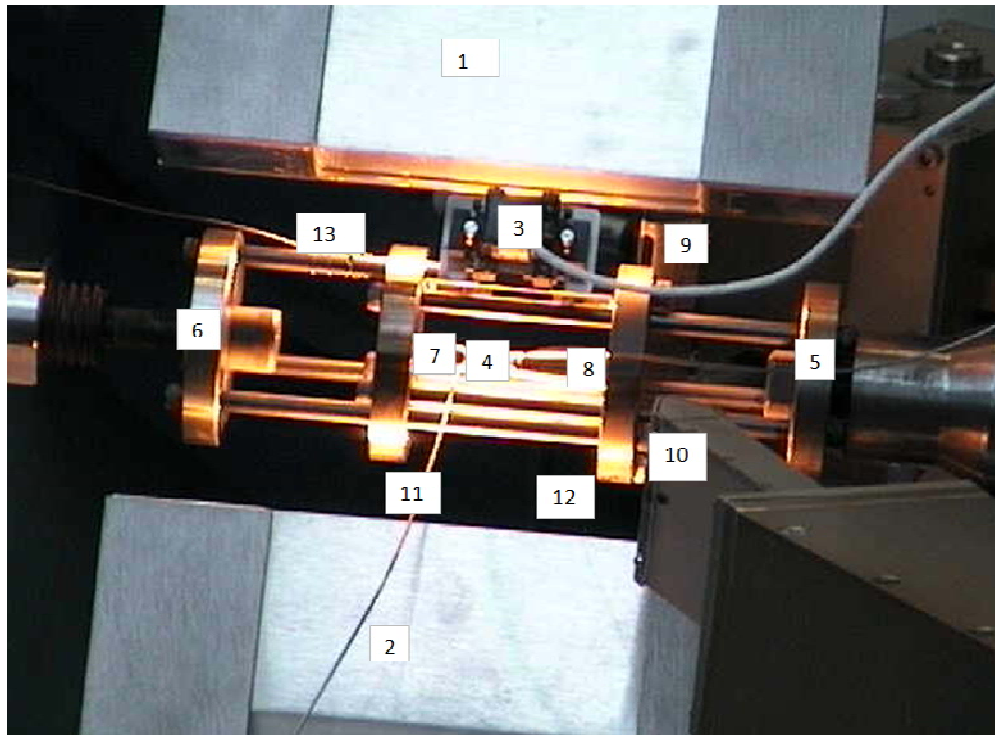


Figure 22. Specimen setup for neutron diffraction testing

The sample was heated by the two infrared heaters (1&2). The sample temperature was monitored by two thermocouples (11&12) while a third thermocouple was used to measure apparatus temperature for safety purposes (13). The reading from these three thermocouples were used to ensure a constant temperature across the apparatus and the sample.

An extensometer (3) was used to measure total deformation of the sample. The extensometer was attached to the compression apparatus rather than the sample itself. This meant that the deformation measured included that of the sample and of the apparatus. The experimental error that arose from this set-up was deemed to be negligible, since the elastic modulus of the steel apparatus was significantly greater than that of the magnesium sample (200 GPa vs. 45 GPa) and the deformation of the apparatus would be negligible in comparison to that of the magnesium sample.

The sample (4 in Figure 22) was placed between the vise components of the compression apparatus (7 & 8) and the tensile loaders (5 & 6) were used to apply a compressive force to the sample. The neutron incident beam came from the incident slit (9) and hit the sample (4) before being diffracted into the diffracted beam slit (10) and then the analyzer.

4.2.3 Neutron Diffraction Experimental Procedure

Compressive-creep behavior of the Mg alloys AE42, AJ32 and ZE10 was analyzed using neutron diffraction. The material samples were hot extruded and machined into rods approximately 15mm long with a diameter of 6 mm. The actual dimensions of the machined samples are provided in Table 3.

Table 3. Neutron diffraction sample dimensions before testing

Alloy	Length (mm)	Diameter (mm)
AE42	15.0	6.0
AJ32	14.9	6.0
ZE10	15.0	6.0

Prior to use of the compression apparatus, the extensometer was calibrated by measuring the voltage change over a 2 mm change in distance. The voltage output versus change in distance can be seen in Figure 23 along with the corresponding line of best fit.

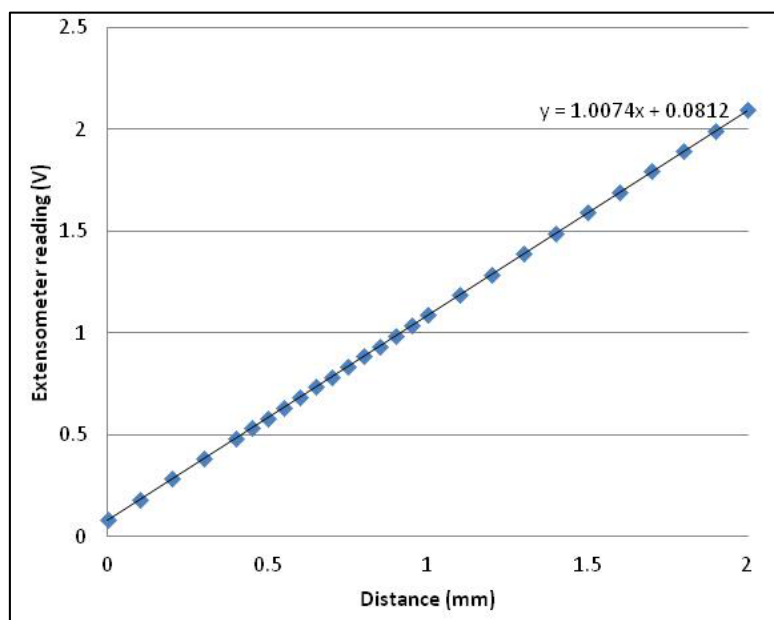


Figure 23. Extensometer calibration: voltage vs. displacement

A germanium (Ge) monochromator single crystal was used to manipulate the wavelength of the sample incident neutron beam. The (331) crystal plane of the Ge single crystal was chosen to yield a neutron beam wavelength of 1.792 Å. This wavelength was close to the lattice spacing of the magnesium alloys, yet remained large enough to result in a sufficient neutron flux (thus minimizing the time required for data acquisition). The magnesium alloy sample was then centered in the neutron beam by following sample set-up procedures prepared by NRC-CNBC scientists. These procedures are publically available to all neutron beam line users.

Once the neutron beam wavelength was selected, the theoretical diffraction angles were calculated for crystallographic planes of interest. These diffraction angles were necessary in order to set an initial angular position (φ) for the diffracted beam analyzer. Theoretical diffraction angles (θ) for pure Mg were calculated using Bragg's Law, as listed in (Table 4), using the theoretical crystal lattice spacing obtained from the literature.

Table 4. Theoretical diffraction angles for Mg

Plane	Diffraction angle (degrees)
$10\bar{1}0$	37.62
0002	40.24
$10\bar{1}1$	42.87
$10\bar{1}2$	56.26
$2\bar{1}\bar{1}0$	67.90

The actual diffraction angles slightly differed from the theoretical angles, since the lattice structure of the tested alloys was not identical to that of pure Mg. Introducing solute elements affects the position of atoms in a lattice, while presence of residual stresses can also alter the spacing of crystallographic planes. For example, the analyzer was first set to $\varphi=37.62^\circ$ to measure the diffraction flux from the $\{10\bar{1}0\}$ planes, as seen in Figure 24. The peak neutron flux was then used to determine the exact diffraction angle for a particular alloy, as presented in Table 5 for the ZE10 alloy.

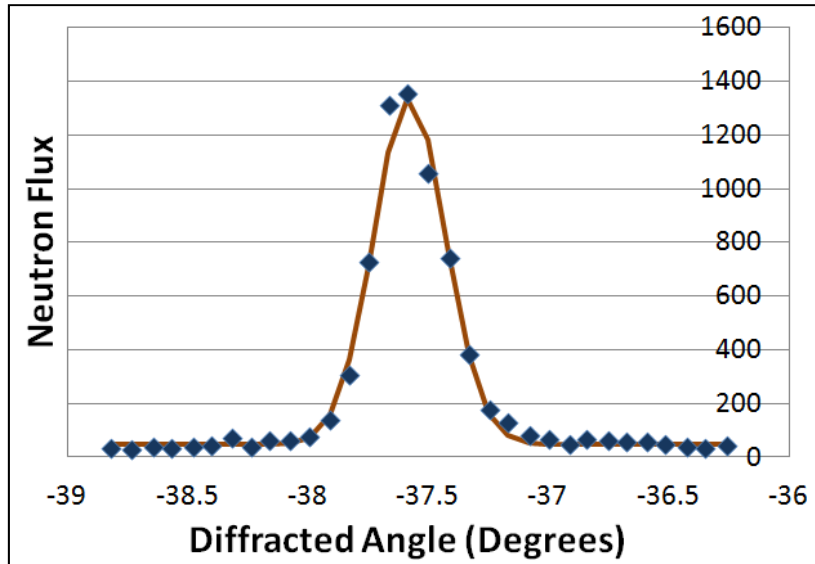


Figure 24. Neutron count vs. diffraction angle

Table 5. Measured diffraction angles for ZE10 during neutron diffraction

Plane	Diffraction angle (degrees)
$10\bar{1}0$	37.54
0002	40.24
$10\bar{1}1$	42.79
$10\bar{1}2$	56.26
$2\bar{1}\bar{1}0$	67.90

The load and temperature conditions imposed on the material during testing are summarized in Figure 25. At each step listed in Figure 25, the diffraction angles were measured for each of the planes listed in Table 5.

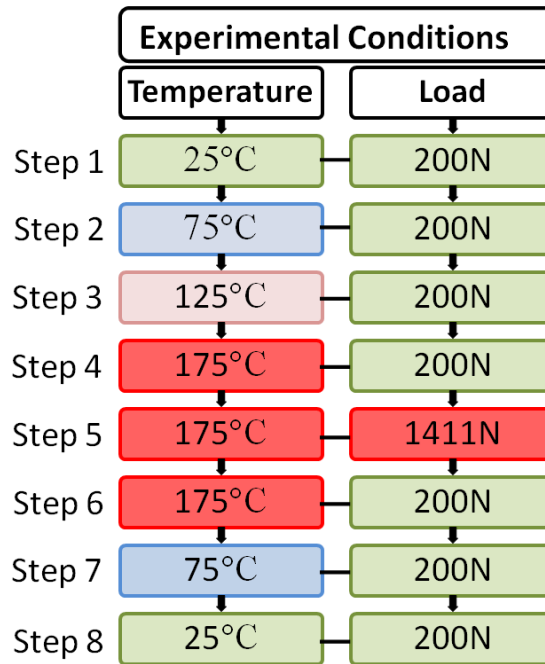


Figure 25. Compressive creep testing experimental conditions performed during neutron diffraction

The first neutron diffraction measurement (step 1) was obtained at room temperature and 200N applied force. This force was required to hold the sample in the vise of the compression apparatus. The temperature was then increased in steps 2-4 by 50°C intervals, while maintaining the 200 N force. The temperature was increased gradually to avoid overheating of the material sample. Upon heating, the material expanded and the lattice spacing increased due to thermal strain. Neutron diffraction measurements were taken for each plane at each temperature interval in steps 2-4 to measure the amount of thermal strain during heating.

Once the thermal strains were measured, step 5 consisted of applying a load of 1411 N to the sample, while maintaining the temperature at 175°C. These conditions were held constant for approximately 24 hours during which elastic strain measurements were recorded. During this time, the lattice spacing was measured at each plane repeatedly to analyze lattice strain during material creep.

Once the 24 hours of creep testing was complete, the load was released (step 6, Figure 25). The temperature was then lowered to room temperature, as can be seen in steps 7 and 8. Finally, the strains at these temperatures were compared to those of the sample measured during steps 1.

Upon completion of steps 1-8, the sample was removed from the apparatus using tongs and the final dimensions were recorded. The samples were then processed through the NRC-CNBC safety surveyor until the material radiation reached acceptable levels for transportation and handling.

4.2.4 Neutron Diffraction Data Analysis

The neutron diffraction data gained from each measurement took the form of neutron flux versus diffraction angle, as seen in Figure 24 and Figure 26. A curve was fitted to this data and the position of the peak was used as the measured angle of diffraction. The diffraction angle was then used to measure lattice spacing using Bragg's Law.

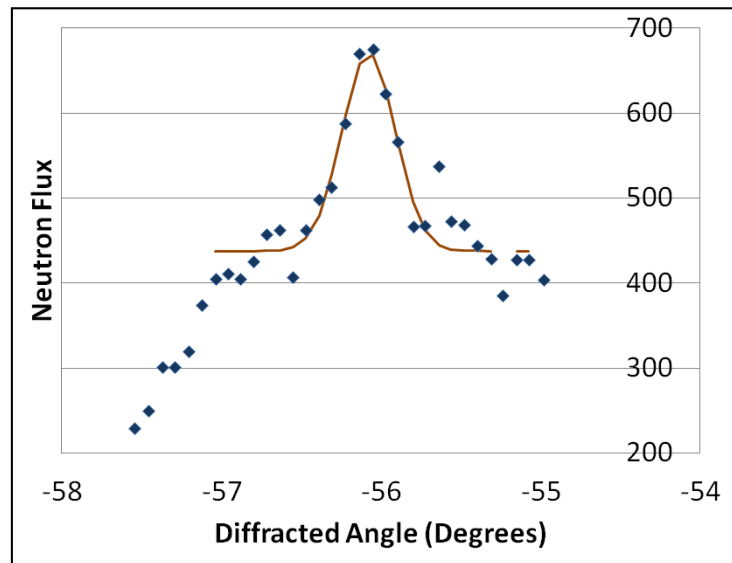


Figure 26. Neutron count vs. diffraction angle (with outlier data points)

Due to the texture of the extruded alloys, the flux measured from each plane did not always form a clean peak (as shown in Figure 26). In cases where outliers were apparent, the outlier points were neglected from the curve fitting and the peak was determined from the remaining points.

Once the diffracted angle was measured, it was then used to calculate the lattice spacing and microstrain using Equations 1 and 2. The value of d_0 was taken as the lattice spacing at step 1 of the neutron diffraction procedure, where the sample had no applied stress at room temperature.

In conjunction with the diffraction lattice strain measurements, the extensometer, load and thermocouple data were collected and recorded in one minute intervals during the experiment. The values measured by the safety thermocouple and applied load were constantly monitored. If the applied load and temperature varied by more than 20 N and/or 5°C, respectively, the loads were altered to maintain test conditions as laid out in Figure 27. Variations below 20N and 5°C were assumed not to affect results significantly. An example of the applied load and temperature over time can be seen in Figure 27 along with labels indicating the corresponding steps in the procedure from Figure 25.

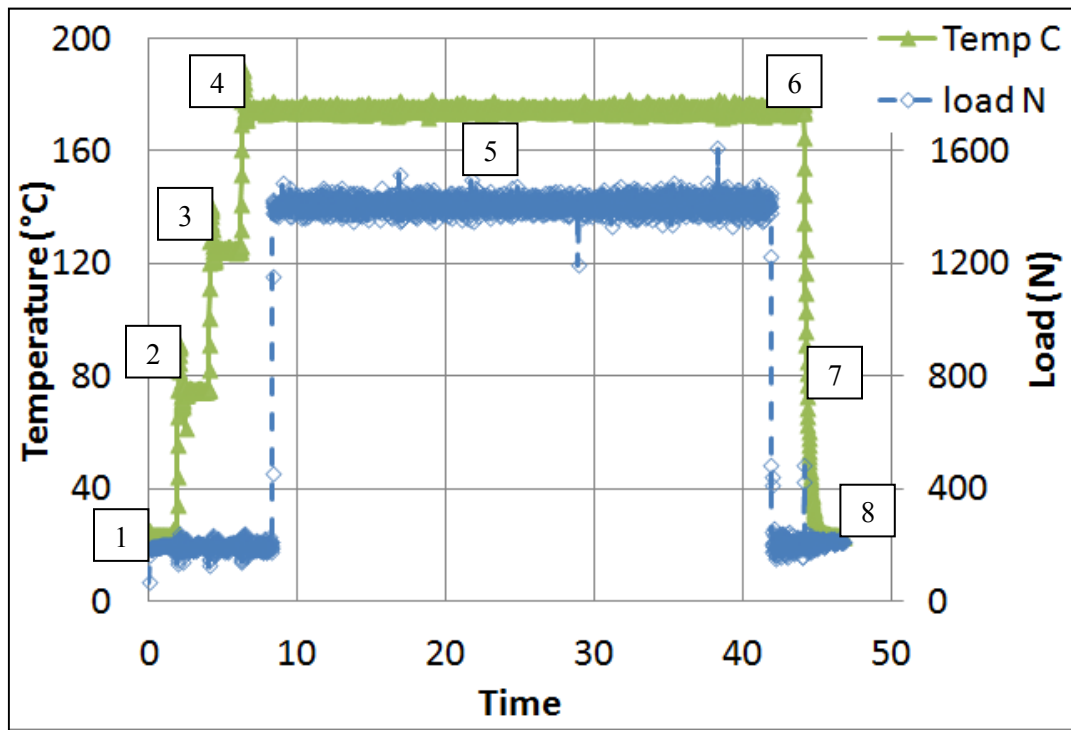


Figure 27. Profile of applied load and temperature during neutron diffraction testing. Corresponding experiment steps are presented in Figure 25

4.3 Microscopy

Metallographic samples were prepared using standard techniques for Mg alloys. A Zeiss AxioObserver A1m microscope with differential interference contrast (DIC) capability was used for metallographic analysis of the as-extruded and post-creep specimens. Scanning electron microscopy was conducted using Tescan Mira3 XMU Scanning Electron Microscope (SEM) with X-ray Energy Dispersive Spectrometry (XEDS) capability. Metallographic analysis was performed using Buehler OmniMet software. This software allowed for the accurate and repeatable measurement of microstructure characteristics.

4.3.1 Sample Preparation

As-extruded rods of the studied alloys were sliced into torus-like specimens, as seen in Figure 28. The outer diameter of the torus was 25 mm, inner diameter was 7 mm and thickness 9 mm. The torus was then sectioned to reveal the cross section (surface parallel with the extrusion direction) and the radial section (surface perpendicular to the extrusion direction).

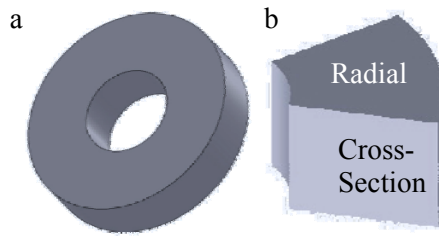


Figure 28. As-extruded alloy samples: a) Torus and b) Sample surfaces examined

In industry, AE42 alloys are typically heat treated after extrusion to decrease the amount of β -phase in the matrix. This heat treatment is known to increase the creep resistance of the alloy. However, in this research no heat treatment was performed in order to allow comparison of alloys in their as-extruded conditions. The absence of heat treatment of the AE42 alloy possibly caused a discrepancy with respect to alloy properties normally found in the literature. This was, however, less relevant to the industrial partner of this project, since finding an alloy which does not require a heat treatment would be a significant technological advance for commercialization of magnesium alloys.

Metallography was performed on post-creep samples after the neutron diffraction experiments were completed. As mentioned in section 4.2.3 Neutron Diffraction Experimental Procedure, material samples were machined into 6 mm diameter rods 15 mm long. After conducting creep tests with these samples, the rods were sectioned to reveal the radial and cross section directions, as depicted in Figure 29.

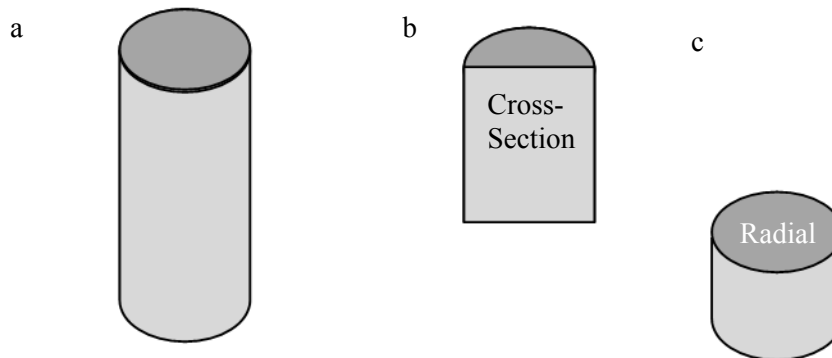


Figure 29. Post-creep alloy samples: a) Machined sample, b) Cross-section and c) Radial section

Each material sample in the as-extruded and post-creep conditions and in the radial and cross-section directions, was mounted in a cold mount acrylic material, as seen in Figure 30. Mounting the material specimens allowed for easy handling during polishing and microstructure analysis.



Figure 30. Representative example of the mounted and polished sample

Once the material samples were mounted, mechanical polishing was performed using various grades of emery paper (0, 2/0, 3/0 and 4/0) in stages of decreasing roughness. The samples were rotated 90° between each polishing stage to ensure the removal of all mechanical deformation from the previous stage. This was followed by polishing with diamond paste in sizes of 9 μm , 3 μm and 1 μm on a medium nap cloth. The final polishing stage involved the use of an 0.05 μm Al₂O₃ powder suspension on a fine nap cloth, polished by hand. The samples were rinsed between each polishing stage with alcohol.

4.3.2 Scanning Electron Microscopy

The alloys AE42, AJ32 and ZE10 in their as-extruded and post-creep conditions were analyzed using a Tescan MIRA3 XMU scanning electron microscope (SEM) and Oxford EDS X-max XEDS detector. Alloy samples were sputter coated with 5nm of platinum/palladium to make their surface conductive.

The coated sample was then placed in the SEM holder along with a copper stub. The copper stub was used for X-ray XEDS calibration. The copper stub was raised to a similar height of that of the sample. This setup can be seen in Figure 31.

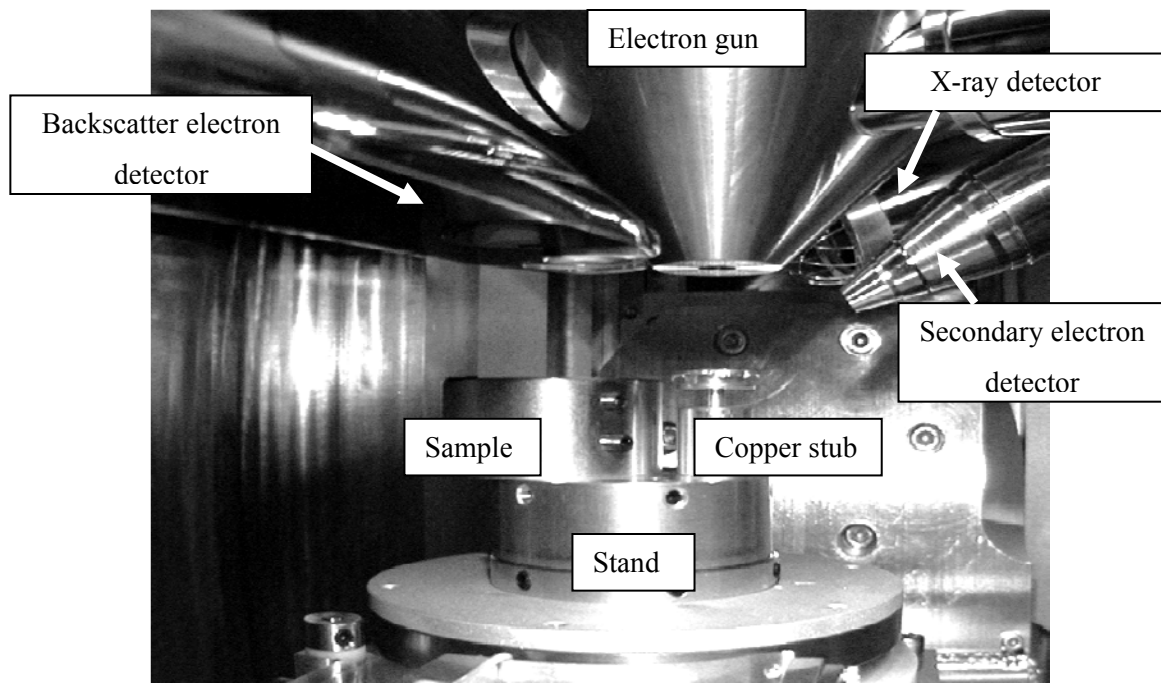


Figure 31. The SEM chamber of the Tescan MIRA3 XMU SEM

Once the sample was placed in the SEM chamber, the door was closed and the chamber was evacuated. An electron accelerating voltage of 20kV was used for analysis. The working distance was set to 20mm from the electron gun. At this position, the XEDS system had the highest efficiency. The electron gun was then optimized and centered to ensure good quality images.

Following gun centering, an XEDS optimization was performed, by carrying out chemical analysis on the copper stub. Optimization and gun centering were re-done every 2 hours to maintain a high efficiency and short test duration.

After collecting secondary and backscatter images, XEDS analysis was performed in the form of point scans, area scans, linescans and smartmaps. Examples of these can be seen in Figure 32. Each point and area scan gave the composition of the area in atomic percent.

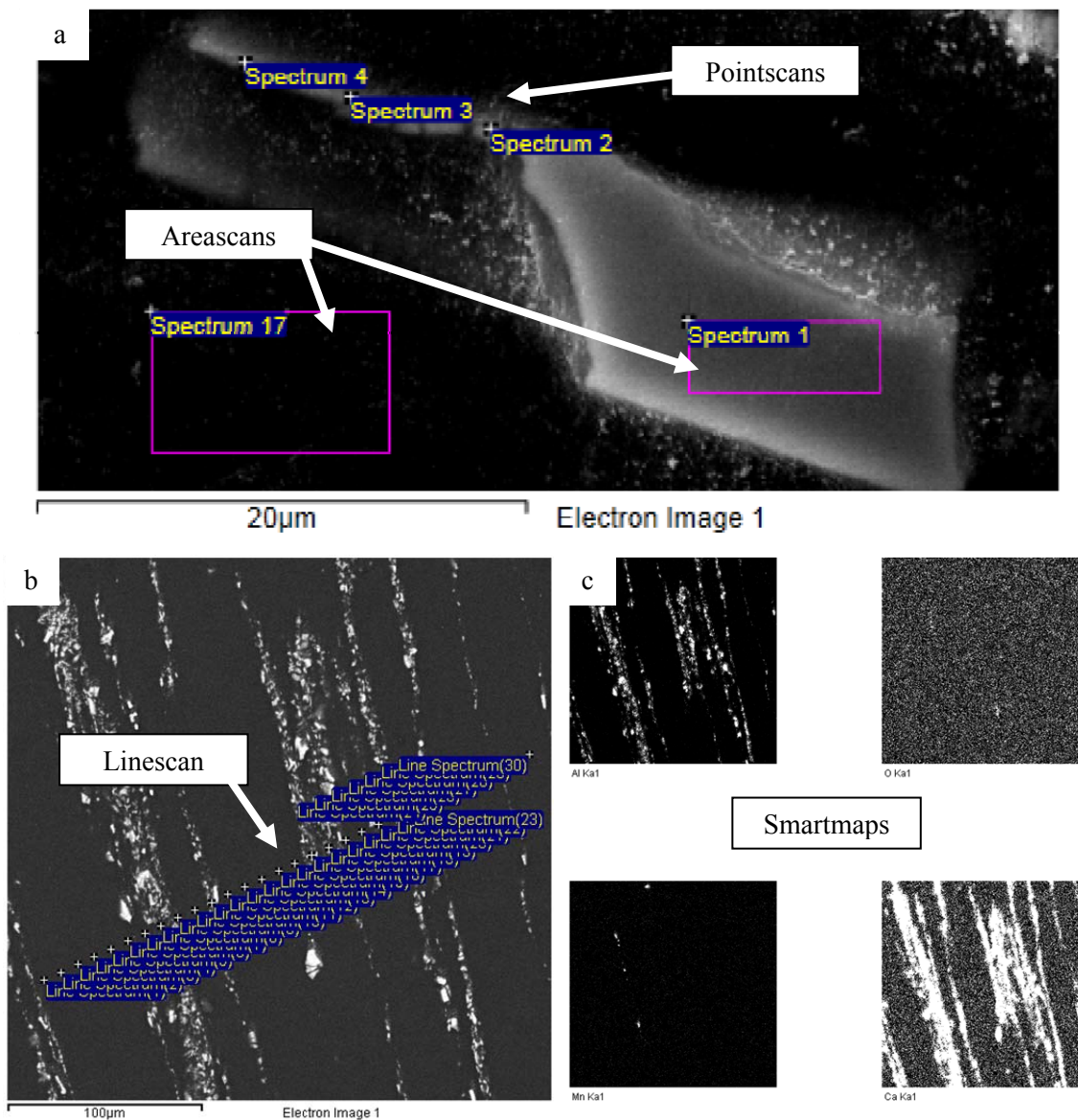


Figure 32. Examples of XEDS analysis: a) Point and area scans, b) Linescans and c) Smartmaps

Smartmaps were used in conjunction with backscatter electron micrographs to distinguish between different intermetallics and solute segregation. Point and area scans were used to find the elemental composition of each intermetallic compound. Linescans were used to analyze compositional changes across bands of solute segregation, between two intermetallics, across grain boundaries and at transitions from the intermetallics to the matrix.

The atomic compositions reported by the XEDS system sometimes contained incorrectly identified elements. These elements, resulting from XEDS noise and Bremsstrahlung radiation, were manually eliminated from the results. Subsequently, the intermetallic compositions were determined by finding the lowest common denominator in the percentages. The accuracy of intermetallic composition was ± 0.1 atomic %.

4.3.3 Optical Microscopy

All material samples were etched using gentle agitation in Glycol (Table 6). Glycol was used to reveal the general microstructure of each alloy, including grain boundaries, subgrain boundaries, intermetallic compounds and mechanical twinning [2]. The time required to etch each sample was determined through trial and error. The etching time changed for each alloy, between the as-extruded and post-creep conditions and was dependant on which microstructural component was being analyzed. Table 7 shows the etching time for each alloy, material condition and microstructural component. After etching was accomplished, the samples were rinsed using alcohol and wiped dry using a cotton swab.

Table 6. Glycol etchant composition

Substance	Amount (mL)
HNO ₃	2
Distilled water	24
Ethylene glycol	75

Table 7. Summary of the time required for alloy etching using glycol

Alloy	Condition	Etching time needed for:		
		Subgrains (min)	Twinning (min)	β -phase (min)
AE42	As-extruded	2.0	2.0	1.5
	Post-creep	2.0	2.0	1.5
AJ32	As-extruded	0.5	0.5	
	Post-creep	0.5	0.5	0.5
AX30	As-extruded	1.5	1.5	
	Post-creep	1.0	1.0	1.0
EZ33	As-extruded	4.0		
	Post-creep	3.0	3.0	
ZE10	As-extruded	3.0		
	Post-creep	3.0		

Optical microscopy was performed using both bright field and the DIC modules of the microscope. The bright field module was especially effective for viewing β -phase at low magnifications. Bright field micrographs were used to view different intermetallic compounds and to calculate their relative area percent. The DIC module was more effective at higher magnifications, where it was able to distinguish between different intermetallics, subgrain boundaries, twinning

boundaries and intermetallic structures. Examples of bright field versus DIC micrographs can be seen in Figure 33.

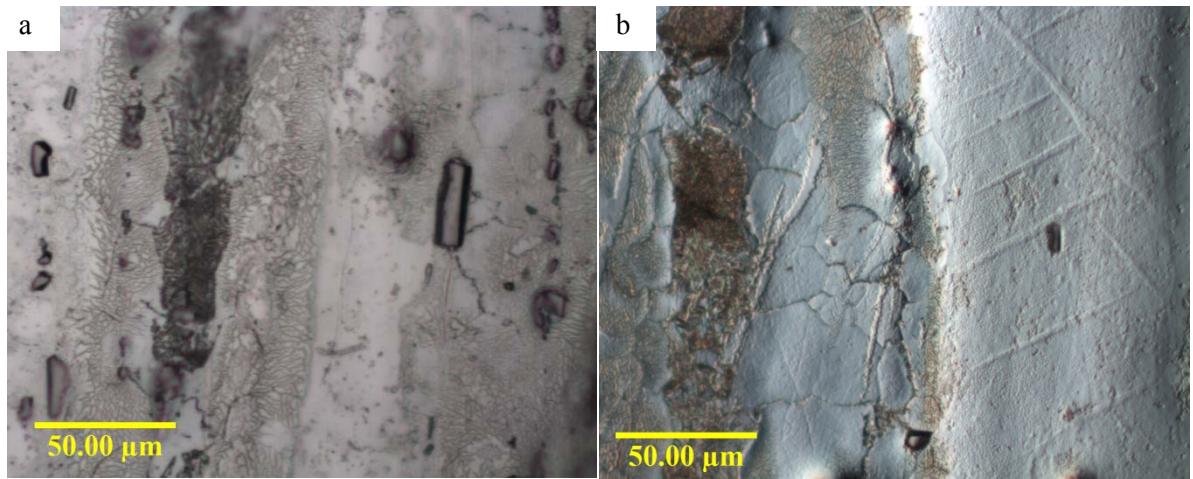


Figure 33. AE42 alloy micrographs in the: a) Bright field and b) DIC modules

Since all alloys were extruded, elongated grains were observed in the cross-section samples. These samples were then characterized by measuring the grain widths, subgrain sizes and twinning directions. Grain widths were measured using an imaging routine. The subgrain sizes and twinning directions were measured manually to ensure accuracy, as the imaging routine was unable to distinguish subgrains and twins from the surrounding microstructure.

The routine used to measure the alloy grain widths is outlined in Figure 96. An example of the micrograph and delineated image are shown in Figure 34.

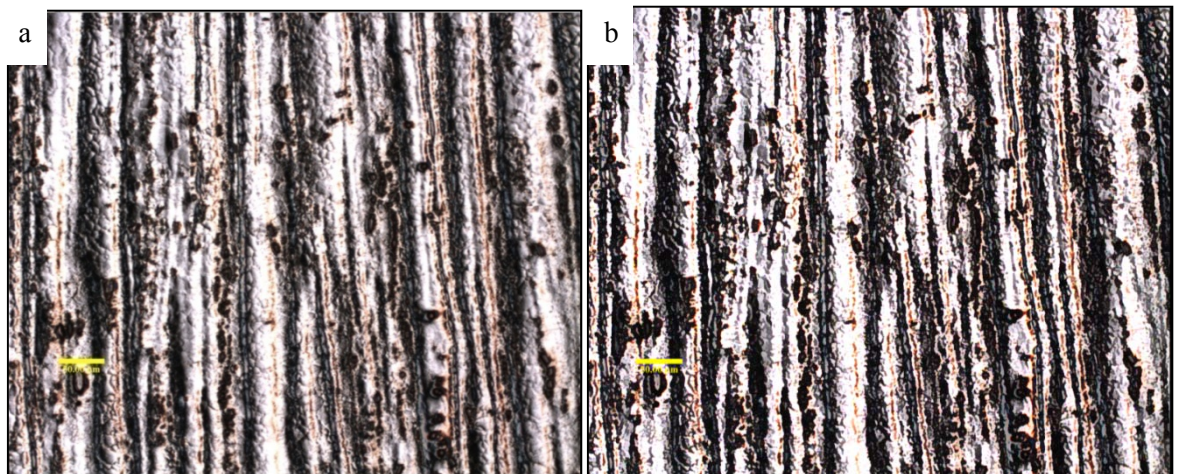


Figure 34. Cross-section of the AE42 alloy (100x magnification): a) Captured and b) Delineated

Thereafter the grain boundaries were colored blue and the matrix purple, as shown in Figure 35.

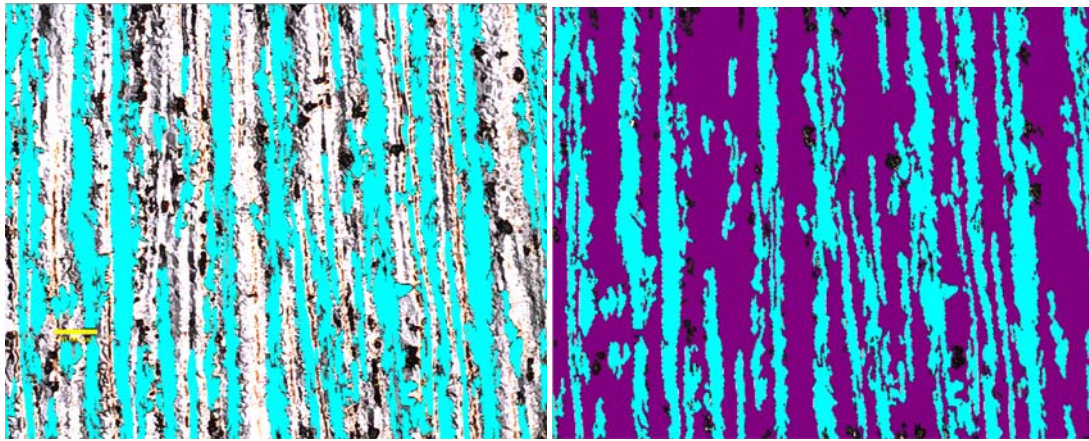


Figure 35. Grain boundaries and matrix in the AE42 alloy cross-section

Finally, the software routine overlaid 50 horizontal lines across the image, as depicted in Figure 36. Each line was used to measure the grain widths across the image by measuring the length at which the line overlapped a purple section. This enabled the routine to gather an overall grain width averaged over the entire field of view. The measurement results included mean, minimum and maximum grain width and standard deviation of the measurements.

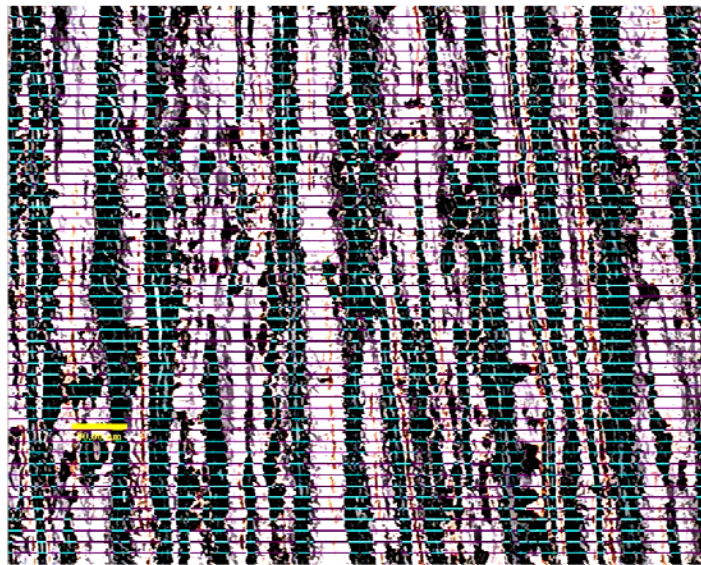
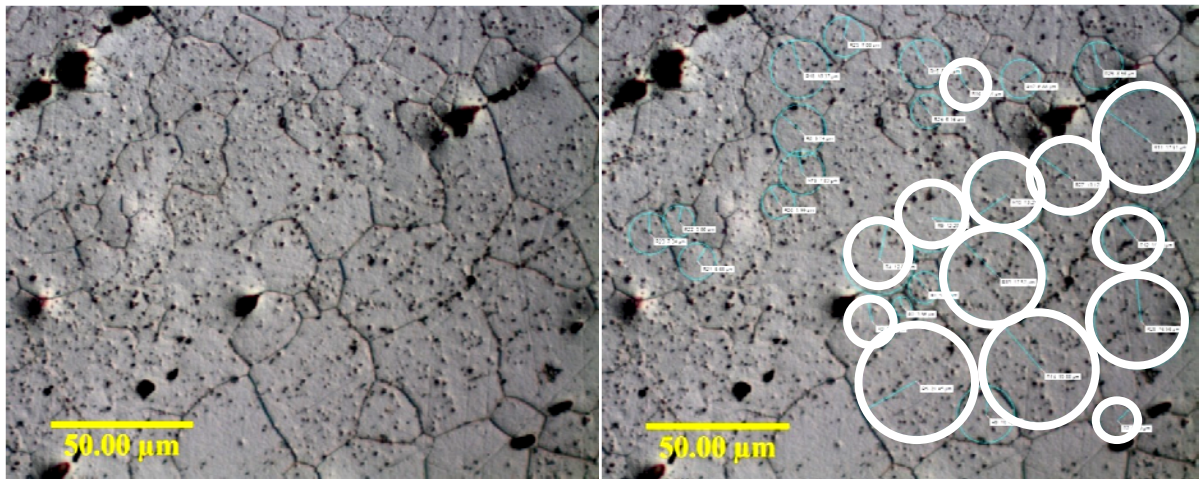


Figure 36. Location of grain width measurements in the AE42 alloy (100x magnification)

The grain width measurements were performed at ten different locations on the sample. The fields of view were randomly selected, while ensuring no overlap. The sample selection over ten fields of view gave a 95% confidence interval that the mean grain width was within $0.3\mu\text{m}$ of the calculated mean.

A 95% confidence interval was also obtained for the subgrain size measurement being in $0.3\mu\text{m}$ of the mean measured subgrain radius. The number of subgrain measurements for each alloy

6sample varied between 25 and 200. An example of subgrain diameter measurements can be seen in Figure 37.



**Figure 37. Representative example of subgrain measurements in the ZE10 alloy:
a) Captured micrograph and b) Measurements**

Similar to subgrains, twinning angles were measured manually, as illustrated in Figure 38. In this procedure, the sample was first aligned with the extrusion direction being vertical at 100x magnification, before the magnification was increased to 500x for the measurements. The angle between the extrusion direction and the twins was then measured. Measurements were taken in 15-30 areas on the sample.

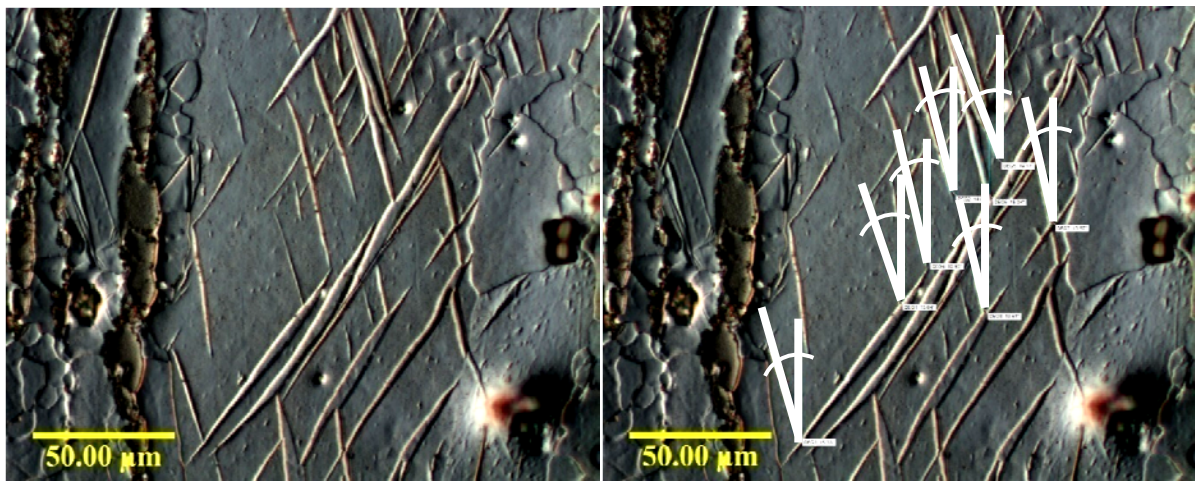


**Figure 38. Twinning measurements in the AJ32 alloy:
a) Captured micrograph and b) Measurement**

5.0 Results and Discussion

In this research, neutron diffraction was used to measure the compressive elastic creep strain of several Mg alloys. Metallographic techniques were subsequently used to characterize alloy microstructure constituents and grain morphology. Each of the techniques provided complimentary information and the results indicate that the size and shape of the intermetallic compounds in the alloys had an important effect on the alloy's creep resistance.

5.1 Neutron Diffraction

The scope of the neutron diffraction work reported in this thesis consists of two parts. Part I was conducted by Dr. Sediako in 2010 [55], and included alloy texture, strain and total deformation measurements during tensile-creep experiments at 150°C and 175°C, as well as compressive-creep experiments at 150°C. Part II involved experiments conducted by M. Fletcher for the current research and consisted of strain and total deformation measurements during compressive-creep testing at 175°C. The key results of Part I are summarized for information purposes in the following sections (5.1.1 and 5.1.2).

5.1.1 Texture Evolution and Analysis

Neutron diffraction experiments were carried out to characterize the as-extruded alloy texture. The $\{10\bar{1}0\}$ pole figures for the as-extruded AE42 and EZ33 alloys are seen in Figure 39. Both alloys showed a preferential crystallographic orientation after extrusion. The EZ33 alloy, however, exhibited a much stronger tendency for the $\{10\bar{1}0\}$ plane to align along the extrusion axis (approximately six times more) compared to the AE42 alloy [51].

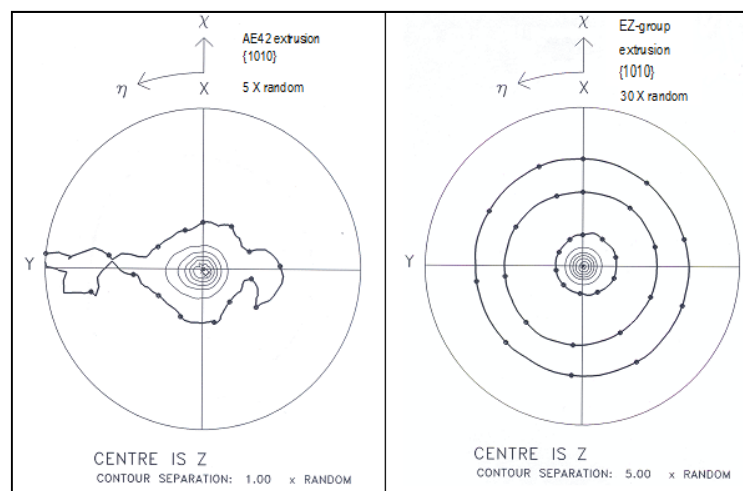


Figure 39. $\{10\bar{1}0\}$ pole figures for the: a) AE42 alloy and b) EZ33 alloy [51]

The {0002} pole figures for the AE42, AJ32, AX30 and EZ33 alloys can be seen in Figure 40. All four alloys showed typical texture for extruded Mg samples, where the basal plane aligned perpendicular to the extrusion direction. In relative terms, the EZ33, AX30 and AJ32 alloys had very strong textures, whereas the AE42 alloy had a weaker texture after extrusion [55].

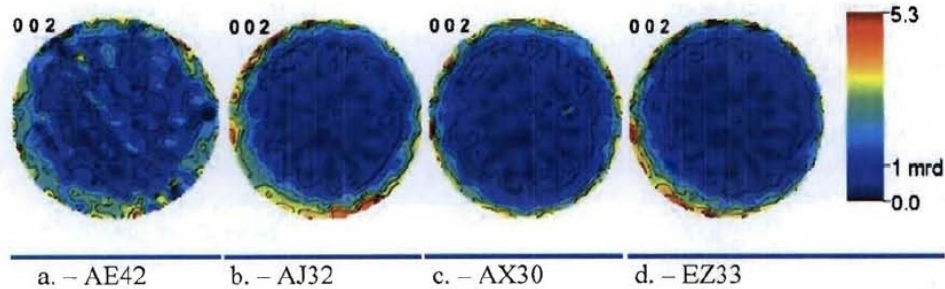


Figure 40. {0002} pole figures for the AE42, AJ32, AX30 and EZ33 alloys [55]

The textures of the AE42, AJ32, AX30 and EZ33 alloys were also analyzed after compressive and tensile-creep testing at 150°C and 175°C respectively (Figure 41). The pole figures for the AE42 alloy show minimal texture evolution after compressive creep loading; however, after tensile loading the texture evolved significantly [55]. The texture evolution of the AE42 alloy occurred through a crystallographic reorientation of grains in the material. This grain reorientation may have been caused by mechanical loading or due to the formation of subgrains with a favourable nucleation/growth direction. Reorientation of grains in the AE42, AX30 and AJ32 alloys may have been assisted by the presence of β -phase along the grain boundaries.

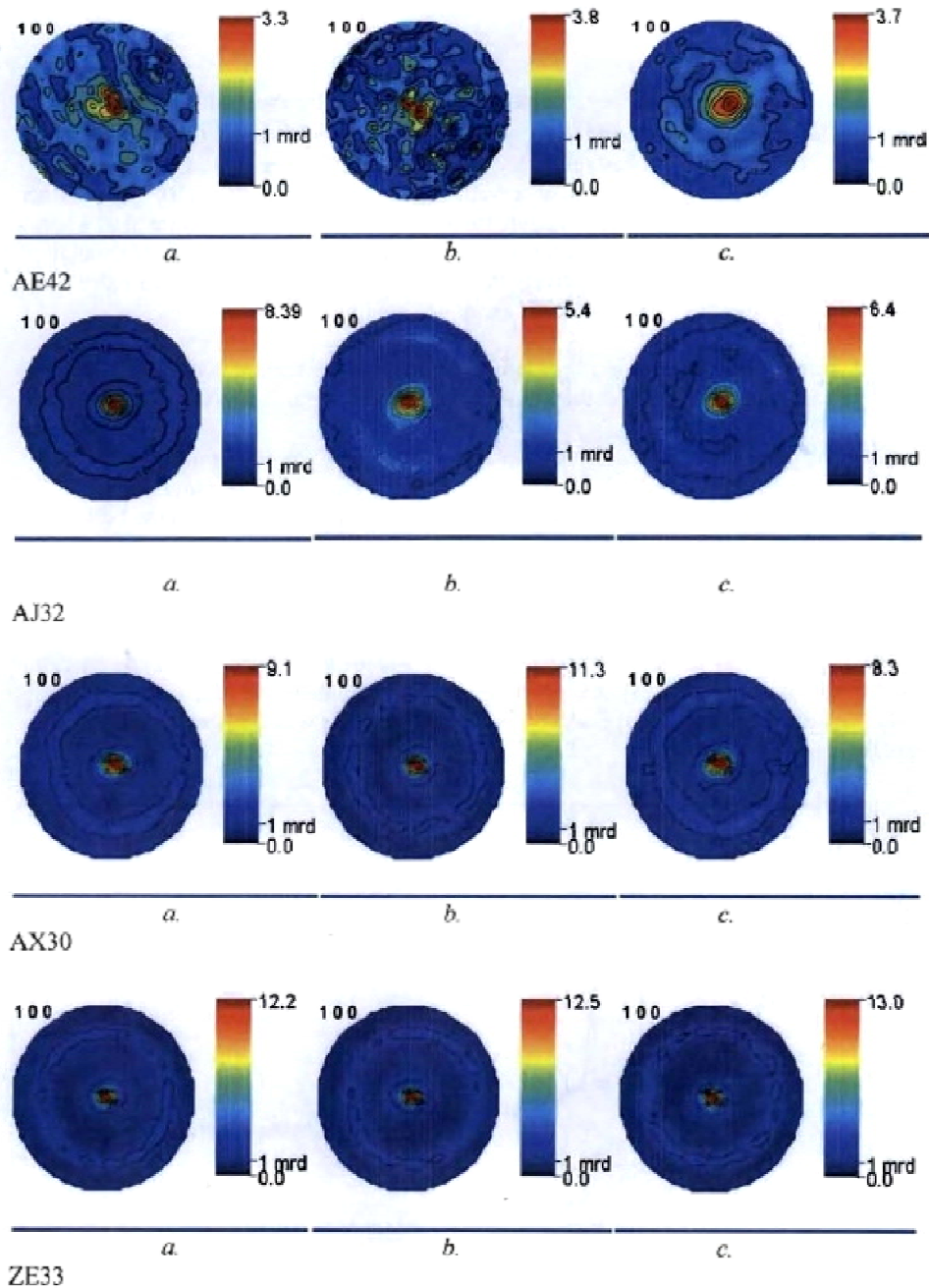


Figure 41. Texture evolution in the $\{10\bar{1}0\}$ reflection for the AE42, AJ32, AX30 and EZ33 alloys: a) As-extruded, b) Post compression-creep at 150°C and c) Post tensile-creep at 175°C conditions [55]

The AJ32, AX30 and EZ33 alloys showed a significantly lower tendency for texture evolution during tensile and compressive testing than the AE42 alloy. Thus, in qualitative terms, the alloys with stronger extrusion texture were seen to perform better during creep testing, as described in the following sections.

5.1.2 Total Creep Strain Measured Using an Extensometer

In this research, tensile and compressive-creep test was performed at 150°C and 175°C. During the creep experiments, an extensometer was used to measure the total creep (i.e., plastic and elastic) strain for each alloy. The results of the total strain analysis are discussed in the following sections.

5.1.2.1 Comparison of Total Tensile-Creep Strain at 150°C to that at 175°C

The total tensile-creep strain profiles are plotted in Figure 42. The plots clearly indicate the primary and secondary creep stages for each of the alloys. As Figure 42 illustrates, the creep strain was much higher in the Al-containing alloys compared to Al-free alloys. Further, the Al-containing alloys show a faster strain increase with time.

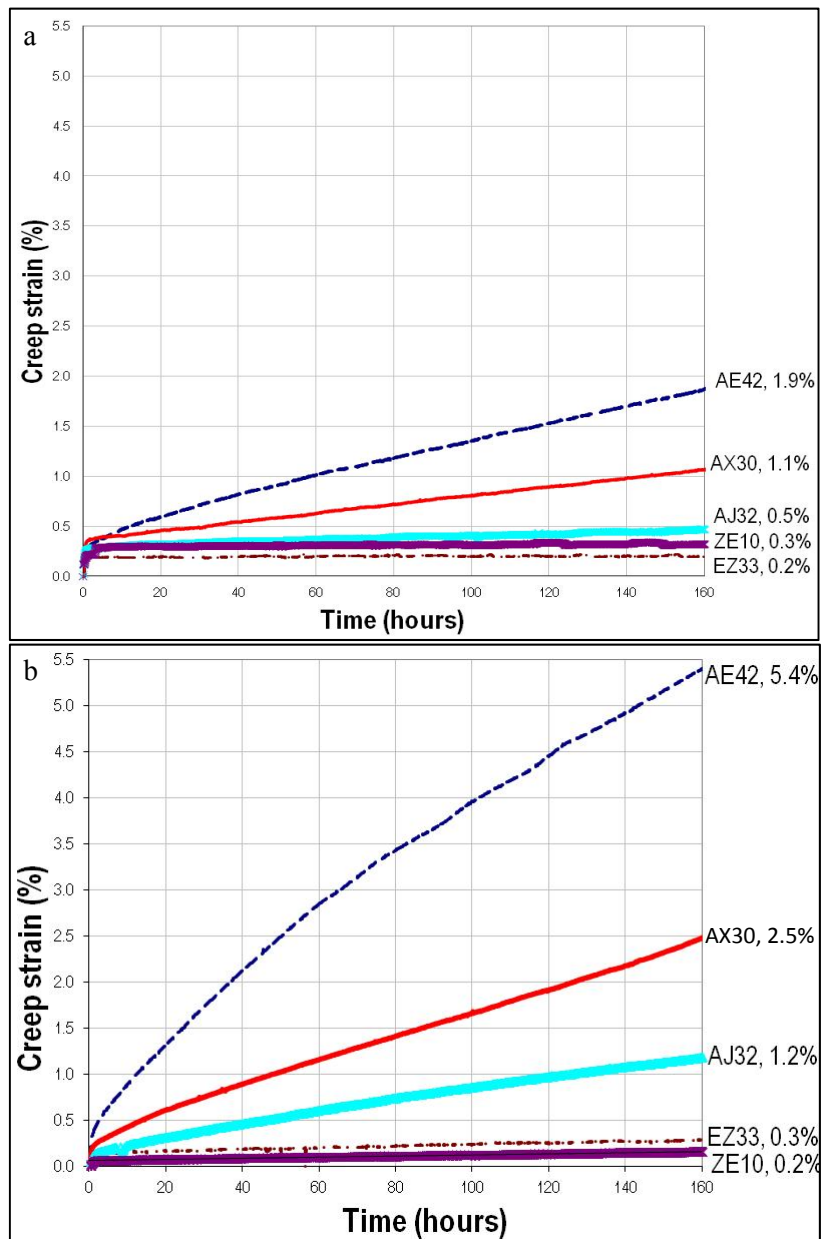


Figure 42. Tensile-creep strain vs. time at: a) 150°C and b) 175°C for the AE42, AX30, AJ32, ZE10 and EZ33 alloys

The increase in temperature from 150°C to 175°C resulted in an increase in strain by 185% in the AE42 alloy, 100% in the AJ32 alloy and the AX30 alloy, while it had no impact on the EZ33 or ZE10 alloys after 160 hours of testing. The ZE10 and EZ33 alloys performed similarly, despite the higher content of REs in the EZ33 alloy.

5.1.2.2 Comparison of Total Tensile to Total Compressive-Creep Strain at 150°C

The extensometer measurement of total strain under tensile and compressive loads at 150°C is shown in Figure 43. From these figures, it is evident that the compressive strain was significantly higher than tensile strain for the AE42, AJ32 and AX30 alloys; however, strain remained similar for

the EZ33 and ZE10 alloys. Specifically, the compressive strain of the AE42, AJ32 and AX30 alloys increased by 360%, 150% and 300%, respectively, in comparison to tensile loading.

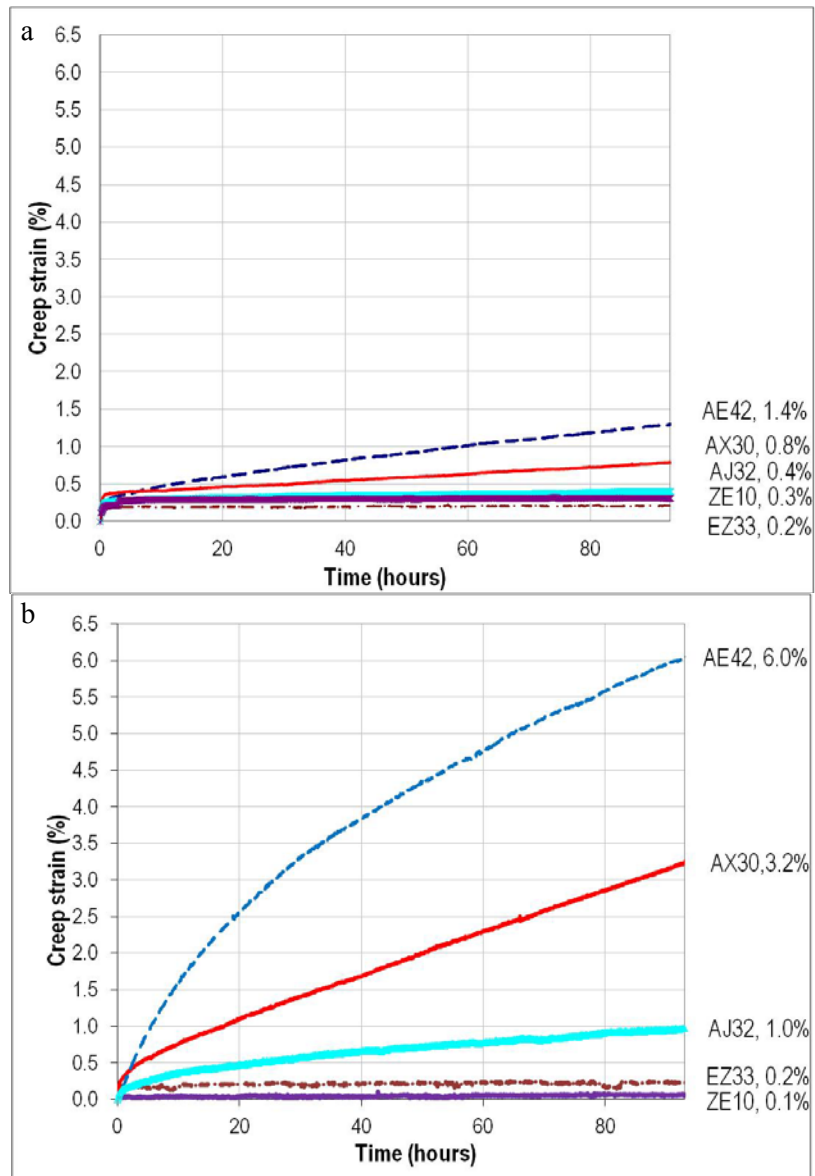


Figure 43. Total strain vs. time at 150°C under: a) Tensile loading and b) Compressive loading for the AE42, AX30, AJ32, EZ33 and ZE10 alloys

The significant increase in total strain upon compressive loading compared to tensile loading of the Al-containing extruded Mg alloys is possibly indicative of the Bauschinger effect, or due to the greater ease of twinning (or lower critical resolved shear stress) in compression rather than in tension. During extrusion, dislocations accumulated at obstacles (e.g., grain boundaries and precipitates) and hindered further tensile deformation. However, when such material was loaded in compression, the back stress in the material enabled significant material flow. The higher creep resistance of the AJ32 and AX30 alloys comparatively to the AE42 alloy is believed to be related to the presence of

thermally stable intermetallic particles in these alloys. These particles are known to impede dislocation movement and grain boundary sliding.

The EZ33 and ZE10 alloys showed very little change in response due to tensile or compressive loading, suggesting that these alloys had relatively uniform elastic properties.

5.1.2.3 Comparison of Total Compressive-Creep Strain at 150°C to that at 175°C

The compressive-creep behavior of the AE42, AJ32 and ZE10 alloys at 175°C for 23 hours is shown in Figure 44. The onset of secondary creep was qualitatively approximated for each alloy by fitting a straight line along the second half of the data points obtained during the experiments. The time at which the measured strain no longer conformed to the trend line (Figure 45) was identified as the onset of secondary creep. This onset was at eight, five and ten hours into the creep test for the AE42, AJ32 and ZE10 alloys, respectively. The strain rates during secondary creep show that the AE42 alloy deformed fastest followed by the AJ32 and ZE10 alloys.

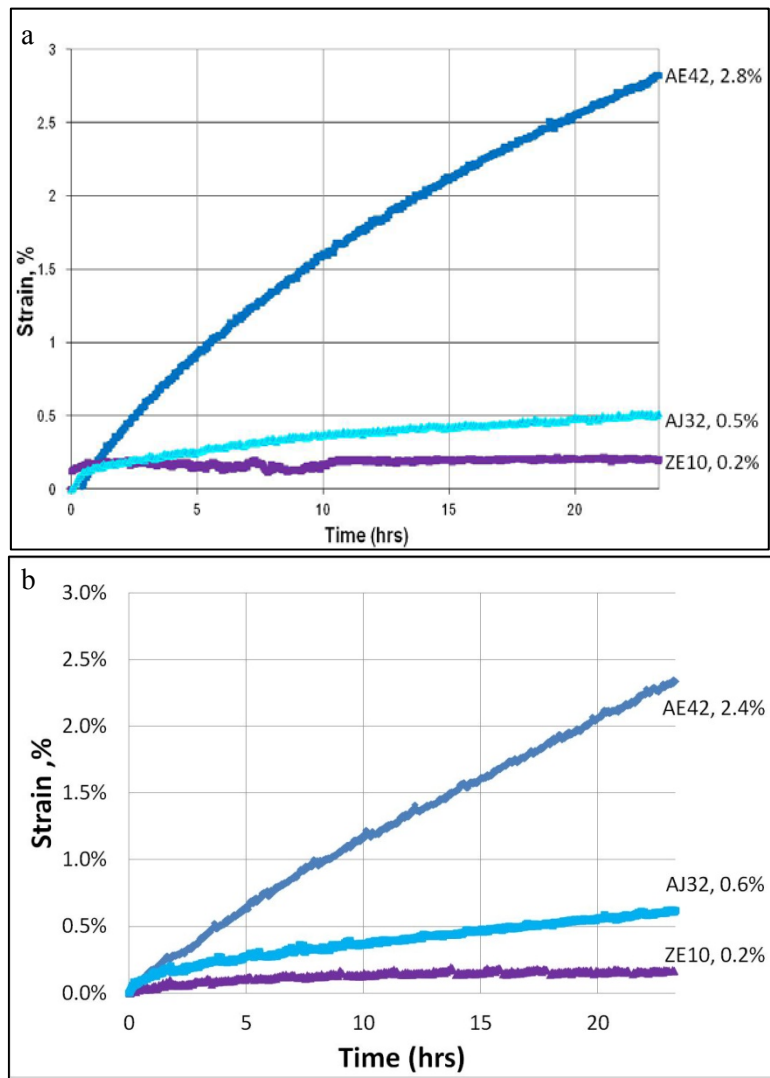


Figure 44. Total compressive-creep strain vs. time at: a) 150°C and b) 175°C for the AE42, AJ32 and ZE10 alloys

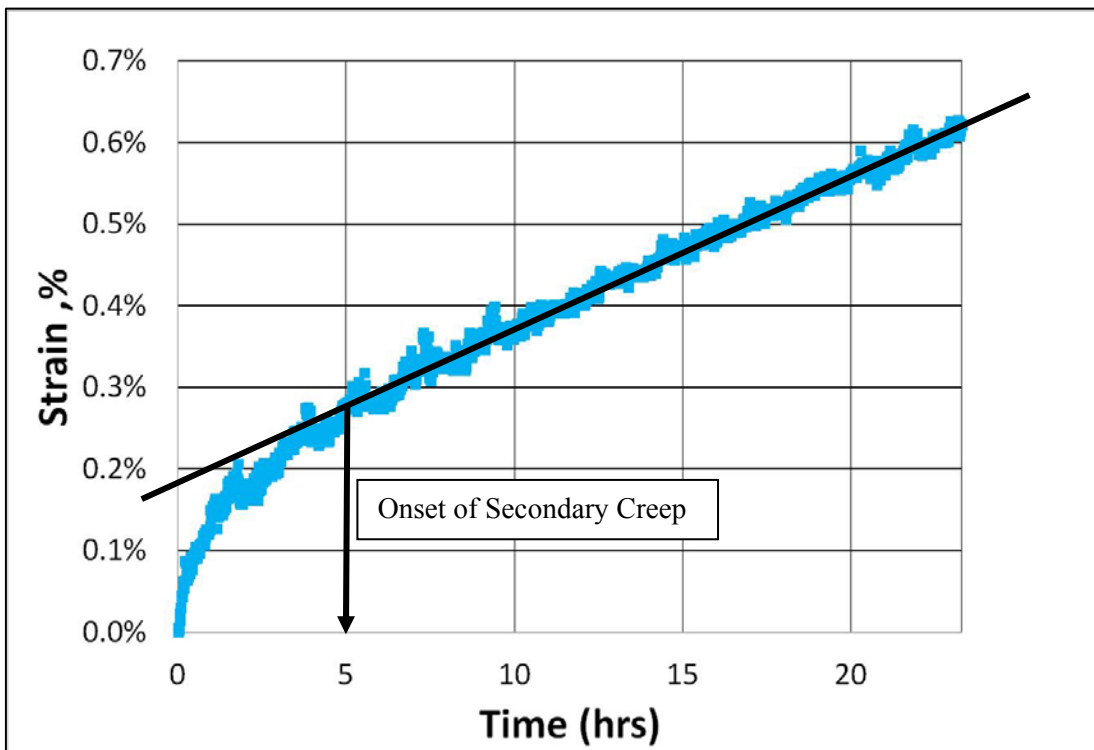


Figure 45. Onset of secondary creep in the AJ32 alloy

The comparison of compressive-creep deformation at 150°C to 175°C after 23 hours is shown in Figure 44. In contrast to the tensile results discussed thus far, it appears that a temperature increase of from 150°C to 175°C had no significant impact on the compressive creep resistance of the alloys under investigation.

5.1.2.4 Comparison of Total Tensile to Total Compressive-Creep Strain at 175°C

A comparison between the tensile and compressive-creep curves of total strain vs. time is given in Figure 46. As can be seen in this figure, all alloys have experienced higher strains under compressive-creep testing than in tensile-creep testing at 175 °C. Upon compression, the strains of the AE42, AJ32 and ZE10 alloys increased by 70%, 100% and 100%, respectively, relative to their tensile counterparts. As was already discussed with respect to experiments conducted at 150 °C, it is suspected that the Bauschinger effect was responsible for the significant increase in compressive creep strain magnitude.

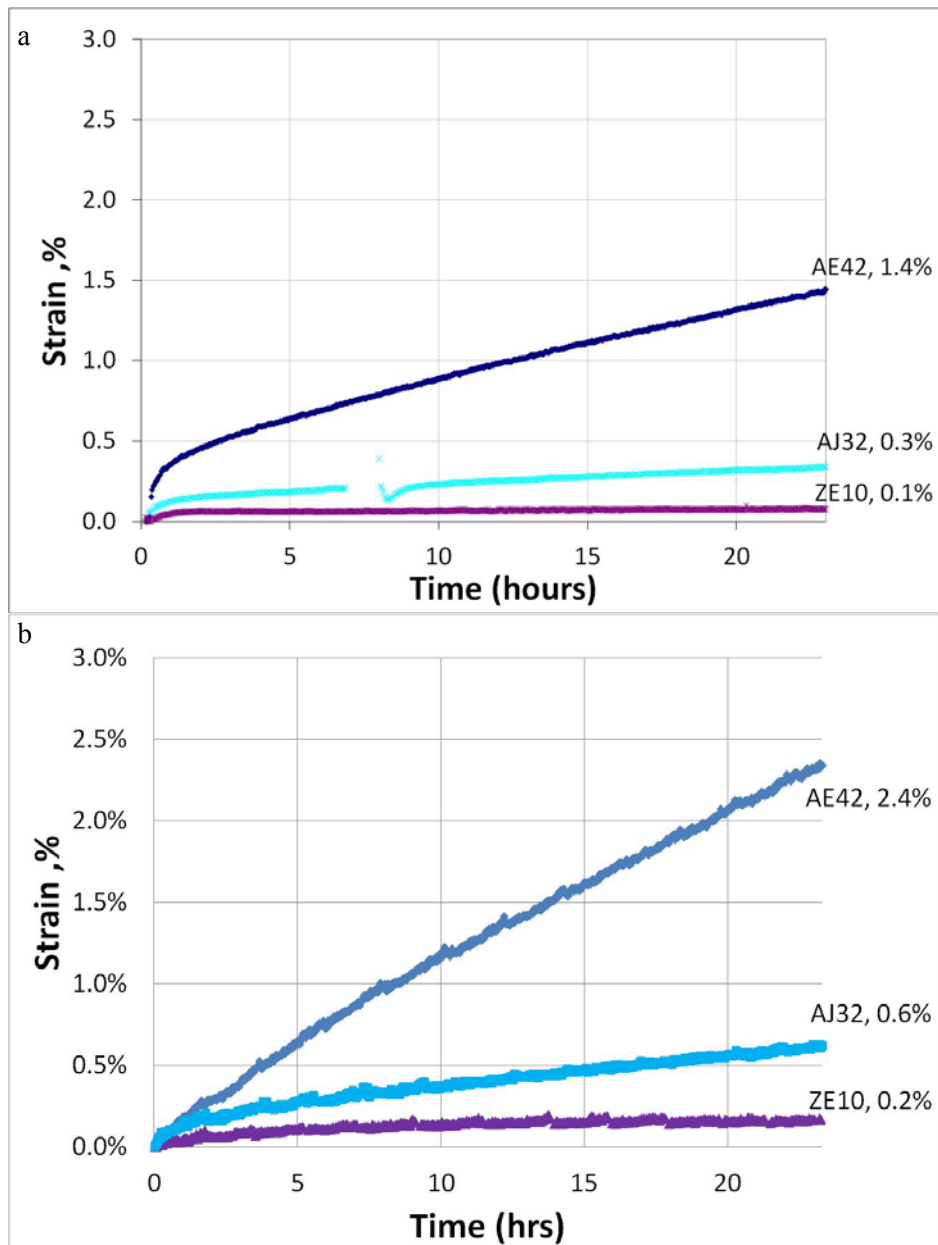


Figure 46. Total creep strain vs. time at 175°C for AE42, AJ32 and ZE10 alloys: a) Tensile creep and b) Compressive creep

5.1.2.5 Summary of Total Strain Measurements

A normalized ranking (with respect to the industrial benchmark AE42 alloy) of the AJ32, AX30, EZ33 and ZE10 alloys under tensile and compressive-creep conditions at 150°C and 175°C is shown in Figure 47. As seen in the figure, the AE42 alloy was ranked the lowest (5), followed by AX30 (4), AJ32 (3), ZE10 (2) and EZ33 (1).

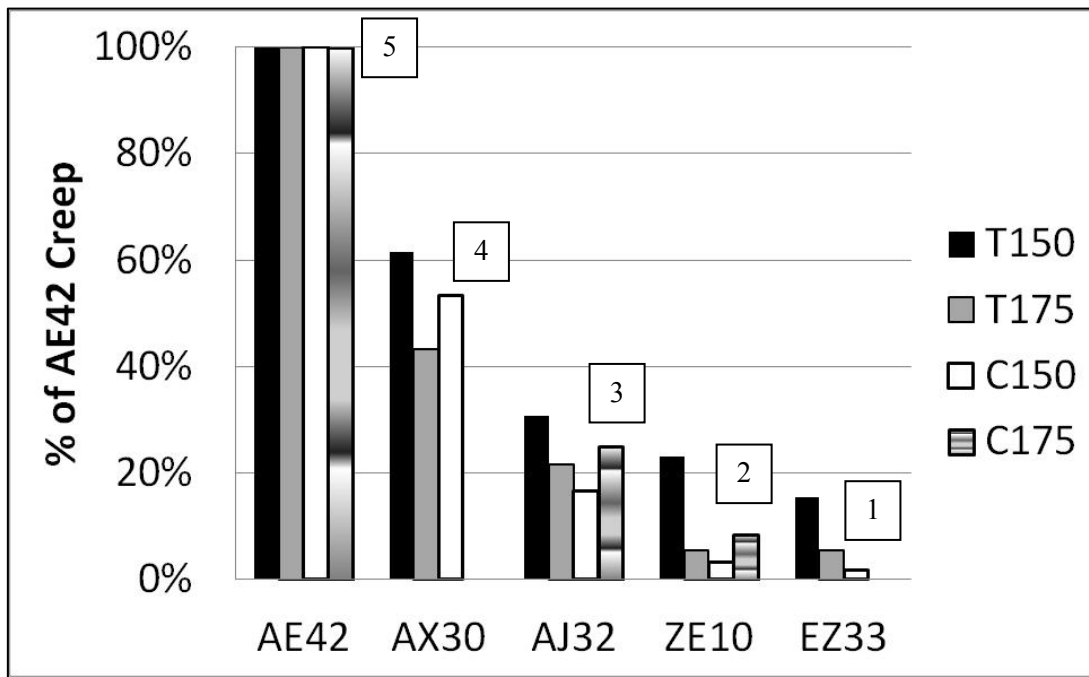


Figure 47. Normalized creep strains of the AX30, AJ32, ZE10 and EZ33 alloys with respect to the AE42 alloy

These results suggest that although AE42 is the industry benchmark alloy, suitable alloying of magnesium can significantly improve the creep performance of Mg-based materials. In particular, removing aluminum from the system appears to be an important step. This alloying change, however, would affect the room temperature strength of the alloy. Consequently, these results suggest that operating temperature-specific alloy may be necessary for industrial applications.

5.1.3 Elastic Creep Microstrain Measured Using Neutron Diffraction

Microstrain measurements were performed in conjunction with extensometer measurements during creep testing. These microstrain measurements quantified the elastic crystallographic lattice strain. The results are listed and discussed in the following sections. The primary assumption made in this analysis was that the strain in the sample volume was homogeneous, not taking into effect strain changes from the interior of the grain to the grain boundaries.

5.1.3.1 Tensile-Creep Elastic Microstrain at 150°C and 175°C

Creep testing completed by Dr. Sediako (Part I) consisted of the elastic microstrain measurements for the $\{10\bar{1}0\}$ plane of AE42 and EZ33 alloys. The elastic microstrain and total material strain results obtained for tensile-creep testing at 150°C are shown in Figure 48. As expected for thermal and tensile elastic strain, an increase in temperature increased the lattice spacing for both AE42 and EZ33 alloys. The subsequent application of a tensile load increased the lattice spacing further. Under a constant load and constant temperature, the lattice strains remained constant for both alloys; however, the total alloy strain continued to increase for both alloys for the duration of the

creep test. On the lowering of the applied load and temperature, the AE42 lattice strain returned to zero, indicating that no residual stresses remained in the alloy. The lattice strain for EZ33 did not return to zero after testing, indicating the presence of residual strain on the order of 500 microstrain in the EZ33 material.

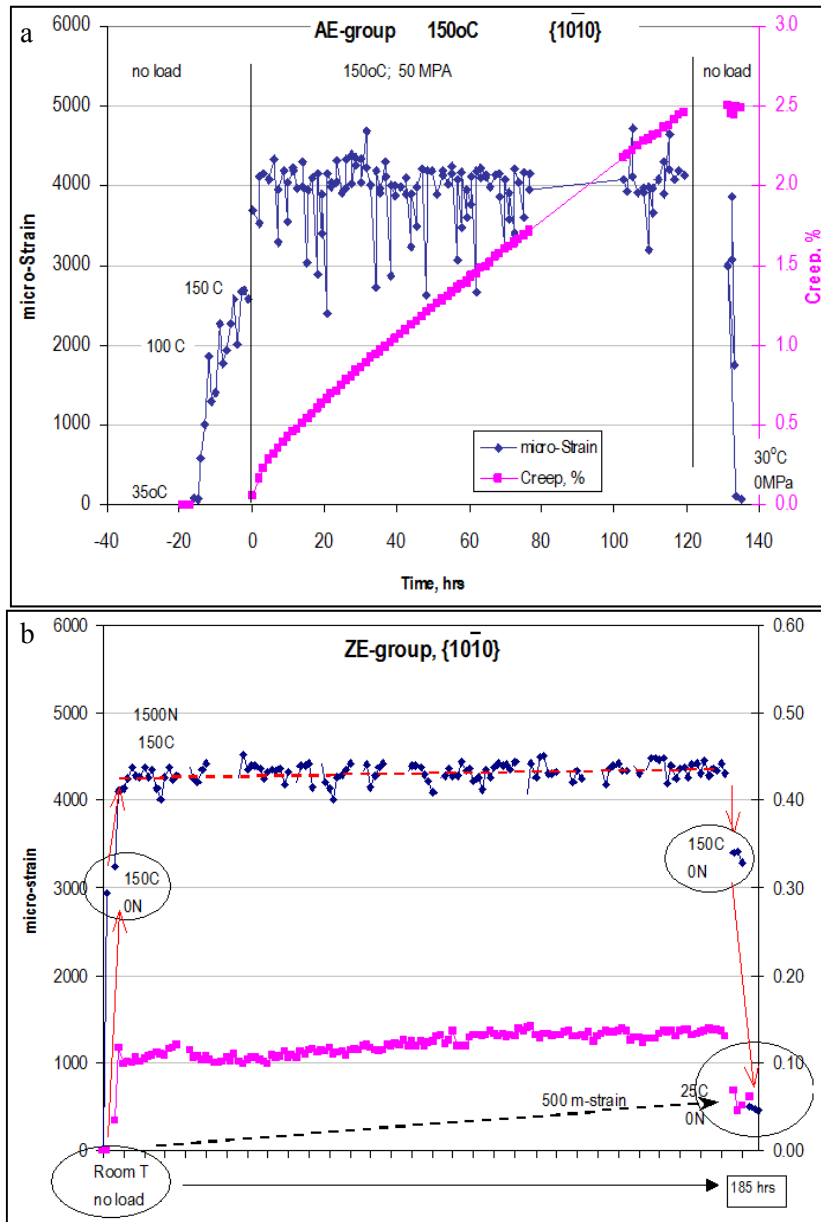


Figure 48. In-situ strain evolution for $\{10\bar{1}0\}$ crystallographic plane in: a) AE42 alloy and b) The EZ33 alloy [51]

The constant elastic strain and ever increasing material deformation (measured with an extensometer) during tensile-creep testing suggests that material deformation under creep conditions was accommodated by plastic deformation. The absence of residual strains in the AE42 alloy after unloading suggested that no intergranular residual strains were retained. The lack of intergranular

residual strains suggests that grain boundary sliding occurred, releasing the stress between grains. Another explanation for the lack of residual strains would be the occurrence of twinning in the alloy during testing, thus reorienting the lattice to allow for material slip. The residual strain present in the EZ33 alloy suggests that the grains were likely pinned together during creep deformation. The residual strain in the EZ33 alloy may also be the result of strain hardening due to the nanoprecipitates present in the alloy. This conclusion, however, warrants further study.

5.1.3.2 Compressive-Creep Elastic Microstrain at 175°C

During Part II of this research, the lattice spacing of the $\{10\bar{1}0\}$, $\{0002\}$, $\{10\bar{1}1\}$, $\{10\bar{1}2\}$ and $\{2\bar{1}\bar{1}0\}$ planes was measured for the AE42, AJ32 and ZE10 alloys. Thus, the thermal and mechanical strains during creep testing at 175°C and under a 50 MPa load were measured. Due to the extruded texture of the alloys, the neutron diffraction data gained from the $\{0002\}$ and $\{10\bar{1}2\}$ planes had a low intensity, resulting in neutron plots where the peak was unclear and gave a low confidence in the measured diffraction angle. Such peaks where the diffraction angles could not be accurately measured possibly increased the error (uncertainty) in the calculated strain values.

A comparison of the calculated lattice spacing for the $\{2\bar{1}\bar{1}0\}$, $\{0002\}$ and $\{10\bar{1}2\}$ planes for AE42 can be seen in Figure 49. As is shown in the figure, the lattice spacing of the $\{2\bar{1}\bar{1}0\}$ plane expanded under a temperature increase and subsequently contracted due to the compressive load, as expected. Both the $\{10\bar{1}2\}$ and $\{0002\}$ planes however, had erratic behaviour with random fluctuations in creep strain during the test.

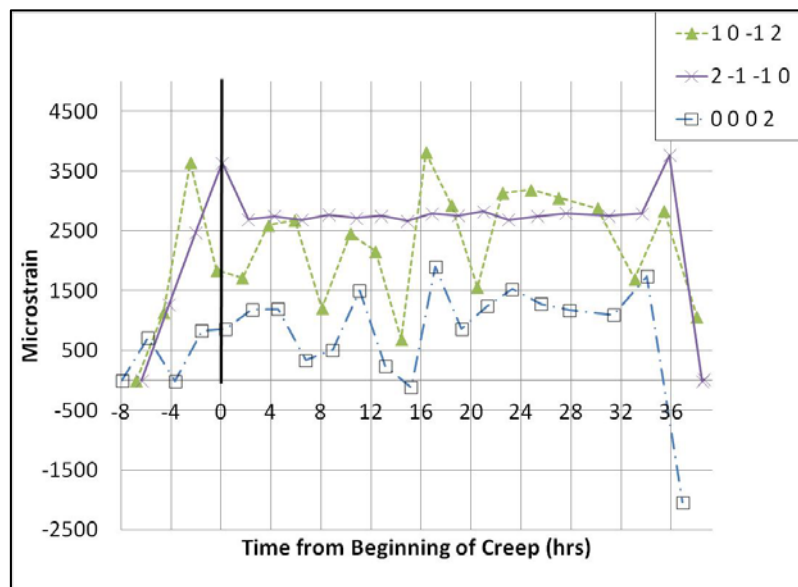


Figure 49. The $\{10\bar{1}2\}$, $\{0002\}$ and $\{2\bar{1}\bar{1}0\}$ microstrain in the AE42 alloy

The compressive lattice strains for the $\{10\bar{1}0\}$, $\{10\bar{1}1\}$ and $\{2\bar{1}\bar{1}0\}$ planes are presented in Figure 50, with the error bars indicating the standard deviation of the data points. In each figure, the lattice spacing increased under heating to 175°C, as a result of the materials' thermal expansion. The lattice strain then decreased upon the application of a 50MPa compressive load and returned to the initial level on the release of the compressive load and cooling to 25°C.

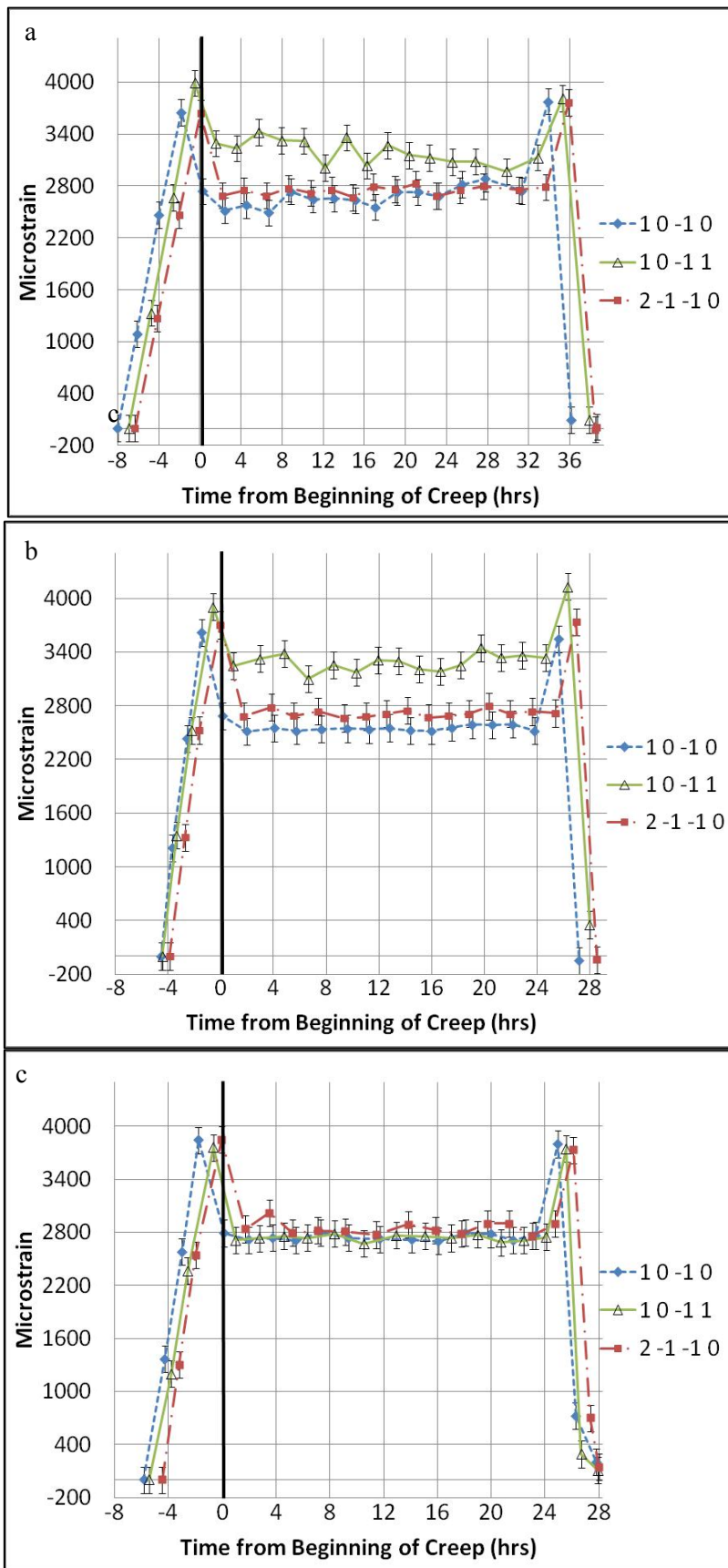


Figure 50. Lattice strains for the $\{10\bar{1}0\}$, $\{10\bar{1}1\}$ and $\{2\bar{1}\bar{1}0\}$ planes for the: a) AE42 alloy, b) AJ32 alloy and c) ZE10 alloy

The AE42 alloy shows a significant variation in lattice strains during creep testing: The $\{10\bar{1}0\}$ plane shows a strain relaxation (of approximately 11%) and the $\{10\bar{1}1\}$ plane shows a strain increase (of approximately 8%) under a constant load and temperature. This non-uniform lattice behaviour begins approximately eight hours after the beginning of the creep test and coincides with the onset of secondary creep. The changes in lattice strain may be due to a reorientation of the crystal lattice due to twinning or grain/subgrain rotation. The strain variations may also be due to the formation of β -phase and the degradation of $Al_{11}RE_3$, which will be discussed in detail in section 5.2. The changes in the lattice orientation and the continuous change of the composition of intermetallic compounds resulted in the constant modification of the material, causing the lattice spacing to change with time. In other words, the AE42 alloy at the beginning of the creep test was not the same as that at the end of the creep test.

In the AE42 alloy, an elastic anisotropy of the strains was seen in addition to variations in the lattice strains with respect to time. The elastic anisotropy took the form of the $\{10\bar{1}1\}$ plane compressing less than both the $\{10\bar{1}0\}$ and $\{2\bar{1}\bar{1}0\}$ planes. Similar elastic anisotropy was observed for the AJ32 alloy. This may be due to intermetallics forming on preferred crystallographic planes, restricting compression (strain) on the $\{10\bar{1}1\}$ plane.

Figure 50b and c also show that the lattice strains for AJ32 and ZE10 remained constant during creep deformation. ZE10 showed stable elastic strain during the entire creep test, with all three planes being seemingly unaffected by the time-dependant high temperature exposure. This result is consistent with the measurements made with an extensometer.

Recalling that the AE42 and AJ32 alloys showed monotonic increasing strain during creep testing (as measured with the extensometer), and relatively stable elastic strains, then the majority of the deformation experienced by the alloys was likely the result of plastic deformation. The lack of residual stress in any of the aluminum-containing alloys at the end of creep testing further supports this assumption, since grain boundary sliding during creep testing would effectively alleviate residual strains in the material.

5.1.3.3 Summary of Elastic Microstrain Measurements

The presence of residual strain under tensile (but not compressive) loading is an indicator of the Bauschinger effect in the extruded alloys. Dislocations likely accumulated at obstacles during extrusion and hindered further tensile deformation. The tensile loads increased the number and intensity of dislocation accumulations⁷ in the material, resulting in residual stresses in the material. The compressive load (studied in this research) however, worked with the back stress in the material to deform the material compressively, annihilating dislocations created in tension. A transmission

electron microscopy (TEM) study would be invaluable to validate this hypothesis and quantify the dislocation densities in materials subjected to tensile and compressive loads.

5.2 Metallographic Analysis

Metallographic analysis was performed on each alloy in the as-extruded and post compressive-creep conditions. The analysis of the as-extruded and post compressive-creep specimens included a measurement of the grain widths, subgrain radii and twinning angles using image analysis. The metallographic characterization also included SEM analysis of the intermetallic constituents and solute segregation. These results are presented in the following sections.

5.2.1 Grain Boundary Analysis Using Optical Microscopy

All five alloys studied in this research exhibited mechanical texture resulting from the extrusion process. This mechanical texture took the form of elongated grains in the extrusion direction, with the intermetallics aligning along the grain boundaries and, in some alloys, intermetallics were forced into the interior of the grains. Representative micrographs of the radial and cross-section directions are given in Figure 51, where the extrusion direction was vertical in Figure 51a.

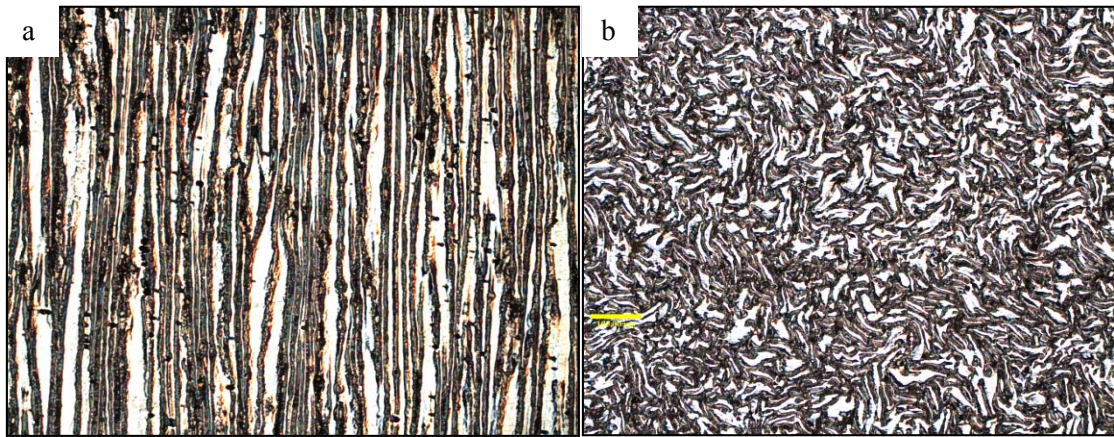


Figure 51. Representative microstructure in: a) Cross-section direction and b) Radial direction (AJ32 alloy at 50x magnification)

Micrographs of the cross-sections of AE42, AJ32, AX30, EZ33 and ZE10 alloys at 100x magnification are given in Figure 52.

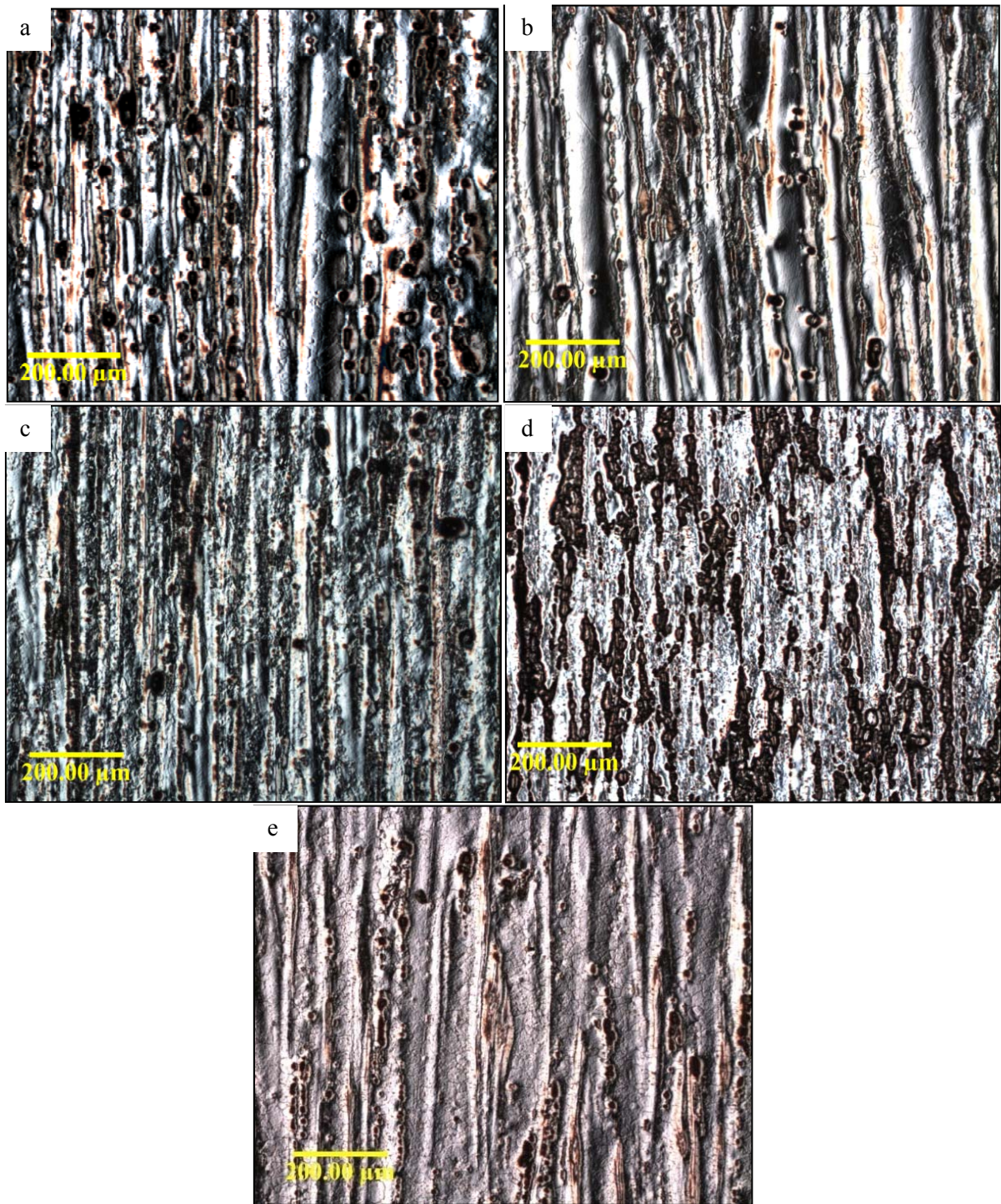


Figure 52. Representative micrographs for the cross-section samples of the: a) AE42 alloy, b) AJ32 alloy, c) AX30 alloy, d) EZ33 alloy and e) ZE10 alloy

The grain widths of each alloy were measured using Buehler OmniMet software and are reported in Figure 53 (raw data can be found in Table 12), with the error bars showing the 95% confidence interval. No significant change in grain width was found between the as-extruded and post compressive-creep material samples. ANOVA statistical analysis was performed on the raw measurements (Table 8) and confirmed to a 95% confidence interval that the grain widths changed

from alloy to alloy, but did not change between the as-extruded and post-creep states. This indicates that the grains did not widen or contract during creep testing at 175°C.

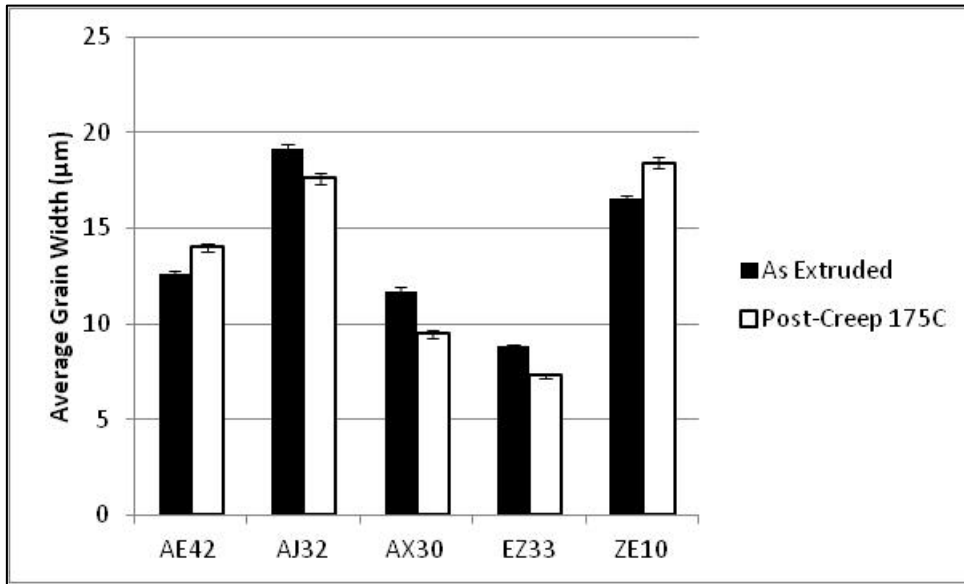


Figure 53. Average grain widths for the AE42, AJ32, AX30, EZ33 and ZE10 alloys in their as-extruded and post-creep conditions

Table 8. ANOVA analysis of the effect of alloy composition and creep on the alloy grain width

ANOVA						
Source of Variation	SS	df	MS	F	P-value	F crit
Alloy to Alloy	154.70736	4	38.67684	21.64054	0.00568	6.388233
AE vs. PC	0.37249	1	0.37249	0.208416	0.671702	7.708647
Error	7.14896	4	1.78724			
Total	162.22881	9				

The number of data points used to calculate the average grain width was at least 11500 and as high as 23000. The average grain width had a large standard deviation, due to the shape of the elongated grains in the material. However, with a large number of data points, an accuracy of the average grain width, to within 0.3 µm, was obtained.

Larger grains are known to be advantageous during high temperature applications, due to the decrease in the number of grain interfaces available for grain boundary sliding. This appears to be the case with the AJ32 alloy, which had the widest grains of the Al-containing alloys. However, AE42 had the second largest grains out of the Al-containing alloys and it experienced the highest creep strain, indicating that the grain size was not the only contributing factor to creep resistance in the alloys.

EZ33 and ZE10 alloys had similar creep resistances in the neutron diffraction experiments; however, they had significantly different grain sizes. The ZE10 grains were over two times larger

than those of the EZ33 alloy. Again, this result suggests that the grain size alone was not the determining factor for creep resistant behavior of these alloys.

5.2.2 Subgrain Size Analysis Using Optical Microscopy

Subgrains were found in all alloys in the as-extruded and post-creep conditions. Representative micrographs of the as-extruded alloys are provided in Figure 54. Electron backscatter diffraction analysis should be performed to determine whether the subgrains were indeed subgrains or recrystallized grains. It is worth noting, however, that the temperature of testing did not reach half of the melting point for the alloys, hence it is unlikely that recrystallization occurred during creep testing. Thus, if the subgrains did not form through a thermal process, they may have formed during the extrusion processing.

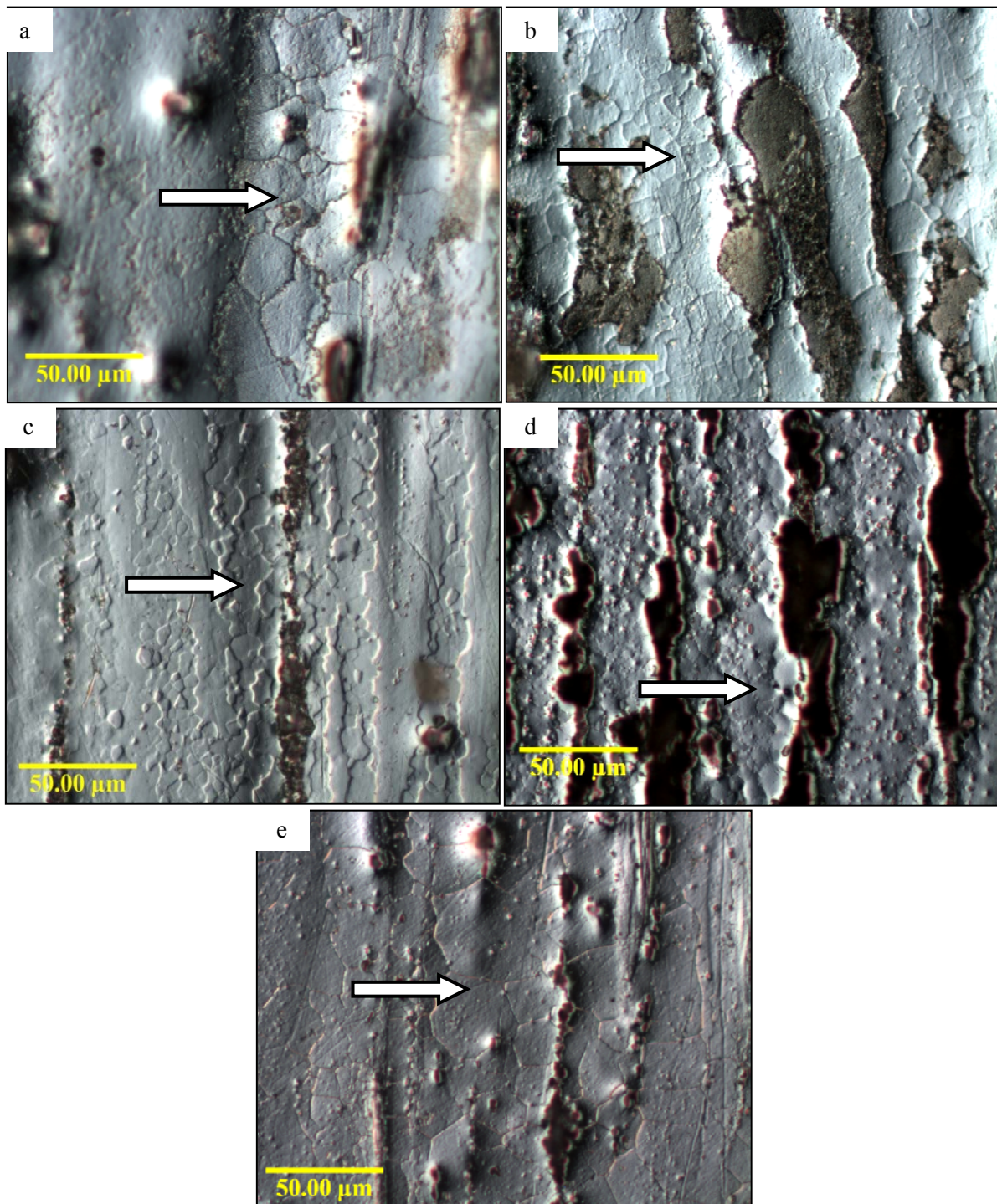


Figure 54. Subgrains in the as-extruded: a) AE42 alloy, b) AJ32 alloy, c) AX30 alloy, d) EZ33 alloy and e) ZE10 alloy

The average subgrain radii are plotted for each alloy in Figure 55, with error bars indicating the 95% confidence interval. Again, the results suggest that the subgrains did not change in size between the as-extruded and post-creep conditions. However, the subgrain sizes varied significantly between alloys. An ANOVA analysis was performed on the subgrain radii measurements to confirm this observation and the results are given in Table 9.

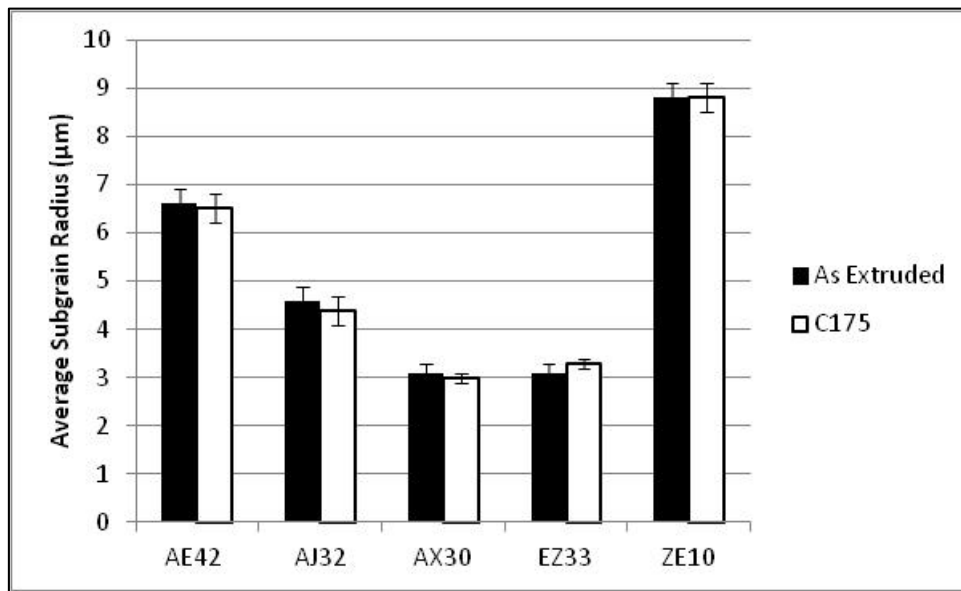


Figure 55. Average subgrain radii in the AE42, AJ32, AX30, EZ33 and ZE10 alloys in their as-extruded and post-creep conditions

Table 9. ANOVA analysis of the effect of alloy composition and creep on the alloy subgrain sizes

Source of Variation	SS	df	MS	F	P-value	F crit
Alloy to Alloy	47.786	4	11.9465	1038.826	2.77E-06	6.388233
AE vs. PC	0.004	1	0.004	0.347826	0.58705	7.708647
Error	0.046	4	0.0115			
Total	47.836	9				

Out of the Al containing alloys, AE42 had the largest subgrain size and the lowest creep resistance, while the AX30 had the smallest subgrains and the second lowest creep resistance. Thus, no direct relation was observed between subgrain size and the creep resistance. Similarly to the grain widths, ZE10 had significantly larger subgrains than EZ33 (approximately three times larger), yet there was no visible change in creep resistance between EZ33 and ZE10 alloys in the neutron diffraction experiments. Thus, the subgrains possibly did not influence the creep resistance of the alloys.

5.2.3 Twinning Analysis Using Optical Microscopy

Twins were found in the AE42, AJ32 and AX30 alloys in both the as-extruded and post-creep conditions. Representative micrographs are provided in Figure 56. Twinning was not found in EZ33 or ZE10 alloys in their as-extruded conditions, but only in the post-creep condition (Figure 56). The angles between the twins and the extrusion direction are plotted in Figure 57, with error bars depicting the 95% confidence interval, for the AE42, AJ32 and AX30 alloys in their as-extruded and post-creep conditions. The twinning angles for the EZ33 post-creep alloy were not measured, due to the lack of sufficient twinning in the grains to measure the twinning angles accurately.

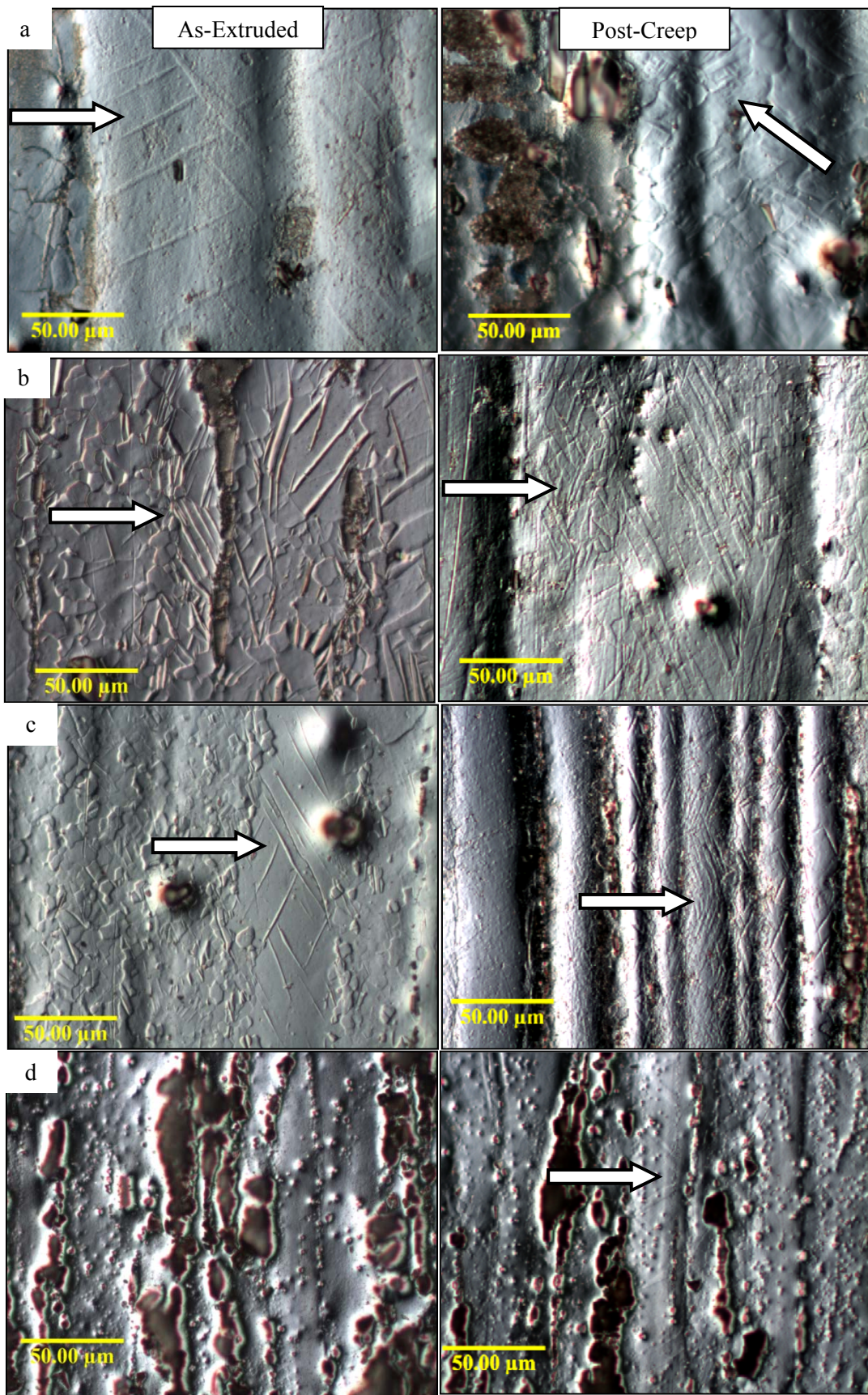


Figure 56. As-extruded and post-creep twinning in the: a) AE42 alloy, b) AJ32 alloy, c) AX30 alloy and d) EZ33 alloy

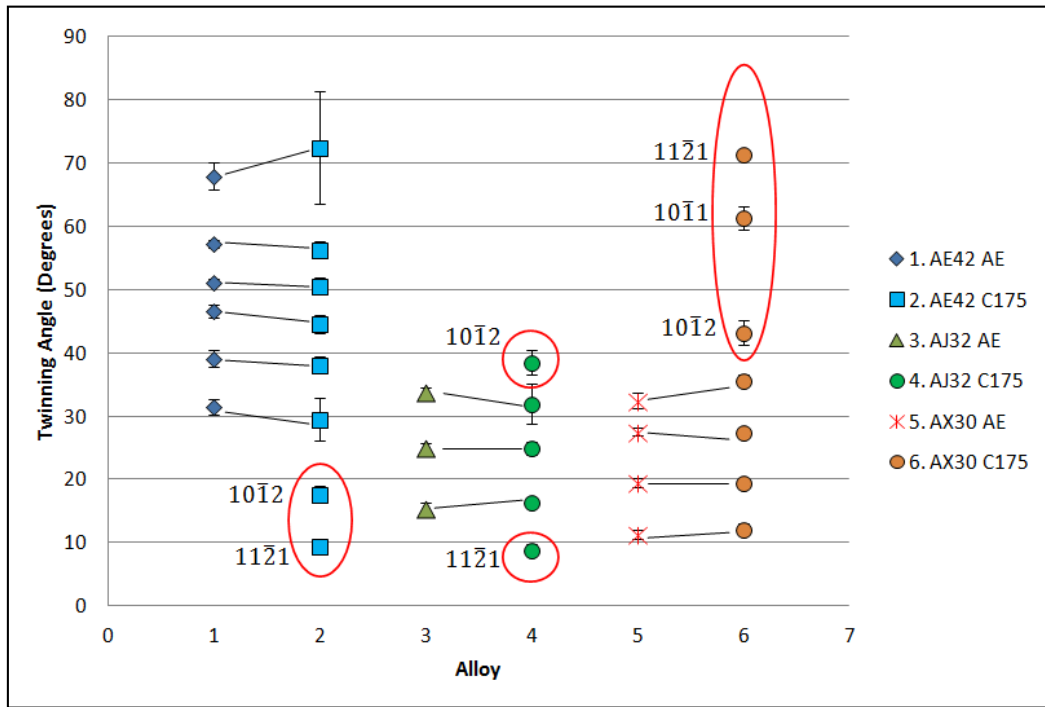


Figure 57. Twinning angles relative to extrusion direction in the AE42, AJ32 and AX30 alloys

Theoretical twinning angles were calculated for HCP twinning on the $\{10\bar{1}0\}$, $\{10\bar{1}1\}$, $\{10\bar{1}2\}$, $\{2\bar{1}\bar{1}0\}$ and $\{11\bar{2}1\}$ planes. The angles between these planes and the basal plane were calculated using Equation 4 to give the theoretical twinning angles. The Mg lattice parameters used were $a=3.21 \text{ \AA}$ and $c= 5.21 \text{ \AA}$.

$$\cos(\phi) = \frac{\mathbf{h}_1\mathbf{h}_2 + \mathbf{k}_1\mathbf{k}_2 + 0.5(\mathbf{h}_1\mathbf{k}_2 + \mathbf{h}_2\mathbf{k}_1) + \frac{3a^2}{4c^2}\mathbf{l}_1\mathbf{l}_2}{\sqrt{\left(\mathbf{h}_1^2 + \mathbf{k}_1^2 + \mathbf{h}_1\mathbf{k}_1 + \frac{3a^2}{4c^2}\mathbf{l}_1^2\right)\left(\mathbf{h}_2^2 + \mathbf{k}_2^2 + \mathbf{h}_2\mathbf{k}_2 + \frac{3a^2}{4c^2}\mathbf{l}_2^2\right)}} \quad (4)$$

Due to the crystallographic symmetry of the HCP crystal, multiple angles were possible for each plane. The theoretical twinning angles for the HCP crystal are summarized in Table 10.

Table 10. Theoretical twinning angles

Plane	Twinning Angle (θ)
$10\bar{1}0$	30
	90
$10\bar{1}1$	62
	58
$10\bar{1}2$	43
	17
	77
$2\bar{1}\bar{1}0$	30
	90
$11\bar{2}1$	13
	47
	73

The twins observed in the alloys had a lens shape, indicating that they were mechanical twins produced during mechanical loading rather than thermal loading. The twins observed in the as-extruded alloys were therefore produced as a result of the high stresses involved in the extrusion process. The increase in the number of lens shaped twins in the post-creep compared to the as-extruded samples indicates that the 50 MPa applied load during creep activated new twin systems.

The as-extruded AE42 alloy exhibited twinning on six different planes. This alloy had the largest number of twins observed of all the studied alloys. For the AE42 and AJ32 alloys, two new twinning angles were identified in their post-creep conditions. Specifically, twinning on the ($10\bar{1}2$) and ($11\bar{2}1$) planes was initiated during creep. AX30 contained three extra twinning planes in the post-creep condition on the ($10\bar{1}2$), ($11\bar{2}1$) and ($10\bar{1}1$) planes. For Mg alloys the ($10\bar{1}2$) and ($10\bar{1}1$) planes are the usual twinning planes [11].

Although no significant difference in creep resistance has been observed between the EZ33 and ZE10 alloys in this research, the appearance of twins in the EZ33 alloy and not in the ZE10 alloy after creep testing suggests that the EZ33 alloy may be more susceptible to plastic deformation than the ZE10 alloy.

A correlation was identified between the twinning susceptibility and the crystallographic texture. Although each alloy exhibited extrusion texture, where the normal of the basal plane aligned perpendicular to the extrusion direction, the strength of this texture varied for each alloy. The weakest

texture was observed in the AE42 alloy, and the strongest texture was in the ZE10 alloy. With the strong texture of the ZE10 alloy, the c-axis was likely perpendicular to the extrusion direction, resulting in a high resistance to material twinning. However, the weaker textures observed in the Al-containing alloys, resulted in orientation of crystals where the c-axis was not perfectly perpendicular to the extrusion direction, providing an opportunity for the material to twin along the pyramidal planes. Therefore, the higher the strength of extrusion texture, the lower the susceptibility to material twinning, and a resulting increase in creep resistance.

The observed twins terminated at the grain boundaries, subgrain boundaries and intermetallic compounds, as seen in Figure 56. The twinning direction changed between adjacent subgrains and grains. Cumulatively, grain boundary sliding and material slip, accompanied by twinning, suggests that multiple mechanisms were responsible for plastic deformation in the alloys.

5.2.4 Characterization of Intermetallic Compounds

Representative SEM micrographs of the as-extruded AE42, AJ32, AX30, EZ33 and ZE10 alloys can be seen in Figure 58 (additional micrographs are provided in Appendix C.2 – Scanning Electron Microscopy). A summary of the general morphology of the intermetallics is provided in Table 11. XEDS analysis was performed on the intermetallics in the AE42, AJ32 and ZE10 alloys, in order to estimate their stoichiometry.

Table 11. General morphology of intermetallic compounds in the AE42, AJ32, AX30, EZ33 and ZE10 alloys

Alloy	Morphology of Intermetallic Compounds
AE42	Cuboid
	Acicular
AJ32	Blocky
	Plate shaped
	Acicular
AX30	Acicular
	Blocky
EZ33	Irregular
	Fine
ZE10	Irregular
	Fine

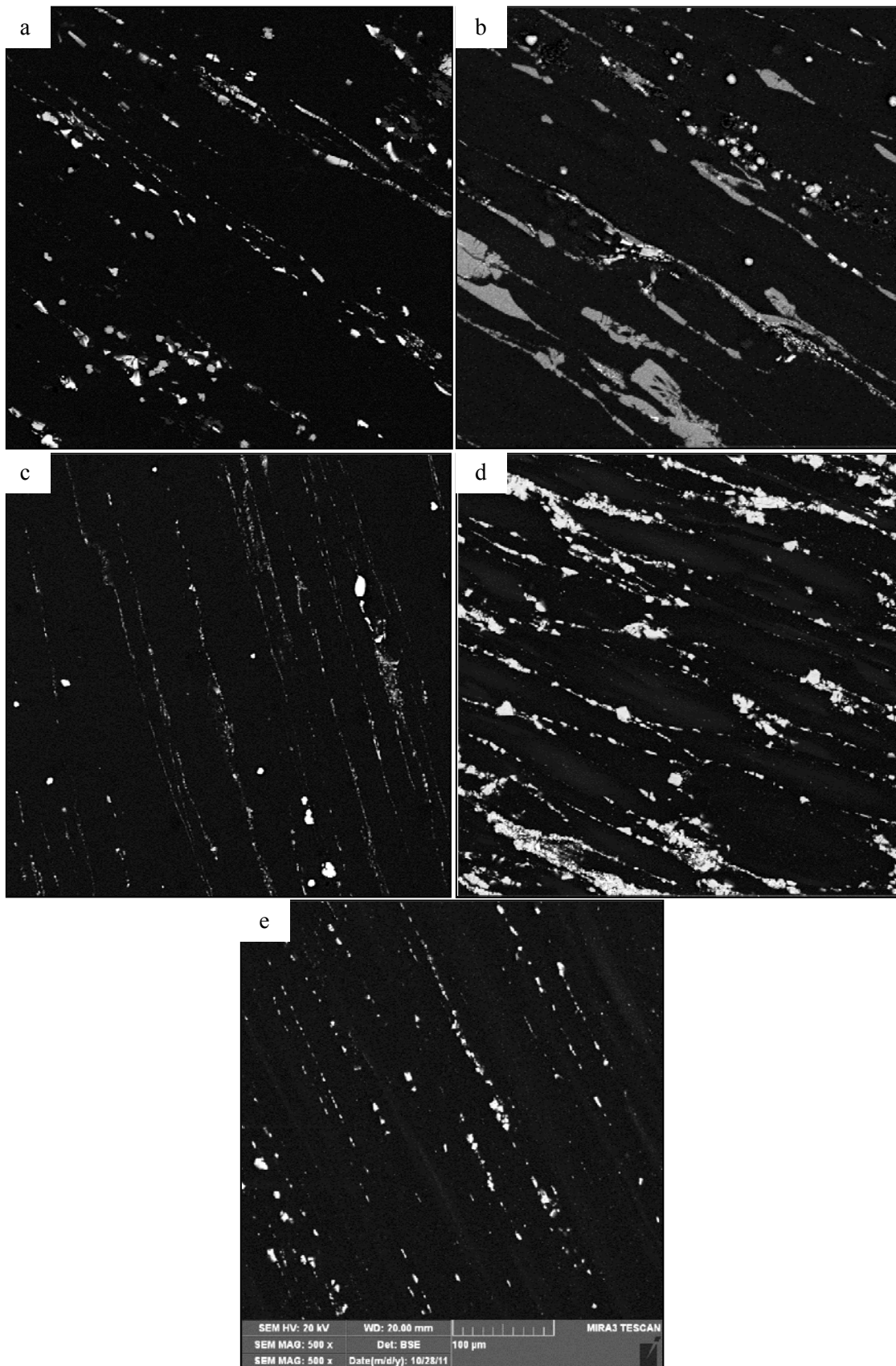


Figure 58. General microstructure of the: a) AE42 alloy, b) AJ32 alloy, c) AX30 alloy, d) EZ33 alloy and e) ZE10 alloy (500x magnification)

5.2.4.1 Intermetallics in the AE42 Alloy

The intermetallics in the as-extruded AE42 alloy are shown in Figure 59. Two main intermetallic compounds were found: cuboid Al_6Mn_3RE and acicular $Al_{11}RE_3$. The Al_6Mn_3RE intermetallic was on average 10 μm in length and appeared to be without fractures from extrusion. The $Al_{11}RE_3$ particles were on average 4 μm in length and likely fractured due to the extrusion process. The $Al_{11}RE_3$ particles formed along grain boundaries or in the immediate vicinity of the Al_6Mn_3RE particles. The Al_6Mn_3RE particles appeared predominantly along grain boundaries, yet were occasionally dispersed throughout the grains.

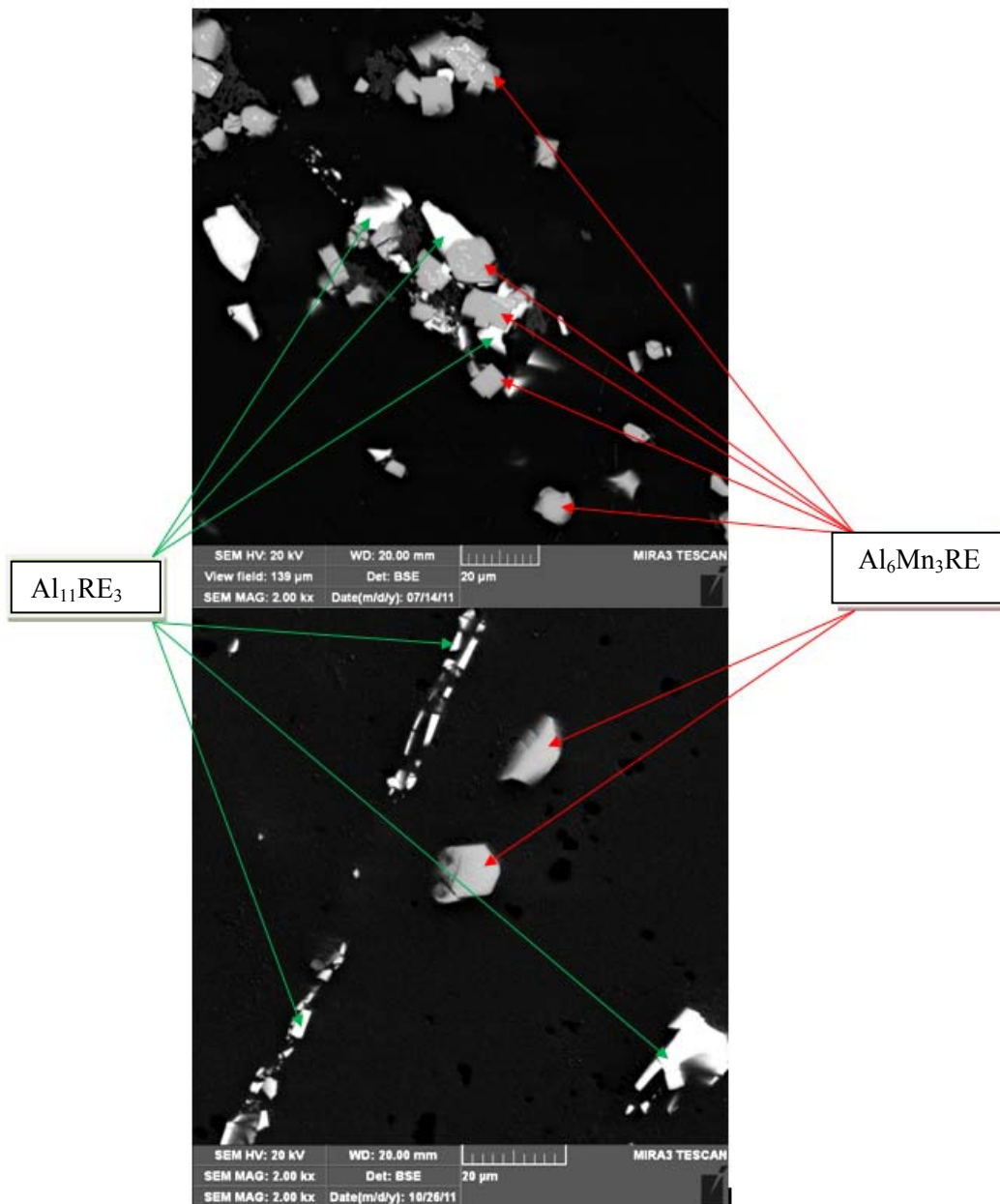


Figure 59. SEM micrographs of the intermetallics in the as-extruded AE42 alloy

The intermetallics in the post compressive-creep AE42 are shown in Figure 60. It was found that the Al_6Mn_3RE remained intact after creep testing, indicating its high thermal stability. This is in agreement with published data, suggesting that the presence of Mn increases alloy strength up to 290°C [4]. The $Al_{11}RE_3$ intermetallics, however, fractured in the post-creep condition and also started to decompose into $(Al_{11}RE_3)Mg_x$, as can be seen in Figure 60b. The $(Al_{11}RE_3)Mg_x$ particles showed significant fracturing due to the phase change. Previous experiments show that $Al_{11}RE_3$ decomposed above 150°C into Al_2RE , however Al_2RE particles were not found in this research due to insufficient time at elevated temperatures (only 23 hours). As a result, the observations in Figure 60 possibly capture the initial stage of the phase transformation.

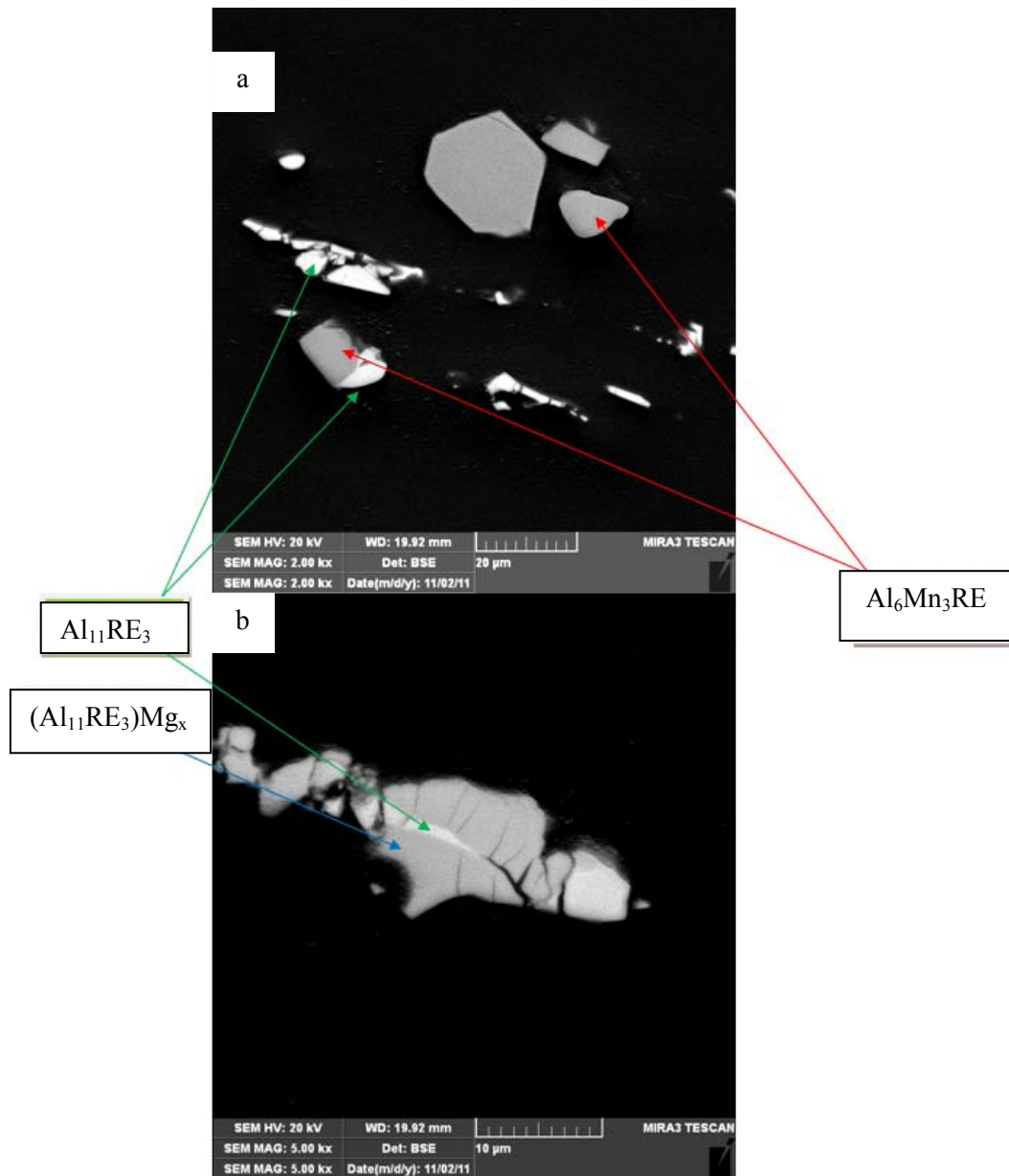


Figure 60. SEM micrographs of the intermetallics in the post-creep AE42 alloy

5.2.4.2 Intermetallics in the AJ32 Alloy

Five different intermetallics were found in the AJ32 alloy and are indicated in Figure 61. The largest intermetallic found was the Al_5Sr_3 , which was on average 28 μm in diameter and had minimal fractures perpendicular to the extrusion direction. Al_5Sr_3 had a unique structure, where pockets of Sr rich matrix were found embedded in the Al_5Sr_3 particles, as seen in Figure 62. These pockets formed within the larger Al_5Sr_3 particles and had an average diameter of 24 μm . Also, impurities of AlN were seen along the grain boundaries.

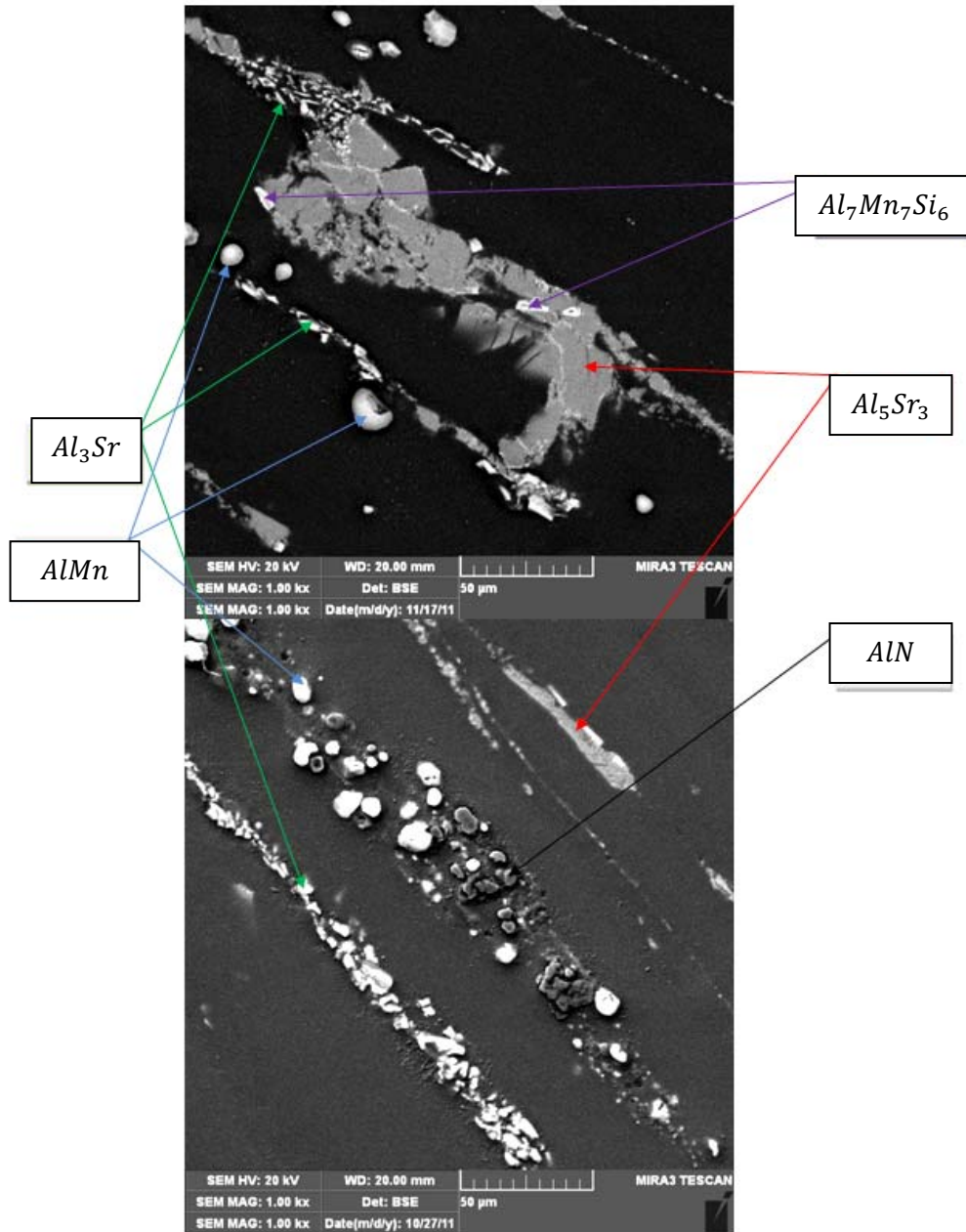


Figure 61. SEM micrographs of the intermetallics in the as-extruded AJ32 alloy

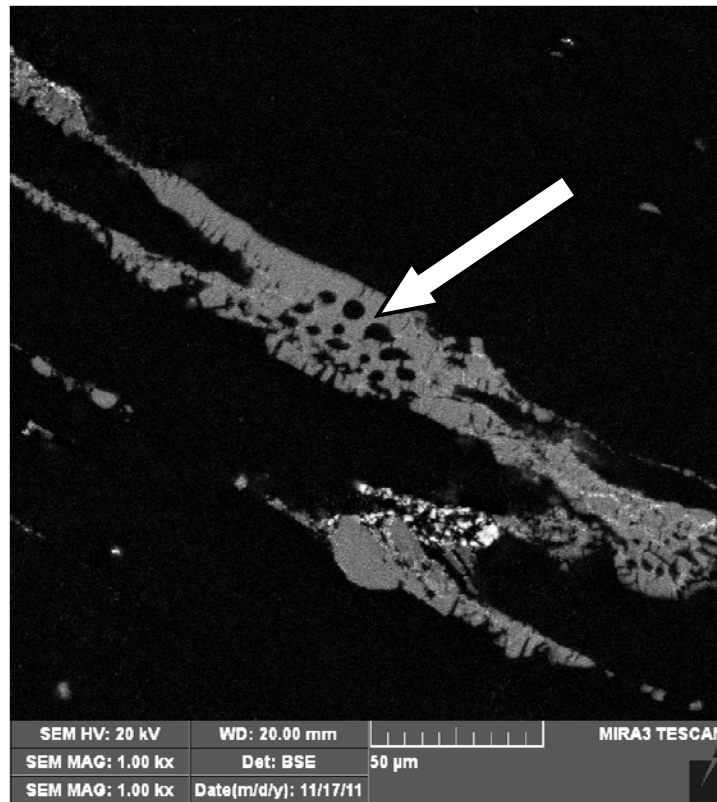


Figure 62. SEM micrograph of Al_5Sr_3 in the as-extruded AJ32 alloy

Severely fractured Al_3Sr particles were found in the AJ32 alloy which were approximately 18 μm in diameter and formed along grain boundaries, at times coating the Al_5Sr_3 phase with fine particles. In essence, the Al_3Sr created rough edges on the Al_5Sr_3 particles, thereby increasing its surface area. This increase of surface area would potentially have a significant impact on the Al_5Sr_3 's ability to pin grain boundaries.

$Al_7Mn_7Si_6$ intermetallic compound was also found to form around the Al_5Sr_3 particles. The $Al_7Mn_7Si_6$ particles were acicular, approximately 10 μm in diameter and often formed near the edge of Al_5Sr_3 particles, as seen in Figure 61.

Rounded $AlMn$ particles were also detected throughout the matrix and along the grain boundaries. These precipitates did not fracture.

Micrographs of the AJ32 intermetallics, post compressive-creep, are given in Figure 63. As seen in the figure, a significant fracturing of Al_5Sr_3 took place during creep. The severity of fractures increased in the direction perpendicular to the extrusion direction. Some fragments of the Al_5Sr_3 intermetallics separated, thus becoming separate particles, as seen in Figure 64.

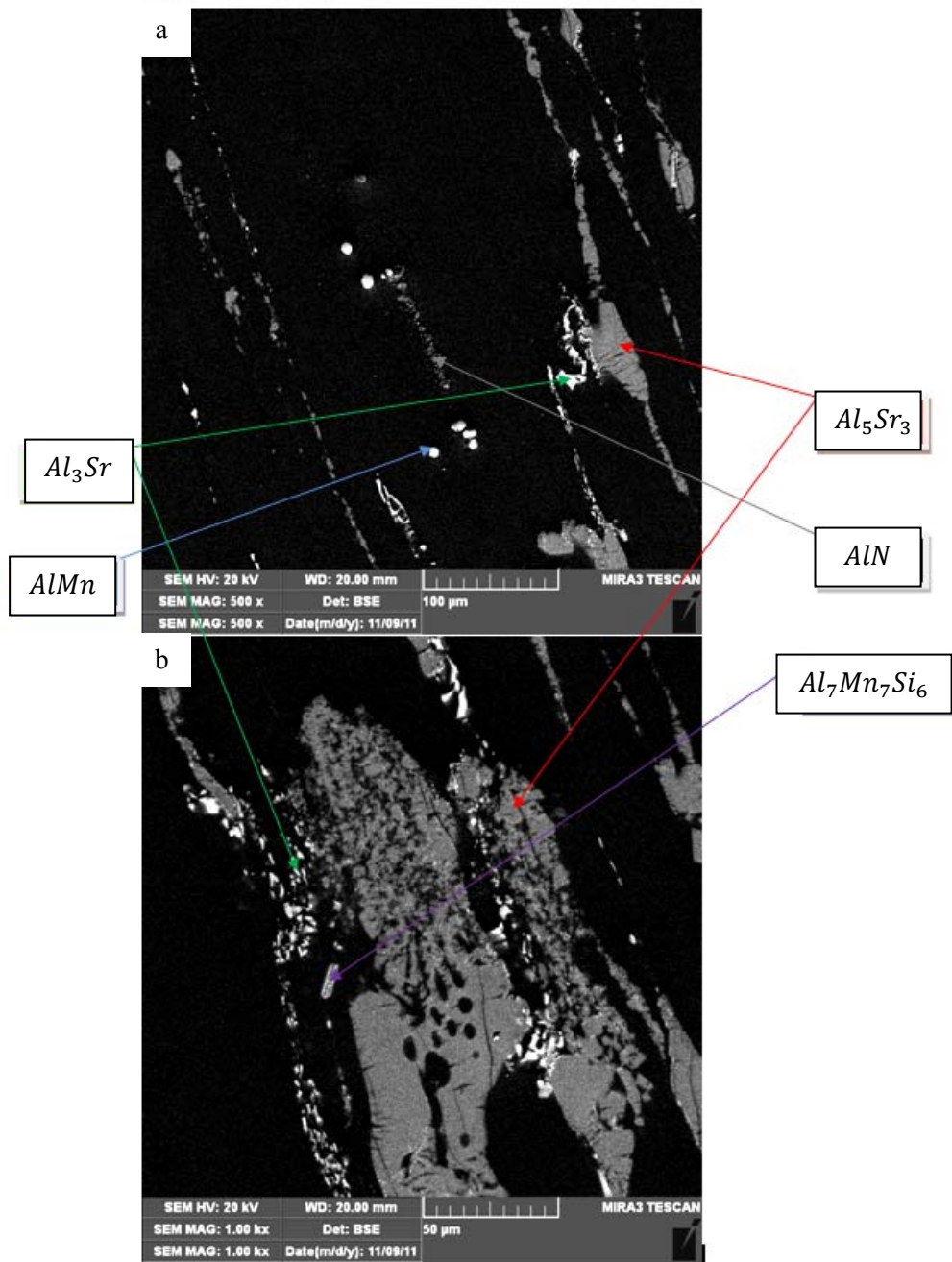


Figure 63. SEM micrographs of the intermetallics in the post-creep AJ32 alloy

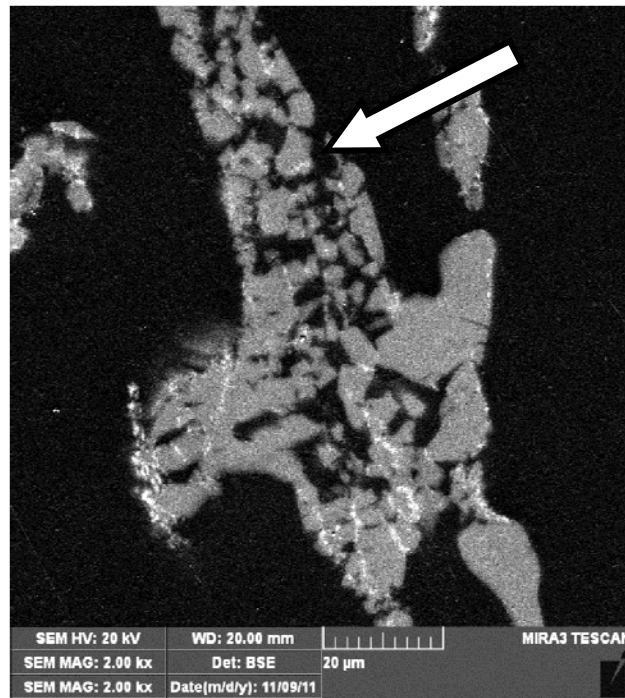


Figure 64. SEM micrograph showing fracturing of Al_5Sr_3 in the post-creep AJ32 alloy

No significant compositional change was found in the Al_3Sr , $Al_7Mn_7Si_6$, $AlMn$, or AlN particles between their as-extruded and post-creep conditions. This indicates a high thermal and mechanical stability of these particles. This coincides with the high creep resistance of AJ32, indicating that the thermally stable intermetallics were likely effective at pinning grains at temperatures as high as 175°C.

5.2.4.3 Comparison of Intermetallics in the AX30 Alloy to AE42 and AJ32 Alloys

As explained in the experimental procedure, a comprehensive analysis of the intermetallics in the AX30 alloy was not performed. However, micrographs were obtained to evaluate the general morphology of the intermetallics. As seen in Figure 65, the AX30 alloy contained acicular intermetallics mainly along the grain boundaries, similarly to both AE42 and AJ32. However, the intermetallics found in the AX30 alloy were significantly smaller than those observed in AE42 or AJ32 alloys. Continuously distributed small intermetallics are generally known to enhance creep resistance [52].

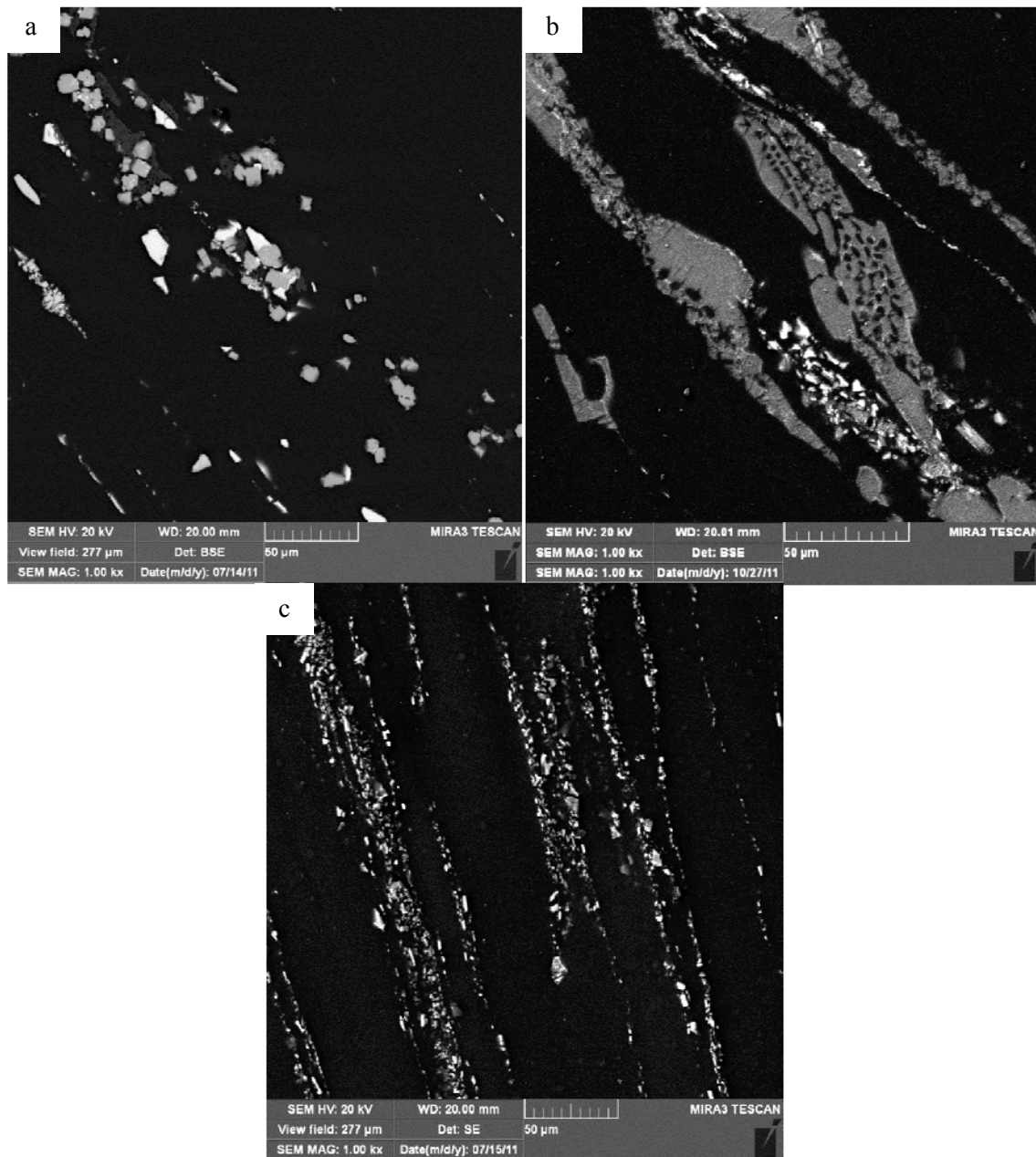


Figure 65. General microstructure of the as-extruded: a) AE42 alloy, b) AJ32 alloy and c) AX30 alloy

5.2.4.4 Intermetallics in the ZE10 Alloy

Figure 66 shows the three intermetallics found in the as-extruded ZE10 alloy. These intermetallics include cuboid $ZnRE$, clusters of nano Zr_3Si particles and nanoprecipitates of Zn_4RE . The $ZnRE$ intermetallics were the largest intermetallics in the ZE10 alloy and were on average 5 μm in diameter. $ZnRE$ was mainly distributed along the grain boundaries and appeared to have fractured and separated during the extrusion process.

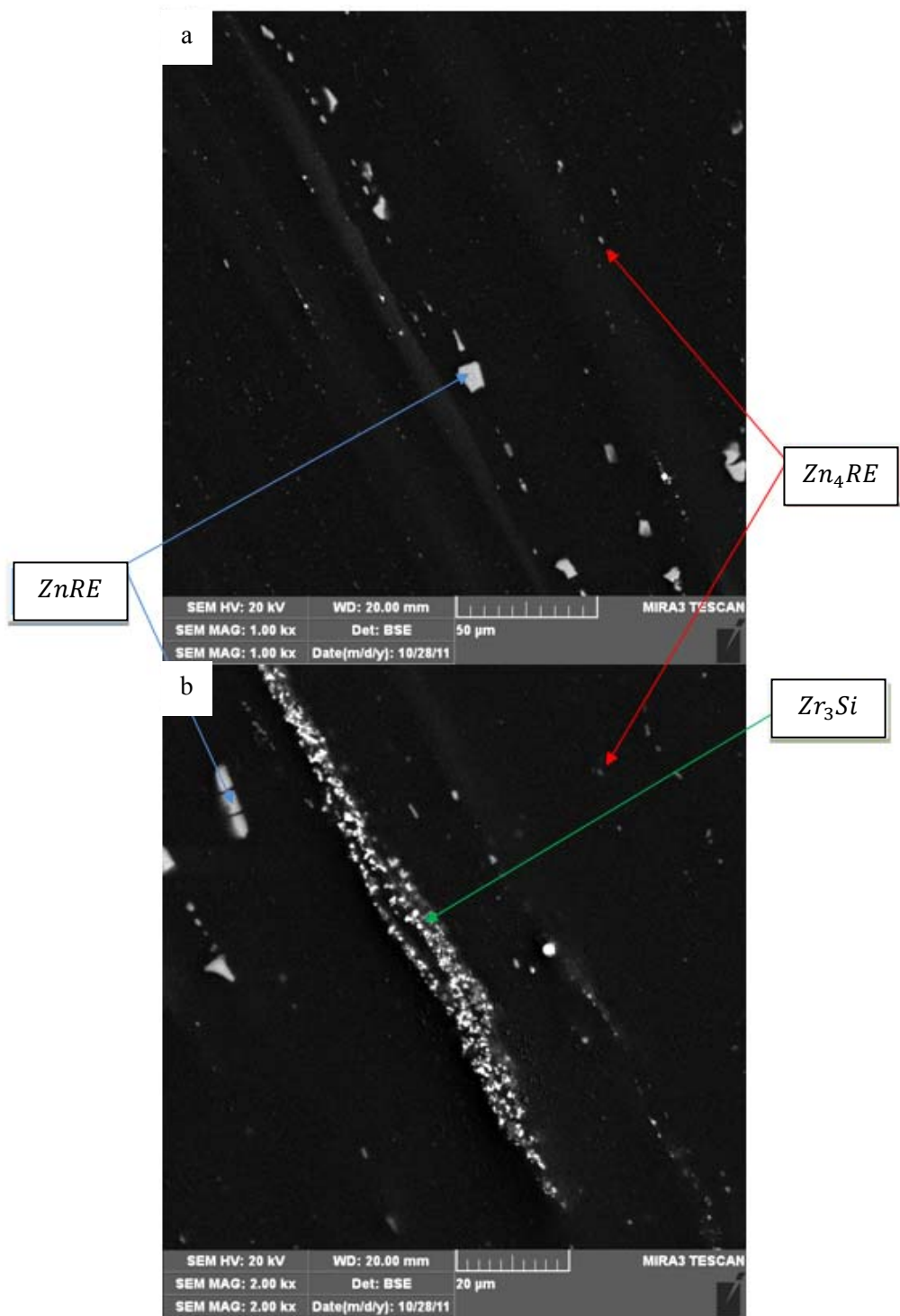


Figure 66. SEM micrographs of the intermetallics in the as-extruded ZE10 alloy

Large clusters of Zr_3Si particles were also found along the grain boundaries throughout the ZE10 alloy (Figure 67). These particles were approximately 0.6 μm in diameter and therefore considered to be nanoparticles, which are known to be effective at increasing alloy creep resistance [52]. Zn_4RE intermetallics were found in the ZE10 alloy and had an average diameter of 0.7 μm (Figure 68). The Zn_4RE particles were distributed throughout the matrix of the ZE10 alloy and at

times formed in strands along the extrusion direction. These particles may have fractured during the extrusion process, however further research must be done to determine how these particles formed.

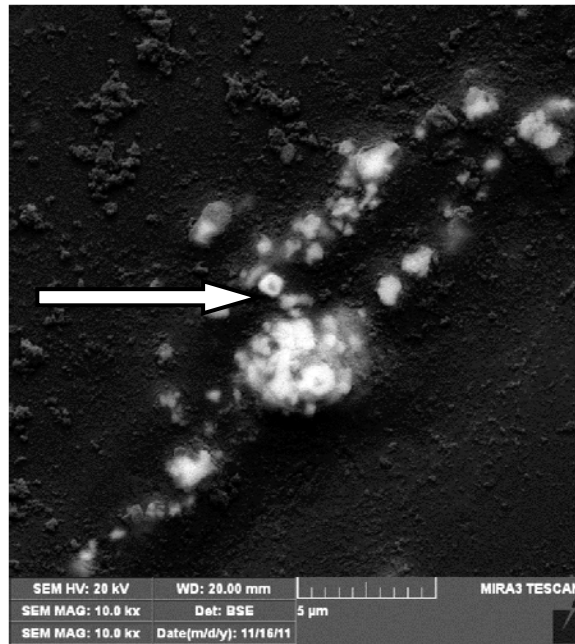


Figure 67. SEM micrograph of the Zr_3Si nanoprecipitate in the ZE10 alloy

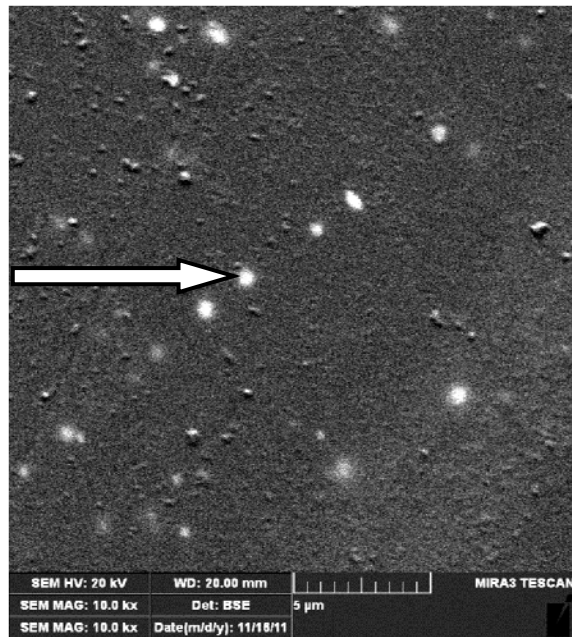


Figure 68. SEM micrograph of the Zn_4RE nanoprecipitate in the ZE10 alloy

The intermetallics observed in the post compressive-creep ZE10 alloy are shown in Figure 69, and were identified as $ZnRE$, Zn_4RE and Zr_3Si . Also, a new intermetallic compound $RE_5Zn_2Si_xZr_y$ was detected. The $ZnRE$, Zn_4RE and Zr_3Si particles did not change size, shape or

composition from their as-extruded to post-creep conditions, indicating their mechanical and thermal stability.

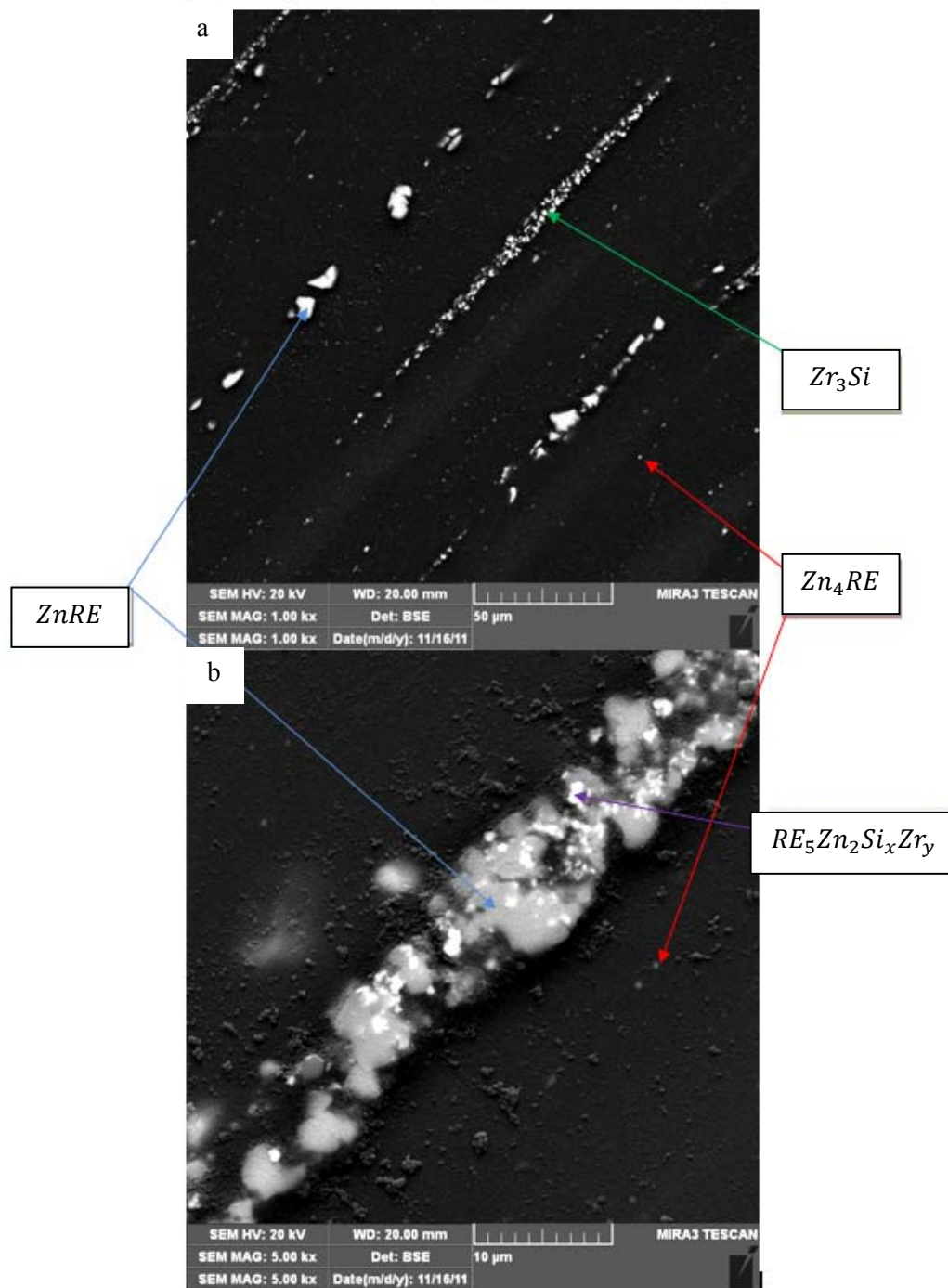


Figure 69. SEM micrographs of the intermetallics in the post-creep ZE10 alloy

5.2.4.5 Intermetallics in the EZ33 and ZE10 Alloys

Similarly to AX30, comprehensive XEDS analysis was not performed for the EZ33 alloy. However, SEM micrographs were obtained for the EZ33 alloy in the as-extruded state to provide a comparison of the general intermetallic morphology to those found in the ZE10 alloy. Micrographs of

the EZ33 and ZE10 alloys in their as-extruded conditions are presented in Figure 70. Although both the EZ33 and ZE10 alloys contain irregular intermetallics, the volume fraction of intermetallics in the EZ33 alloy is much greater than of those in the ZE10 alloy. Similarly to the ZE10 alloy, the EZ33 alloy also contained nanoparticles dispersed throughout the matrix. In the ZE10 alloy, there appeared to be no affinity of one intermetallic to another. The EZ33 alloy had complex particles, where multiple intermetallics formed in clusters, creating irregular particles with serrated edges. These complex intermetallics likely contributed to the high creep resistance of the EZ33 alloy.

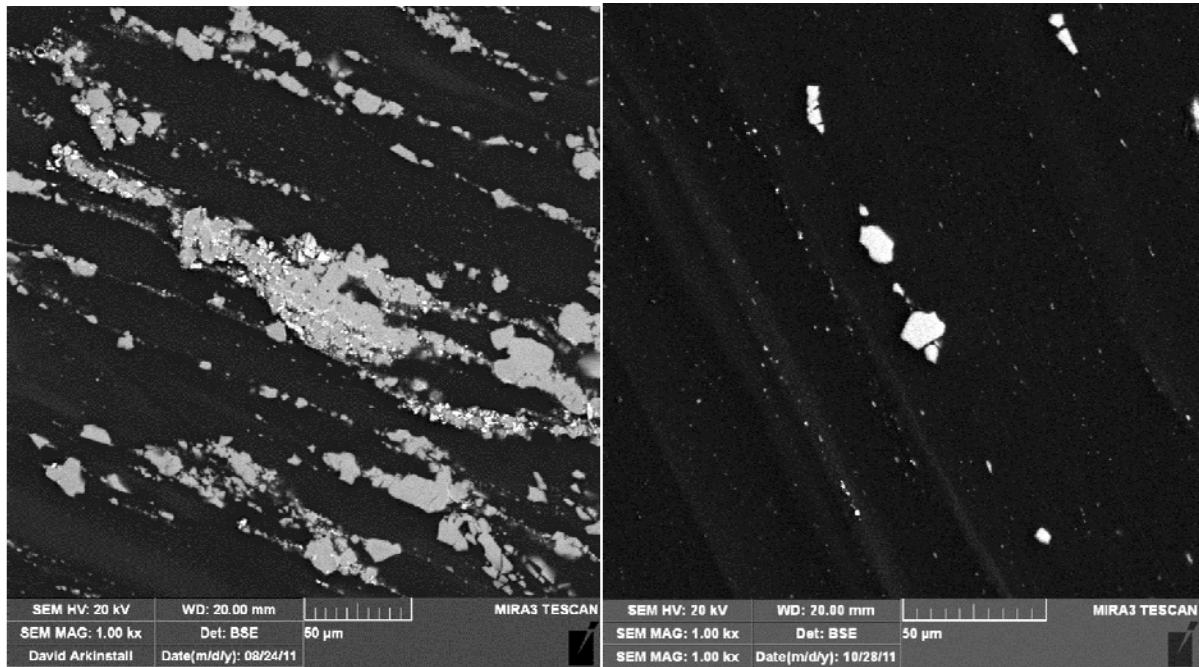


Figure 70. General microstructure of the as-extruded: a) EZ33 alloy and b) ZE10 alloy

Optical microscopic analysis also revealed that particles in the EZ33 alloy oriented in curved bands, thus suggesting matrix flow within the grains (Figure 71). These flow bands were present in both the as-extruded and post-creep EZ33 alloy and show that the material within the grains moved, while the grain boundaries remained stationary. This was possibly an indication of grain boundaries being stronger than the matrix, causing deformation to be accommodated by the matrix and not by grain boundary sliding. Further analysis must be done to analyze whether the flow bands observed in the post-creep EZ33 alloy were due to material deformation during creep testing, or if they were created during the prior extrusion process.

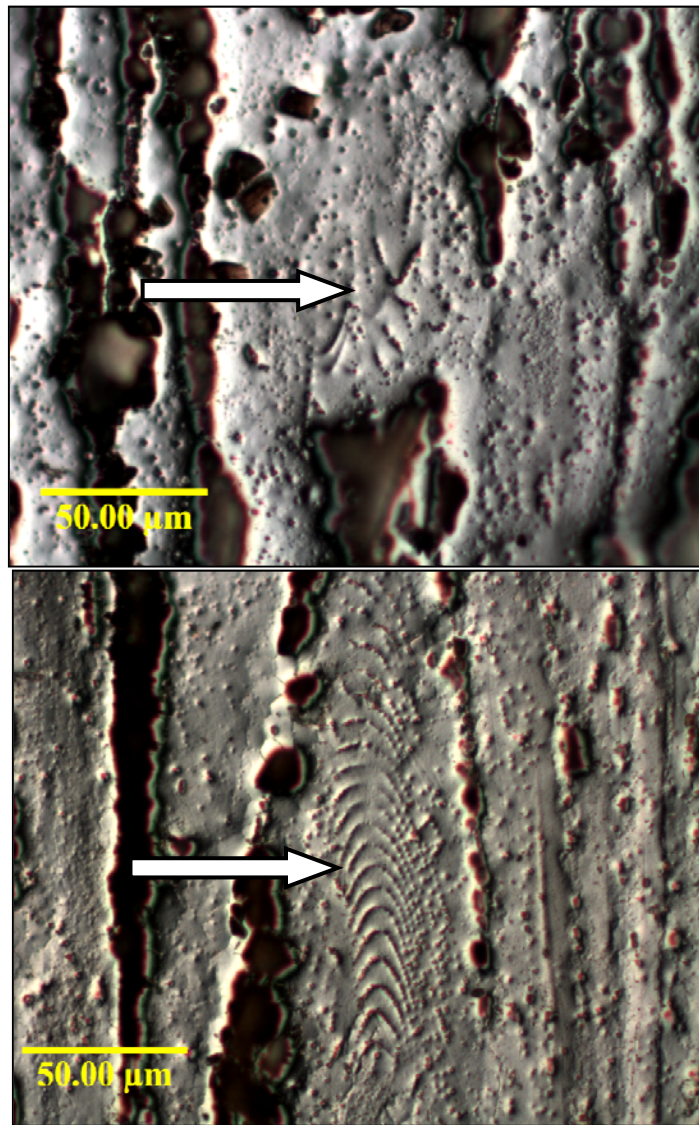


Figure 71. Nanoprecipitate flow bands in the: a) As-extruded and b) Post-creep EZ33 alloy

5.2.5 Al Segregation Analysis Using SEM and Optical Microscopy

Solute segregation was found in the AE42, AJ32 and ZE10 alloys in both their as-extruded and post-creep states. In the AE42 and AJ32 alloys, Al was found to segregate along the grain boundaries and within the grains. In the ZE10 alloy both Zn and Zr segregated within the grains.

5.2.5.1 Segregation of Al in the AE42 Alloy

Elemental mapping was performed using XEDS analysis, as seen in Figure 72. As seen in the element maps, the RE and Mn elements were associated with the intermetallic particles. Al was also found in the intermetallic particles, but also as distinct bands in the grains. Therefore, as expected, the RE elements are believed to have bound the majority of Al in the alloy, but some Al was still available in the matrix for the formation of the undesirable β -phase.

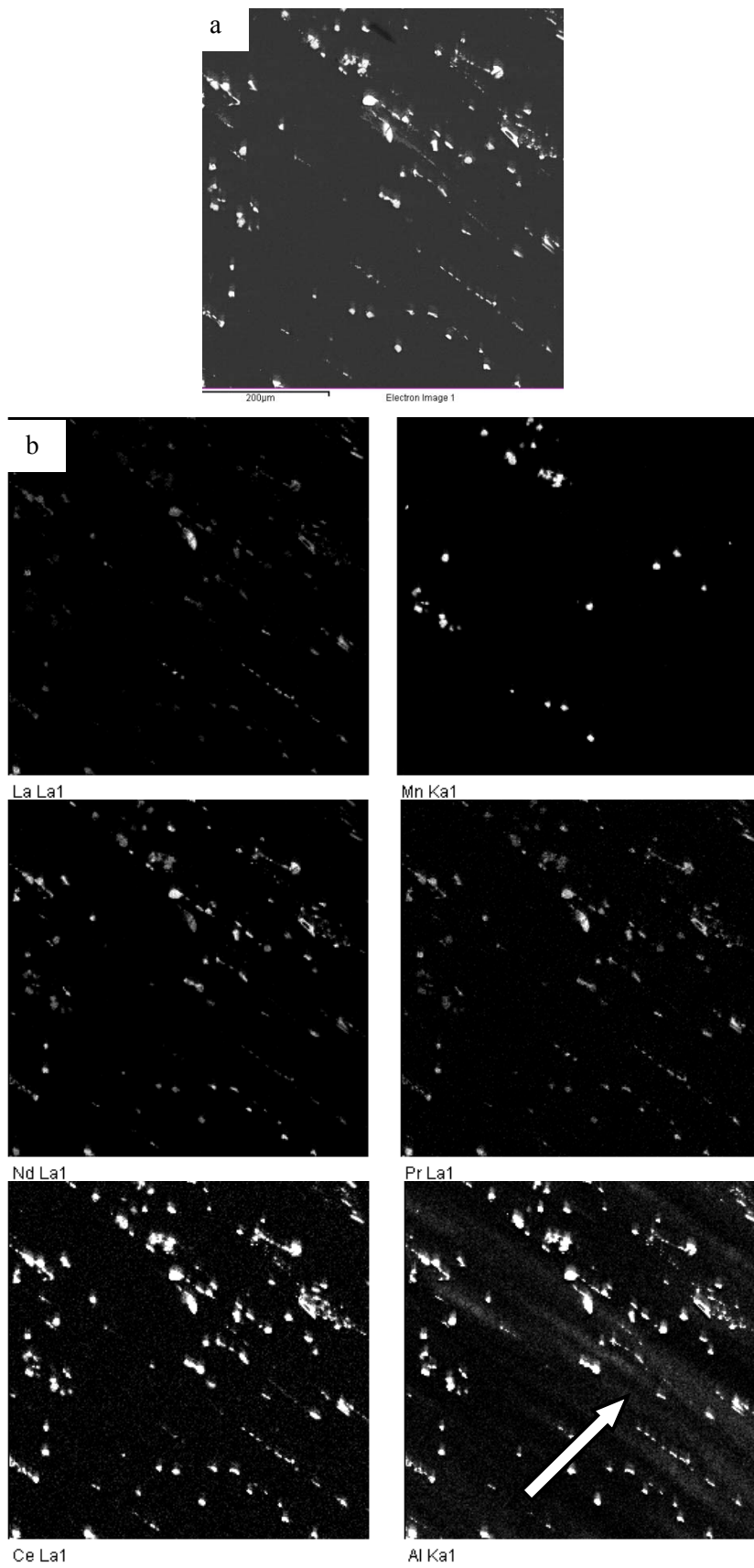


Figure 72. XEDS maps of as-extruded AE42 alloy: a) SEM micrograph and b) Elemental maps

As can be seen in the Al element map in Figure 72, the Al segregation in the AE42 alloy took the form of supersaturated Al banding, rather than islands of Al. Supersaturated Al bands coincided with fibrous β -phase, as verified using optical microscopy (Figure 73).

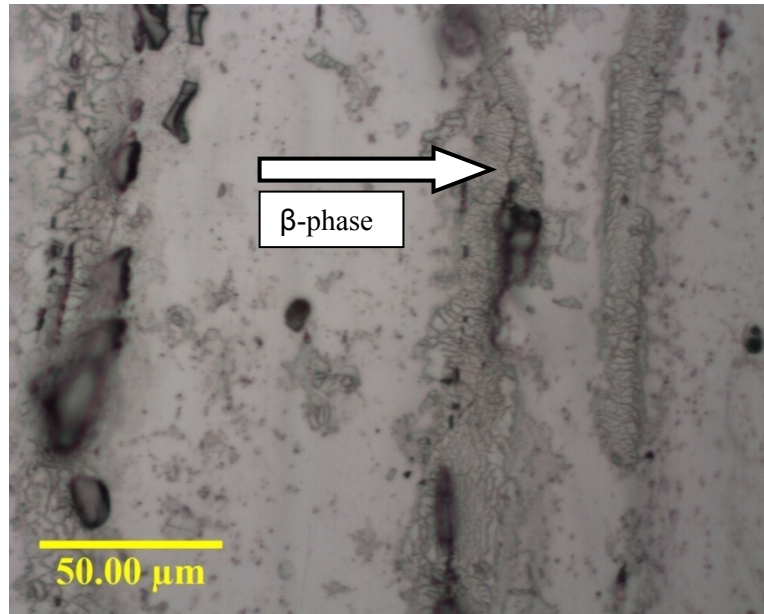


Figure 73. Fibrous β -phase in the as-extruded AE42 alloy

Further XEDS analysis was performed on the Al bands and changes in Al concentration were studied, as seen in Figure 74. A linescan was performed across a grain, in the absence of intermetallics. As can be seen in the plot, the Al concentration increased, while the amount of REs remained at zero. The composition of Mg decreased, before gradually returning to the average matrix composition.

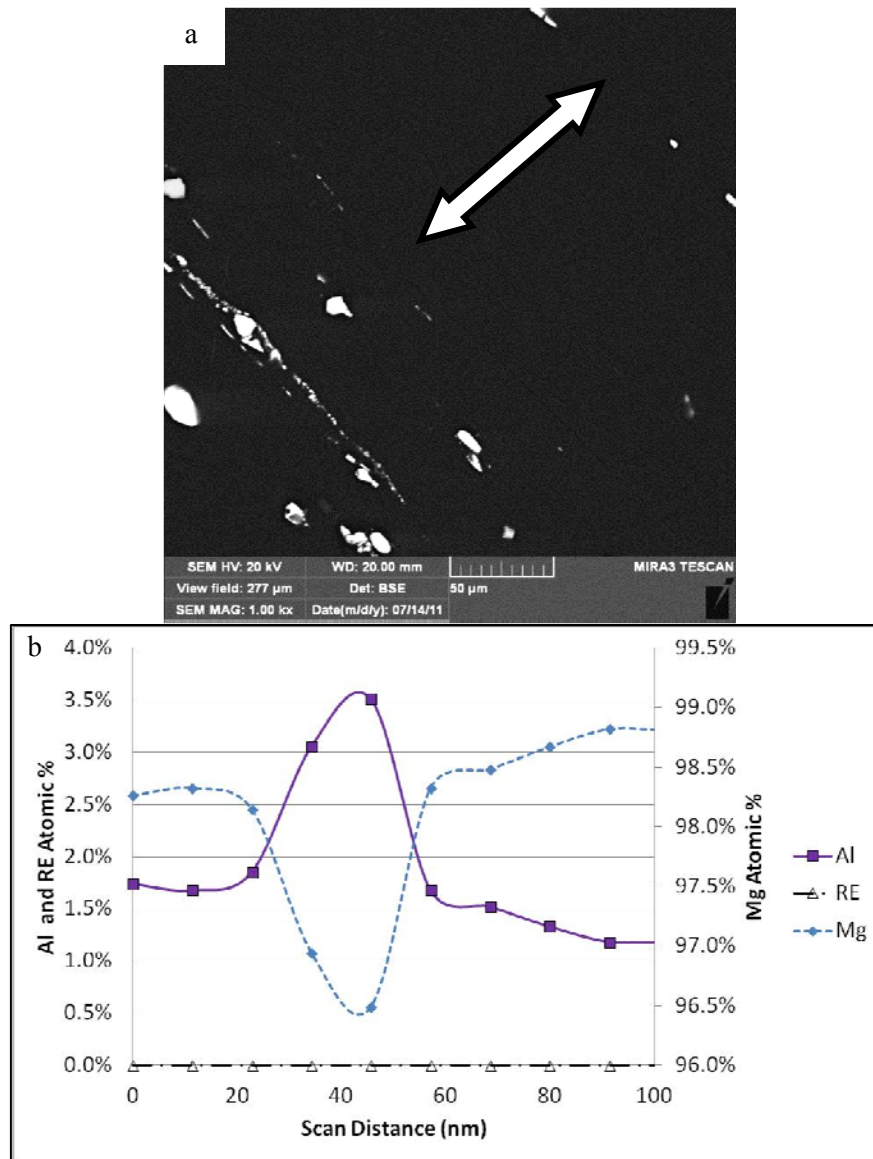


Figure 74. Al segregation in the as-extruded AE42 alloy showing the: a) Location of the linescan and b) Atomic composition along the linescan

The average peak value of Al banding in the as-extruded AE42 alloy was measured to be 3.1 At %, whereas the matrix contained 1.6 At%. Thus, the peak Al concentration was twice as large as that found in the matrix, indicating that the regions of Al bands were significantly different from the matrix material. The average width of the Al bands in the material was measured to be 34 μm.

Al banding was also found in the post compressive-creep AE42 alloy. The XEDS elemental mapping is provided in Figure 75. In the AE42 post-creep alloy, the Mn and RE elements remained tied in the intermetallics; however, the Al was found in the intermetallics as well as dispersed throughout the matrix. The Al concentration in the matrix was significantly higher than that seen in the as-extruded conditions (Figure 72), indicating an increase in Al mobility at elevated temperatures.

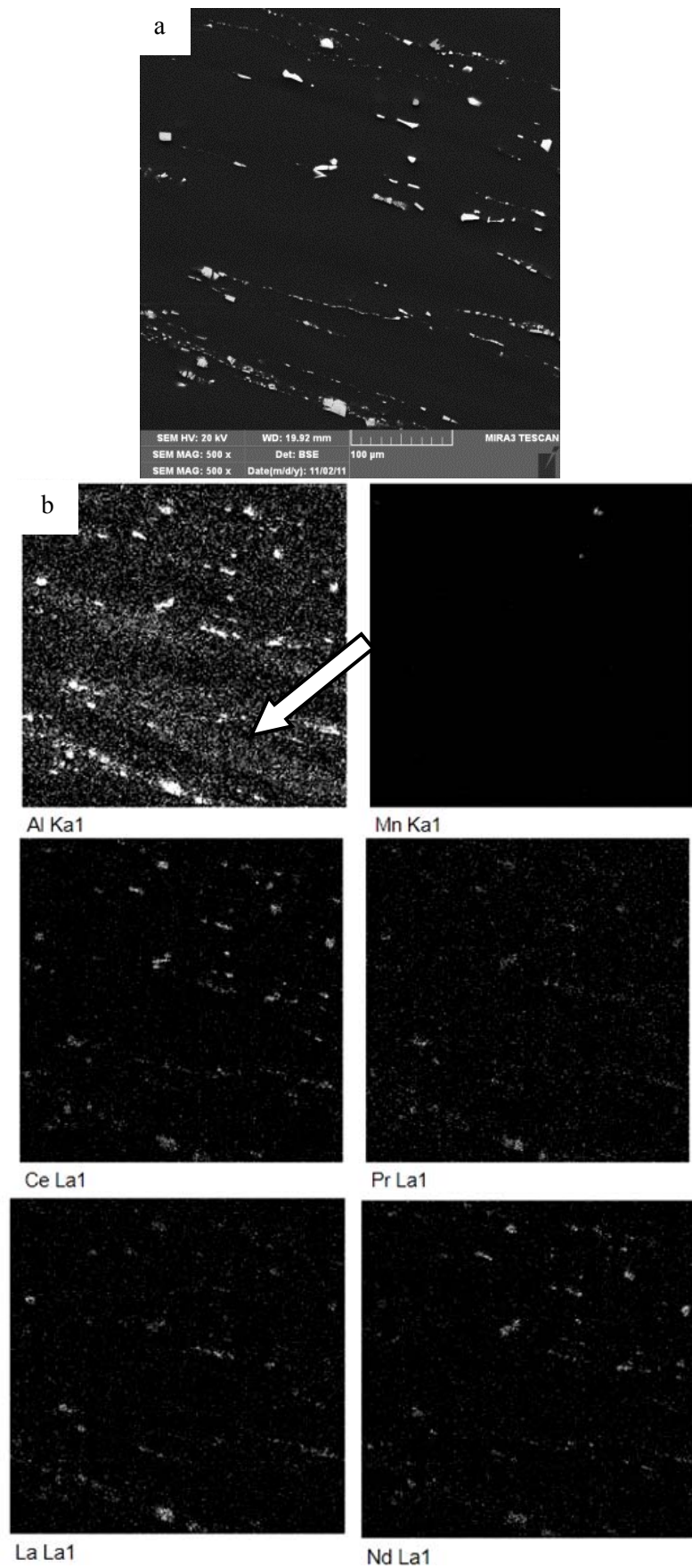


Figure 75. XEDS maps of post-creep AE42 alloy: a) SEM micrograph and b) Elemental maps

The Al segregation in the post-creep alloy took the form of a gradual increase in Al concentration throughout the matrix and possibly enabled the formation of fibrous, rather than lamellar, β -phase. Optical microscopy was again performed to verify the structure of the β -phase (Figure 76). It was observed that the low density fibrous β -phase, also found in the as-extruded microstructure, was still present in the post-creep microstructure (indicated with “A” in the micrograph); however, a high density fibrous β -phase was now readily apparent (indicated with “B” in the micrograph). The formation of the high density fibrous β -phase resulted from the supersaturation of Al in the matrix. This high density β -phase was found along grain and subgrain boundaries as well as surrounding intermetallics, possibly suggesting the instability of these intermetallics at elevated temperatures (which allowed the Al to be released into the matrix).

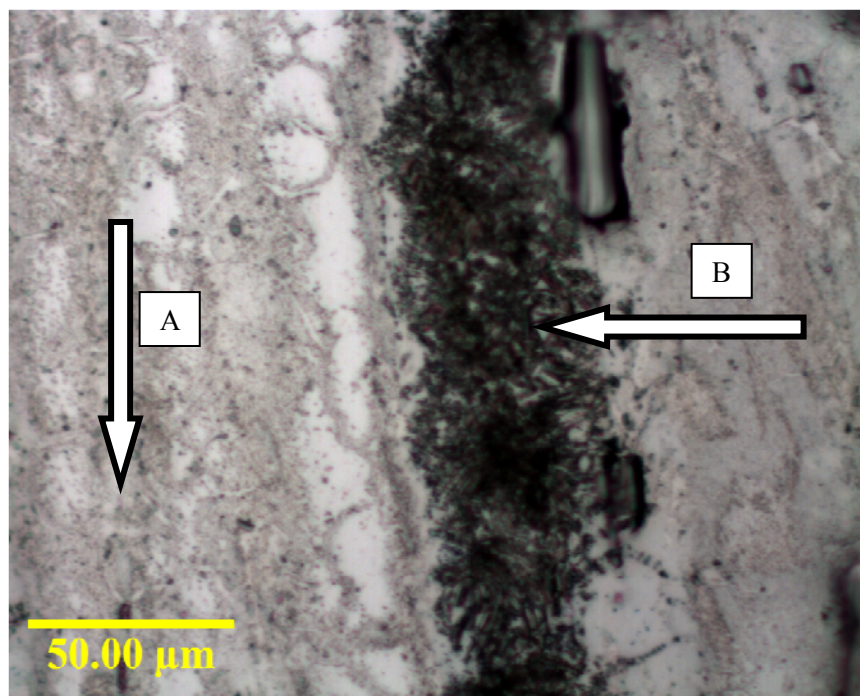


Figure 76. Fibrous β -phase in the post-creep AE42 alloy

Linescans were performed across the grains to gain quantitative information about the Al concentration in the matrix. An example of one of these linescans is given in Figure 77. The Al was seen to strongly peak at the grain boundary with an average peak value of 3.5 At% , while the matrix background contained 1.5 At%. The width of the Al band was 38 μm . The peak width was on the same order of the grain width.

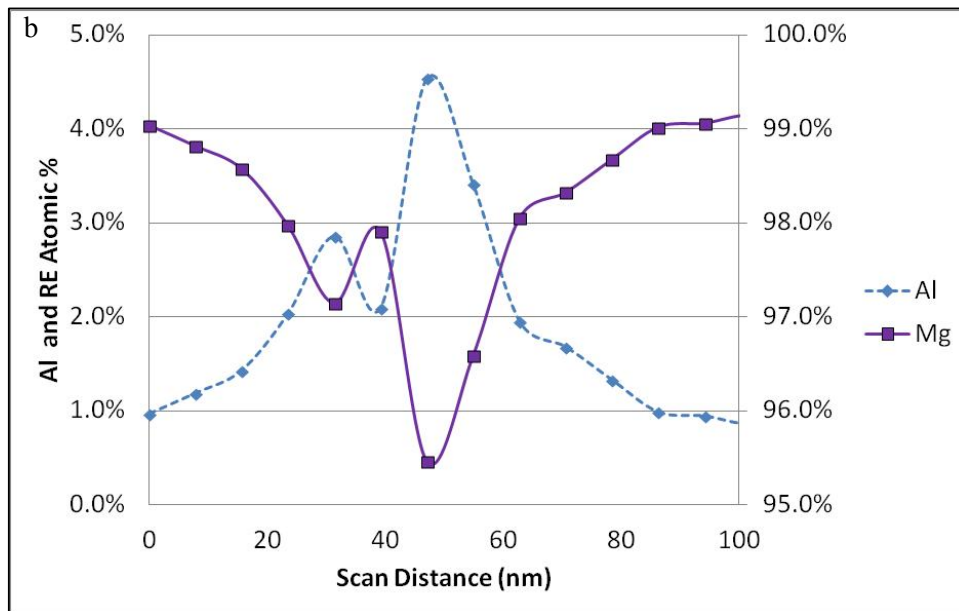
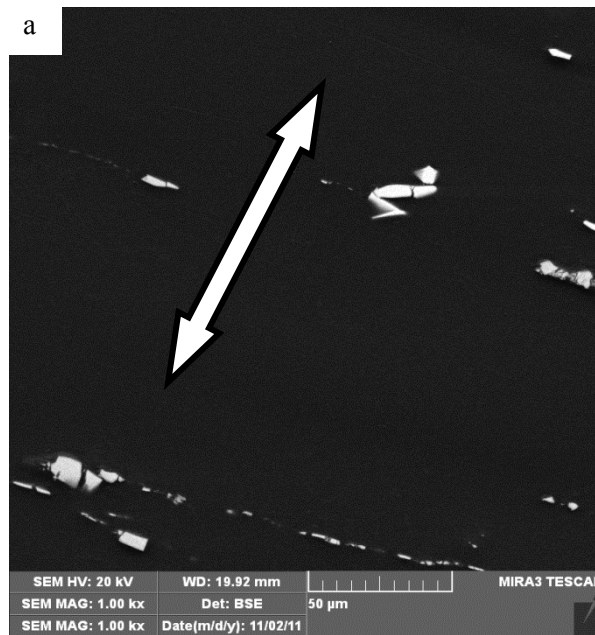


Figure 77. Al segregation in post-creep AE42 alloy showing the: a) Location of the linescan and b) Atomic composition

A comparison of the peak:background (i.e., peak:matrix) concentrations of Al in the as-extruded and post-creep AE42 samples is given in Figure 78, along with a comparison of the widths of the Al bands. The error bars in the figure indicate the standard deviation. The peak Al concentration in the post-creep alloy was approximately 13% greater than that of the as-extruded alloy, showing that Al was mobile at elevated temperatures. The average Al band width increased from 34 to 38 μm , from the as-extruded to post-creep condition. Therefore, more Al was found in the Al bands after creep testing and the bands increased in width.

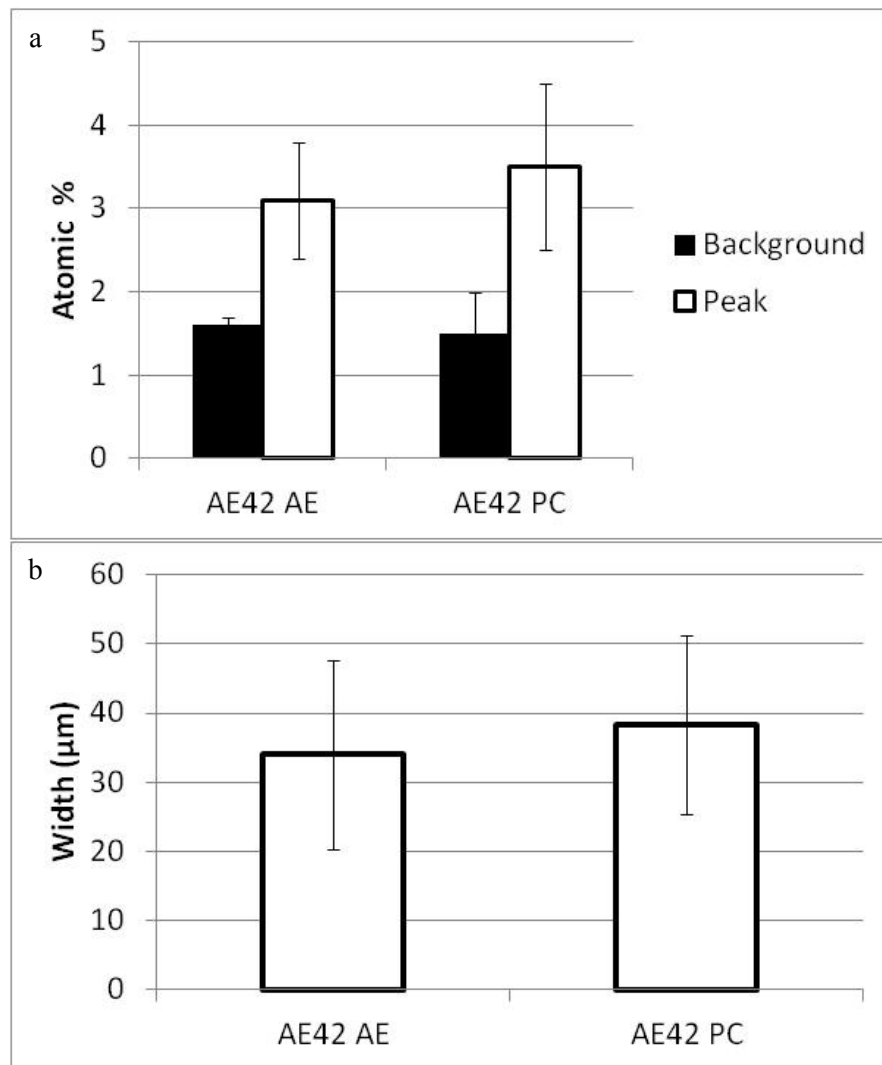


Figure 78. Comparison of the Al segregation in the as-extruded and post-creep AE42 alloy showing the: a) Peak:background ratio and b) Al band width

Statistical analysis was performed on the data gained from the Al concentration measurements, which showed that in both (i.e., the as-extruded and post-creep) conditions Al concentrations at the peak were significantly higher than those of the matrix at a 95% confidence interval. However, due to the low number of tests, at a 95% confidence interval no significant concentration changes between the as-extruded and post-creep AE42 alloy conditions were determined. Therefore, further analysis is necessary to accurately quantify the changes in Al concentration before and after creep testing.

5.2.5.2 Segregation of Al in the AJ32 Alloy

Unlike in the AE42 alloy, Al was not seen to segregate and band in the AJ32 alloy (Figure 79). Instead Al, Mn and Fe were found to be located mainly in intermetallic compounds. Point scans were used to detect Sr in intermetallic compounds, due to the weak signal of Sr in the XEDS maps.

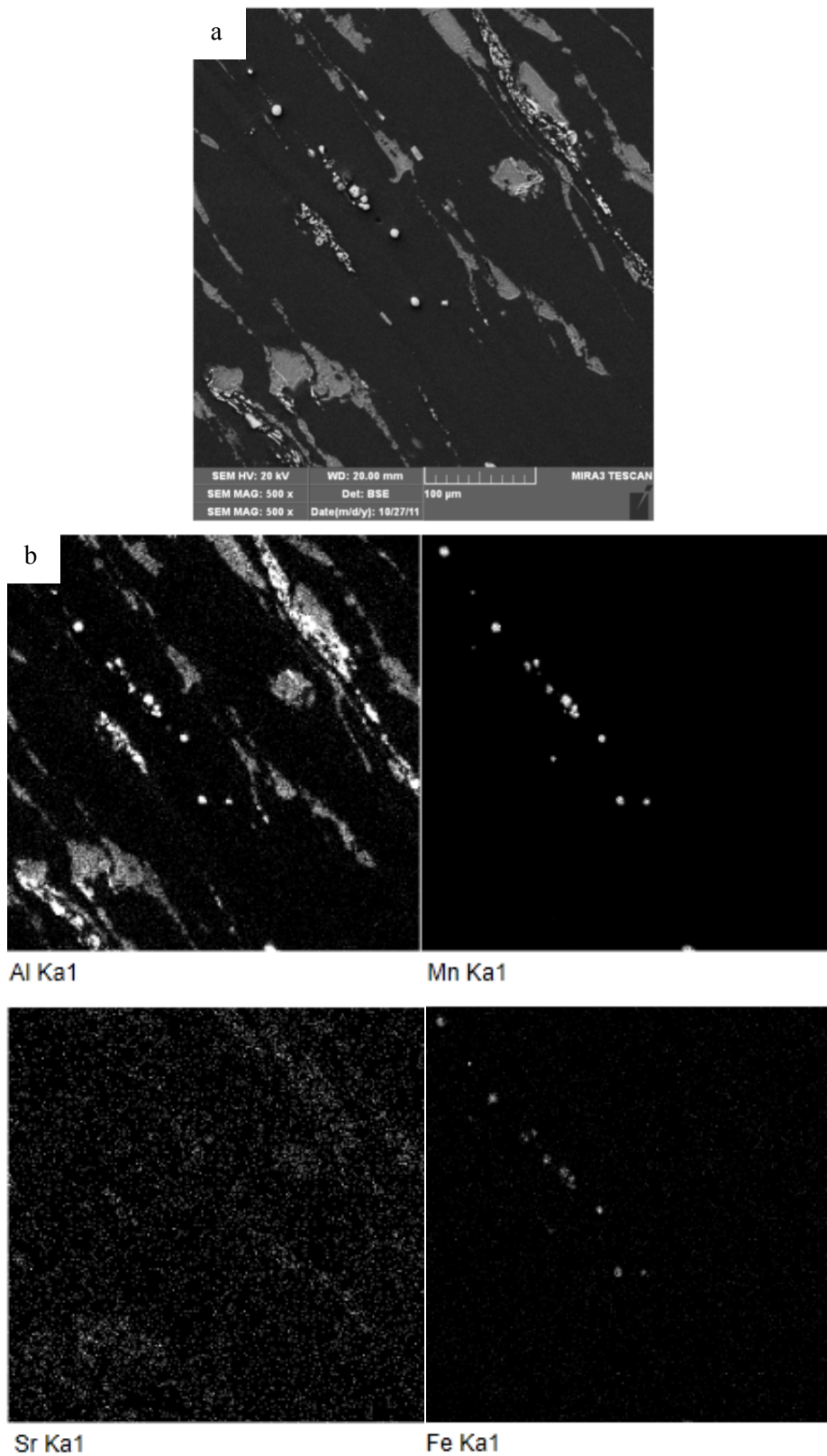


Figure 79. XEDS maps of as-extruded AJ32 alloy: a) SEM micrograph and b) Elemental maps

Although Al was not seen to band distinctly in the XEDS element maps, linescans were performed across the grain boundaries to quantify the Al concentration in these regions. An example

of a linescan is given in Figure 80, where it can be seen that the Al concentration increased at the grain boundaries. The average peak value for Al concentration at the grain boundary was calculated to be 1.2 At%, while it was 0.8 At% in the matrix. Therefore, Al was pushed towards the grain boundaries, rather than banding in the grains of the AJ32 alloy.

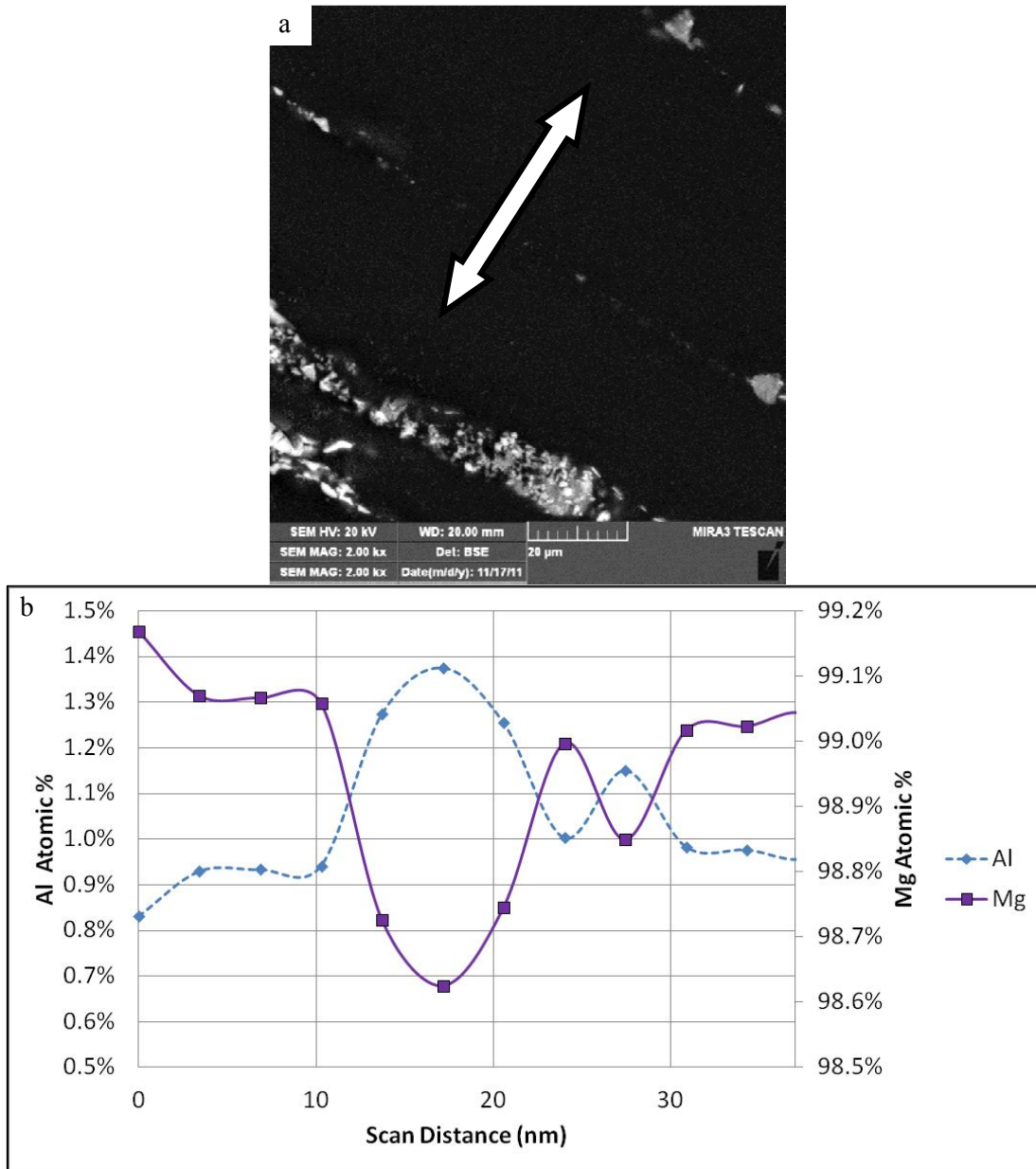


Figure 80. Al segregation in as-extruded AJ32 alloy showing the: a) Location of the linescan and b) Atomic composition

Optical microscopy was performed to study if the Al segregation in the AJ32 alloy resulted in the formation of the β -phase. A representative optical micrograph is provided in Figure 81. No β -phase was found in the as-extruded AJ32 alloy. Therefore, the intermetallics which formed in the AJ32 alloy were likely much more effective at binding Al.

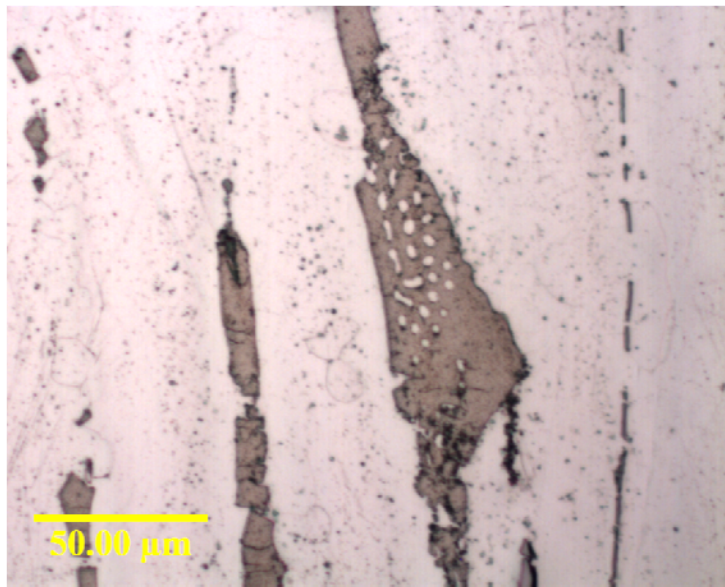


Figure 81. Absence of β -phase in the as-extruded AJ32 alloy

XEDS element mapping was also performed on the AJ32 alloy post-creep (Figure 82). The resulting element maps showed significantly more Al in the matrix, compared to the as-extruded AJ32 alloy. This increase in Al segregation indicated that Al was mobile during compressive creep testing, and possibly dissolved from the intermetallics into the matrix.

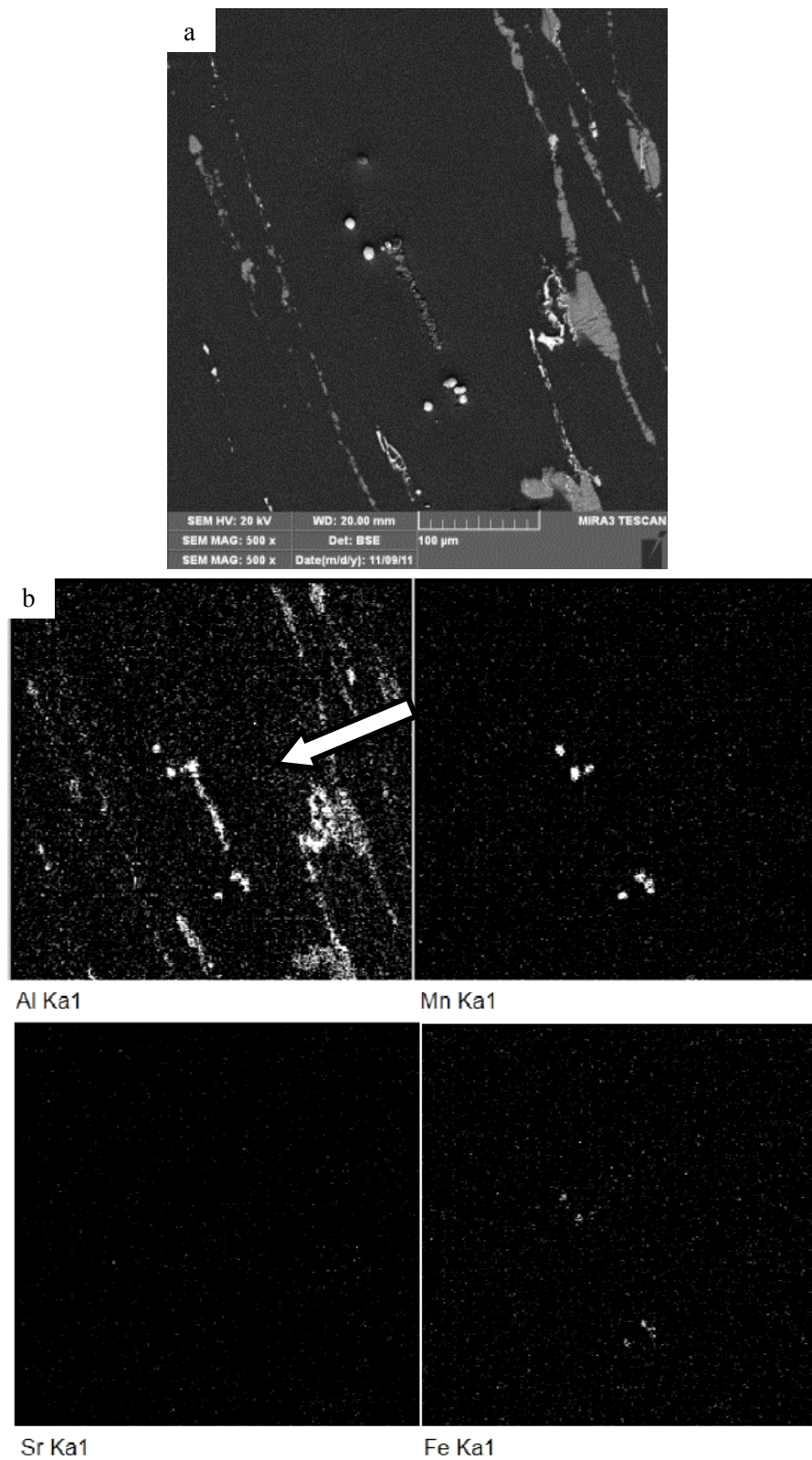


Figure 82. Post-creep AJ32 alloy: a) SEM micrograph and b) Elemental maps

Optical microscopy was performed on the post-creep AJ32 to determine whether or not this increase in Al concentration throughout the matrix resulted in β -phase formation. A representative

micrograph of the post-creep AJ32 alloy can be seen in Figure 83. Indeed, the fibrous β -phase was found surrounding intermetallics along the grain boundary. The β -phase was also observed to form primarily around the Al_3Sr intermetallic particles and was absent around the Al_5Sr_3 intermetallics. Thus, the Al_3Sr possibly released Al into the matrix during compressive creep testing at 175°C, which allowed for subsequent β -phase formation.

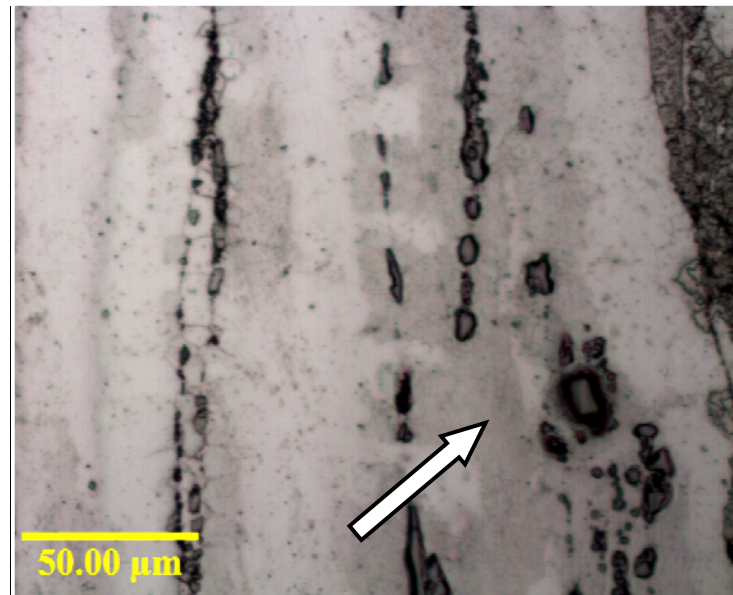


Figure 83. Fibrous β -phase in the post-creep AJ32 alloy

Linescans were also performed in the post-creep AJ32 alloy to quantify the Al concentration in the matrix. An example linescan can be seen in Figure 84. The peak Al concentration was measured to be 2.1 At% compared to 1.1 At% Al concentration of the matrix. A comparison of the peak:background (or peak:matrix) for the as-extruded and post-creep AJ32 alloy is shown in Figure 85, with error bars indicating the standard deviation. As can be observed from this figure, the post-creep AJ32 alloy had a significantly higher concentration of Al in the peak and a wider band width than the as-extruded alloy.

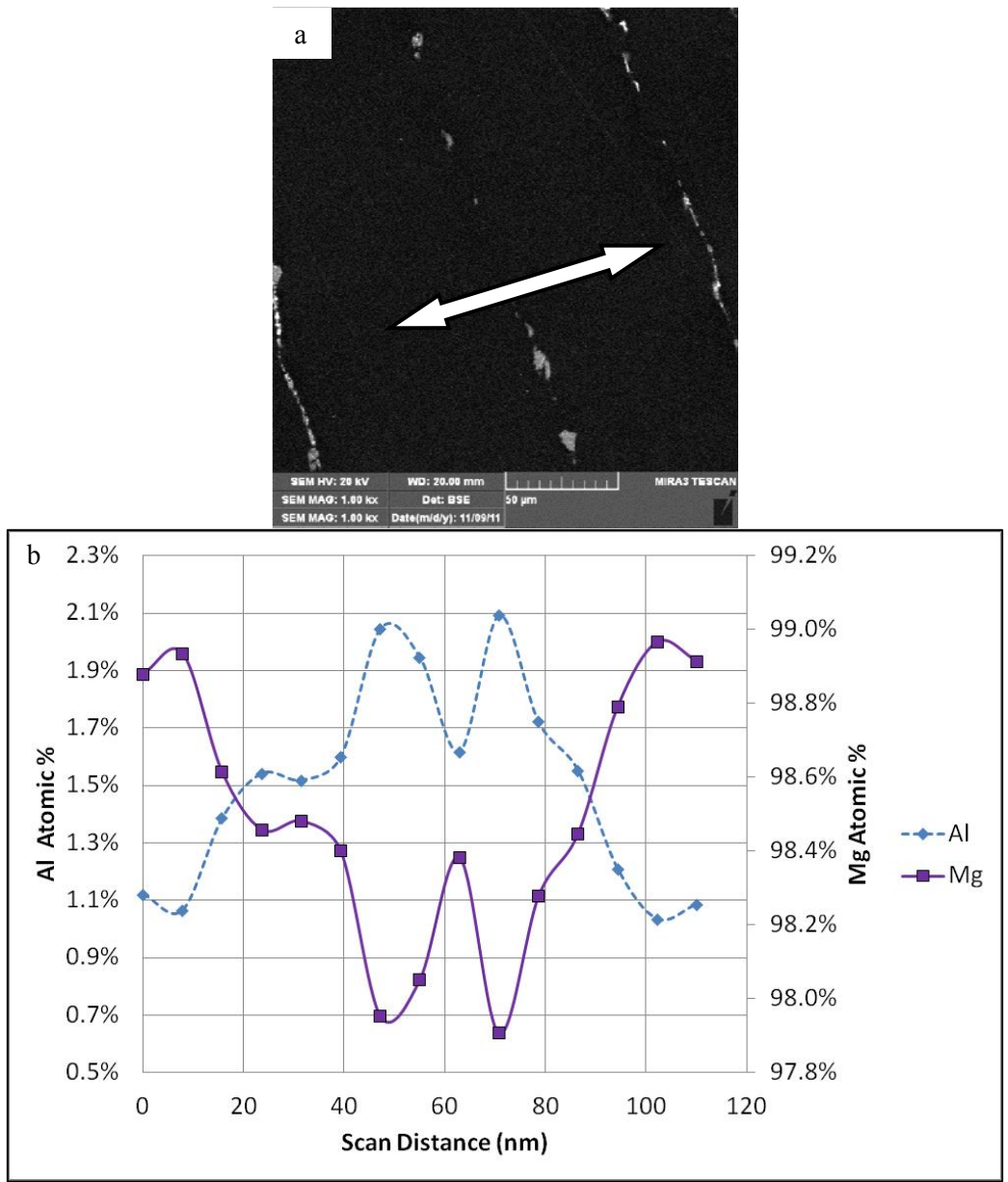


Figure 84. Al segregation in post-creep AJ32 alloy showing the: a) Location of the linescan and b) Atomic composition

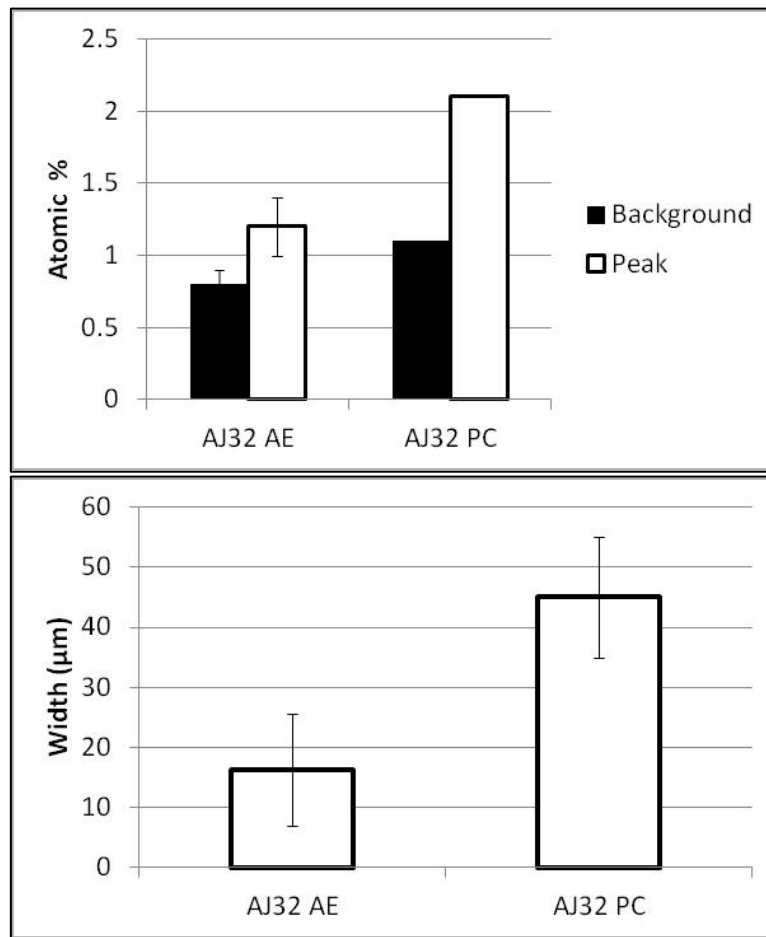


Figure 85. Comparison of the Al segregation in the as-extruded and post-creep AJ32 alloy showing the: a) Peak:background ratio and b) Al band width

Statistical analysis was performed on the data gained from the Al segregation measurements, which showed that in both the as-extruded and post-creep conditions, Al concentrations at the peak were significantly larger than those of the matrix at a 95% confidence interval. Statistical analysis also concluded that at a 95% confidence level the peak value of Al concentration and the width of the Al band increased from the as-extruded to post-creep conditions.

5.2.5.3 Comparison of Al Segregation in AE42 and AJ32 Alloys

Al was found to segregate in both the AE42 and AJ32 alloys. A plot of the peak and background atomic percents of Al in these alloys in their as-extruded and post-creep conditions is given in Figure 86, with error bars indicating the standard deviation. From this figure it can be seen that the peak Al concentration in the AE42 matrix is above that of the AJ32 alloy, indicating that the addition of Sr to the AJ32 alloy was more effective in binding the Al in the matrix than the RE addition into the AE42 alloy. Also, the amount of Al in the matrix was lower in the AJ32 alloy than in the AE42 alloy. The higher overall concentration of Al in the AE42 alloy indicates a higher susceptibility to the formation of β -phase, possibly contributing to a lower alloy creep resistance.

These observations agree with earlier neutron diffraction results, where the AE42 alloy was seen to have a lower creep resistance than the AJ32 alloy at both 150°C and 175°C.

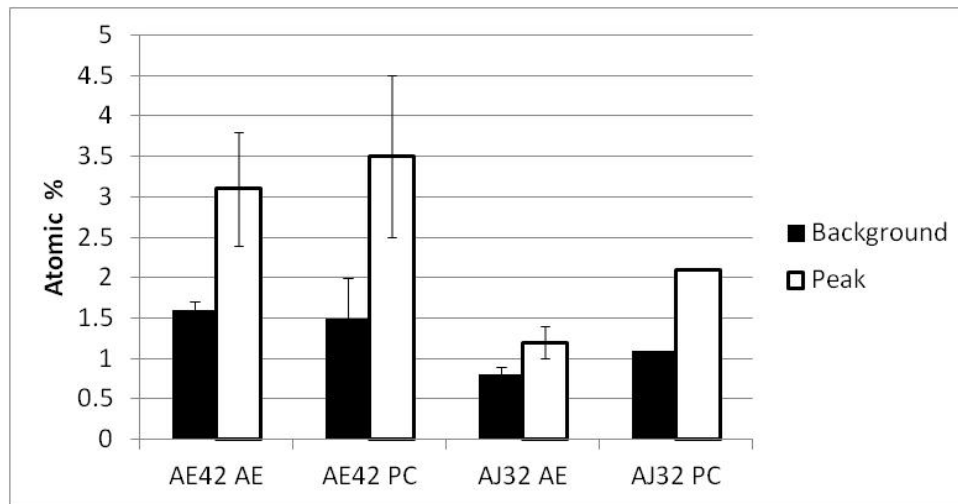


Figure 86. Peak and background Al At% for the AE42 and AJ32 alloy in their as-extruded and post-creep conditions

5.2.6 β -phase Analysis Using Optical Microscopy

Optical microscopy was used to characterize the β -phase in the AE42, AJ32 and AX30 alloys in their as-extruded and post-creep conditions. As mentioned in the previous section, β -phase was found in the AE42 alloy in the as-extruded condition and in the AE42 and AJ32 alloys post-creep. No β -phase was found in the as-extruded AX30 alloy, but was found in the post-creep AX30 alloy. Micrographs showing the as-extruded and post-creep microstructure of the AE42, AJ32 and AX30 alloys are given in Figure 87. In Figure 87, the β -phase is seen to appear along the grain boundaries and in the grains of all three alloys.

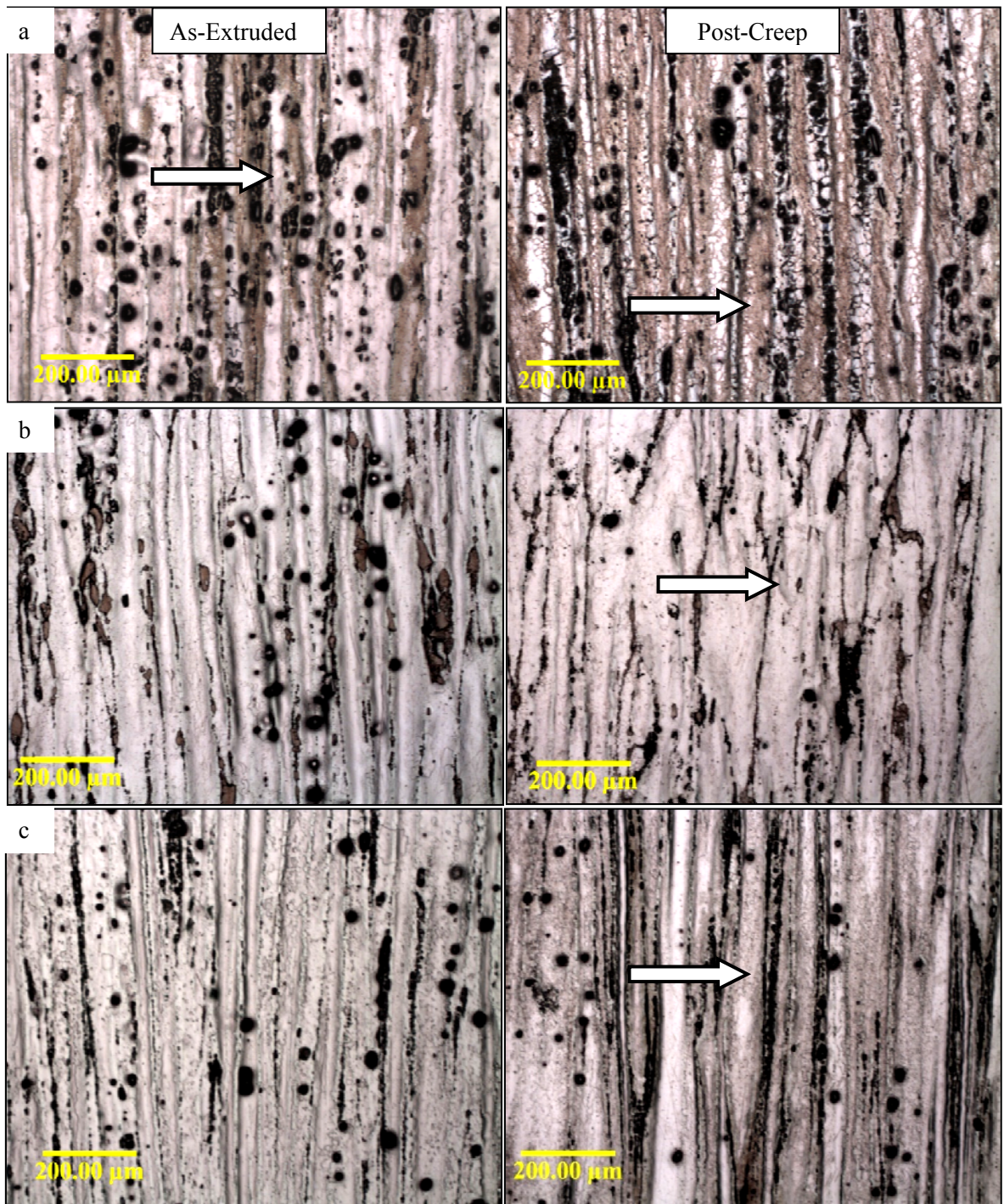


Figure 87. β -phase in the: a) AE42 alloy, b) AJ32 alloy and c) AX30 alloy

A closer inspection was performed on the AE42, AJ32 and AX30 alloys, as-extruded and post-creep, to analyze the β -phase morphology and location of formation (Figure 88). In the as-extruded AE42 alloy, the β -phase formed along grain and subgrain boundaries and near the intermetallic compounds. The density of the β -phase appeared to decrease in the vicinity of some intermetallic compounds; however, not enough to prohibit β -phase formation altogether.

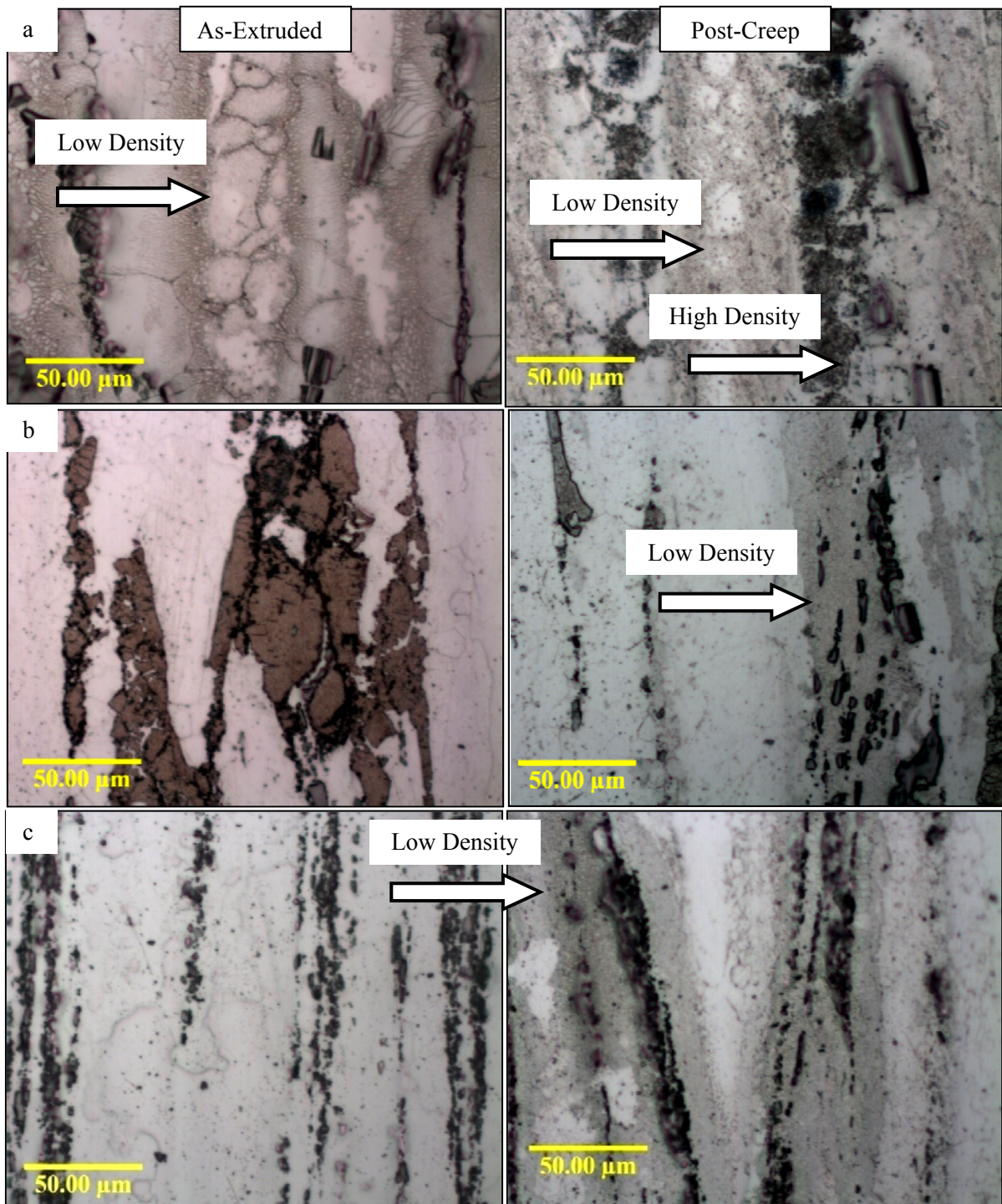


Figure 88. Location of β -phase in the: a) AE42 alloy, b) AJ32 alloy and c) AX30 alloy

As mentioned in the previous section, the post-creep AE42 alloy contained low density and a high density fibrous β -phase (Figure 88a). The high density β -phase formed in close proximity to the intermetallics, indicating that its formation was due to Al being released from the intermetallics during elevated temperature creep. The β -phase in the AE42 alloy also appeared to have moved out from the grain boundaries along the subgrain boundaries into the grains (Figure 89).

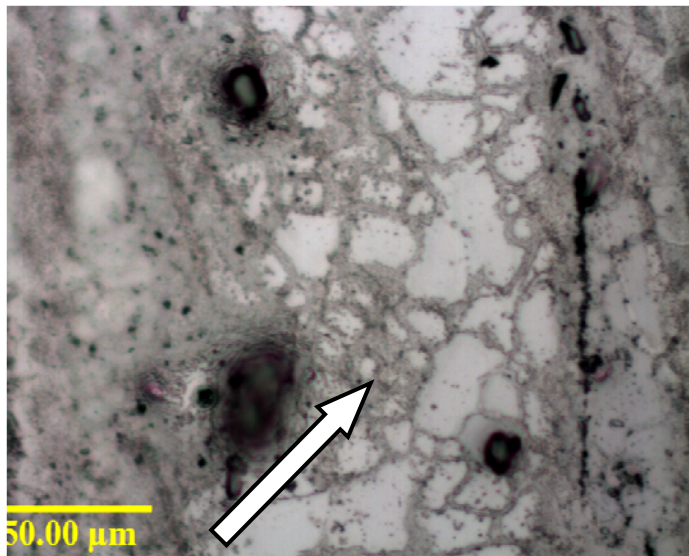


Figure 89. Formation of β -phase along subgrain boundaries in the AE42 alloy

The AJ32 alloy had the least amount of β -phase observed in the post-creep condition out of the Al-containing alloys (Figure 88). The β -phase was present along the grain boundaries surrounding both the Al_3Sr and $AlMn$ intermetallic particles, possibly indicating their low thermal stability. The post-creep AX30 alloy contained β -phase, which also surrounded the intermetallics along grain boundaries and tended to spread into the matrix material.

In summary, the AE42 alloy contained more β -phase than the AJ32 or AX30 alloys. Thus, it appears that Sr was the most effective alloying element to bind Al from the matrix, followed by Ca and REs. A strong correlation was also present between the amount of the β -phase found in the alloys and the alloys' creep resistance. The creep resistance of the three alloys increased with a decreasing amount of β -phase.

5.2.7 Zn and Zr Segregation Analysis Using an SEM

As seen in the SEM micrographs in Figure 90, solute segregation occurred in the center of the grains for both the as-extruded and post-creep conditions of the ZE10 alloy. XEDS element mapping was unsuccessful at accurately identifying the solute elements that segregated; therefore, linescans were performed perpendicular to the solute bands.

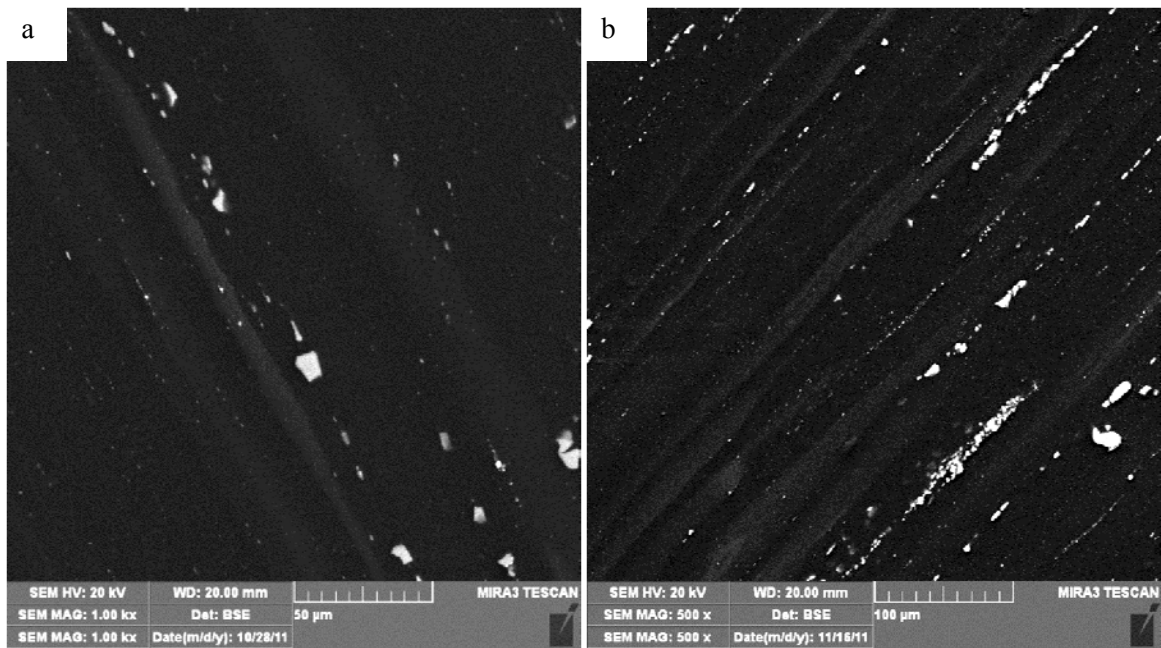


**Figure 90. Solute segregation of Zr in the ZE10 alloy:
a) As-extruded and b) Post-creep**

An example of a linescan performed in the as-extruded ZE10 alloy can be seen in Figure 91, where both Zr and Zn were seen to increase in concentration over the solute band. Therefore, Zn and Zr were the solutes that segregated in ZE10. Linescans were performed in the as-extruded and post-creep samples of the ZE10 alloy and the peak and background atomic compositions and band widths for both Zn and Zr were detected (Figure 92, with error bars depicting the standard deviation). Both Zn and Zr showed a decrease in their peak atomic concentration in the post-creep ZE10 alloy, along with an increase in peak width. This indicates that rather than an increase in Zn or Zr in the matrix (as seen in the previous sections with Al), both Zn and Zr were mobile at elevated temperatures. Future work is needed to more accurately quantify the solute segregation and dispersion at elevated temperatures.

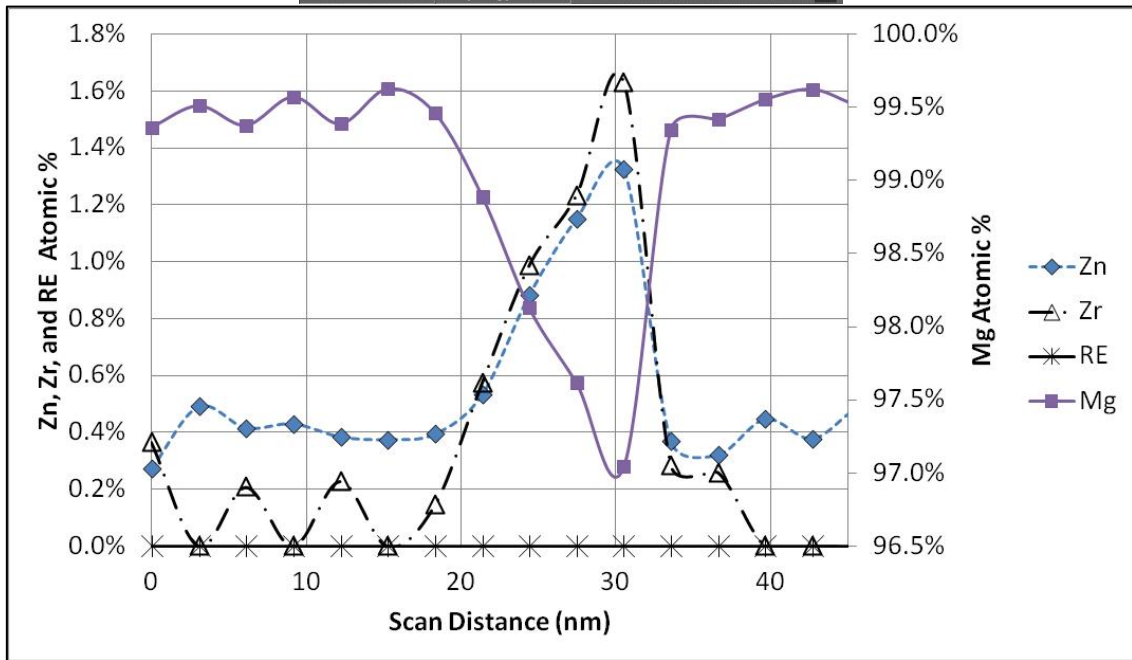
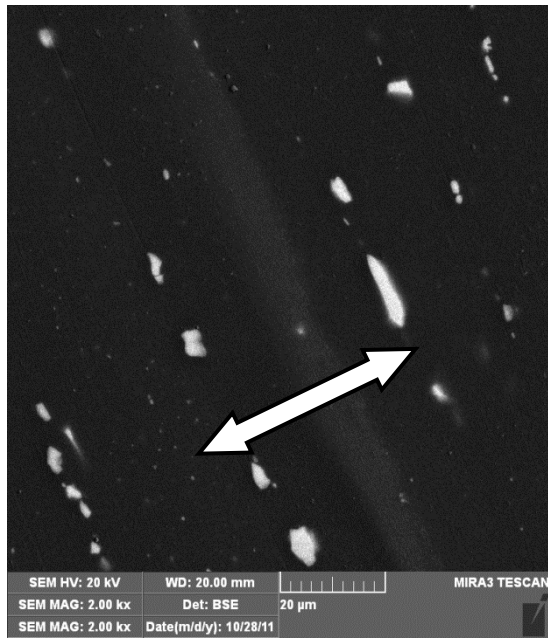


Figure 91. Zn and Zr segregation in as-extruded ZE10 showing the: a) Location of linescan and b) Atomic composition

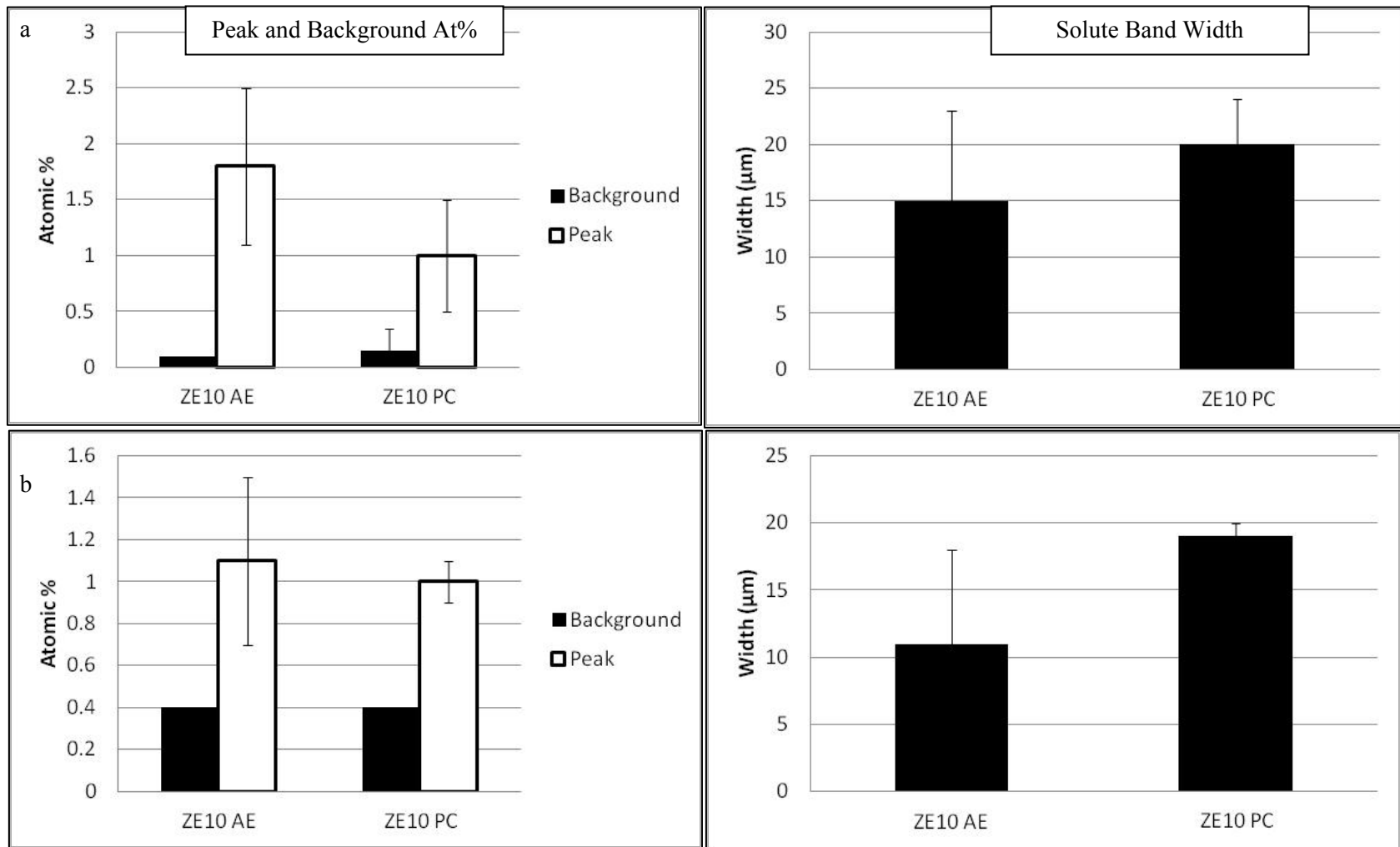


Figure 92. Segregation in ZE10 alloy: a) Zr and b) Zn

6.0 Conclusions

The results of this research show that Al containing alloys have a lower creep resistance compared to Al-free alloys. Thermal degradation of intermetallics and material twinning had a large impact on the creep resistance of the studied alloys, while the grain and subgrain structure appeared to have little or no effect.

The specific conclusions are as follows:

6.1 Neutron Diffraction

The AE42 alloy had the lowest creep resistance, followed by AJ32 and ZE10, which indicated that the addition of Sr was more effective at increasing alloy creep resistance than the addition of REs to Al containing alloys. The ZE10 alloy had a better creep resistance than either the AE42 or AJ32 alloys. The elastic strains in the AE42 alloy showed the greatest variation during testing, indicating that the alloy undergoes lattice-level changes and transformations during creep.

Residual strains were only found in the EZ33 alloy after tensile-creep testing at 150°C, suggesting effective grain pinning. No residual strains were found in the AE42, AJ32, or ZE10 alloys after compressive-creep testing due to strain relaxation as a result of the Bauschinger effect and/or grain boundary sliding.

Texture analysis of the AE42, AJ32, AX30 and EZ33 alloys indicated that a strong alloy texture possibly improved the alloy creep resistance. The most significant texture evolution was observed in the AE42 alloy after creep exposure.

6.2 Metallographic Analysis

The grain and subgrain sizes for all alloys remained constant for the as-extruded and post-creep conditions, indicating that grain growth did not occur during creep.

Twinning was found in all three Al containing alloys and showed a significant correlation with creep resistance. Extensive twinning in an alloy was related to a lower creep resistance. The highest number of twinned planes was seen in the AE42 alloy, followed by AX30 and AJ32. In these alloys, new twin systems on the $(10\bar{1}2)$ and $(11\bar{2}1)$ planes became operative. Twinning also occurred on the $(10\bar{1}1)$ plane during creep testing of the AX30 alloy.

Alloy intermetallics, especially β -phase, were also seen to have a significant impact on the creep resistance. The AE42 alloy contained β -phase in the as-extruded condition. Thus, the Ca and Sr added to the AX30 and AJ32 alloys, respectively, were more effective at binding excess Al into

intermetallics than the addition of REs to the AE42 alloy. After creep testing, β -phase was found in all Al containing alloys, with the greatest amount found in the AE42 alloy, followed by the AX30 and AJ32 alloys. The Al was released by the intermetallics in the alloys at elevated temperature, resulting in the increased formation of β -phase. The least stable intermetallic in the AE42 alloy was $Al_{11}RE_3$, which was observed to degrade into $(Al_{11}RE_3)Mg_x$. In the AJ32 alloy, both the Al_3Sr and $AlMn$ intermetallics degraded during creep testing, resulting in β -phase formation around these particles.

The ZE10 alloy contained irregular complex intermetallics and nanoprecipitates along the grain boundaries and throughout the matrix, respectively. These particles had a high thermal stability and possibly contributed to the high creep resistance of the ZE10 alloy. Segregation of Zn and Zr was observed, however the impact of these solute bands on creep resistance has not yet been confirmed.

6.3 Recommendations for Future Work

This research involved a comprehensive analysis of the creep resistance and material properties of five Mg alloys. However, more research should be completed to fully understand all mechanisms responsible for the behaviour of the alloys at elevated temperatures. For example:

1. Total deformation should be measured during compressive-creep testing at 175°C for longer than 23 hours, to ensure steady state creep has been reached and to give an accurate comparison to creep testing under standard testing conditions.

2. Neutron diffraction analysis should be performed on the AX30 and EZ33 alloys to complete the comprehensive analysis on all five alloys.

3. Neutron diffraction and metallographic analysis should be performed on the radial sections of the alloys.

4. Electron Backscatter Diffraction (EBSD) testing should be performed to analyze the crystallographic orientation of the alloy grains. This analysis will aid in accurate analysis of subgrain formation and twinning planes.

5. Comprehensive intermetallic analysis should be performed on the AX30 and EZ33 alloys to determine their intermetallic compositions and stability.

References

1. Rollason, E.C., 1959. Metallurgy for Engineers; Second Edition. Butler and Tanner Ltd., London.
2. Avedesian, M., Baker, H., 1999. ASM specialty handbook; Mg and Mg alloys. ASM International, Materials park, OH.
3. Emley, E., 1966. Principles of Mg Technology. Pergamon Press, Long Island City, NY.
4. Haughton, J.L., Prytherch, W.E., 1937. Magnesium and its alloys. Department of Scientific and Industrial Research, London.
5. Gupta, M., Sharon, N.M.L., 2011. Magnesium, magnesium alloys, and magnesium composites. John Wiley & Sons, Inc., Hoboken, NJ.
6. Hertzberg, R.W., 1996. Deformation and fracture mechanics of engineering materials. John Wiley & Sons.
7. Dieter, G.E., 1986. Mechanical metallurgy. McGraw-Hill, Boston, MA. pp. 103-635.
8. Callister, W.D., 2007. Materials science and engineering; An introduction. John Wiley & Sons, Inc., PA.
9. Dieringa, H., Hort, N., Kainer, K.U., 2009. Investigation of minimum creep rates and stress exponents calculated from tensile and compressive creep data of magnesium alloy AE42. Materials Science and Engineering A, **510-511**:382-386.
10. Gharghour, M.A., Weatherly, G.C., Embury, J.D., Root, J., 1999. Study of the mechanical properties of Mg-7.7At% Al by in-situ neutron diffraction. Philosophical Magazine A, **79(7)**:1671-1695.
11. Barnett, M.R., 2007. Twinning and the ductility of magnesium alloys; Part I: "Tension" twins. Materials and Science Engineering A, **464**:1-7.
12. Cullity, B.D., Stock, S.R., 2001. Elements of x-ray diffraction; Third edition. Prentice-Hall, Inc., NJ.
13. Kim, B.-N., Hiraga, K., 2000. Contribution of grain boundary sliding in diffusional creep. Scripta Materialia, **42**:451-456.
14. Hort, N., Huang, Y., Kainer, K.U., 2006. Intermetallics in magnesium alloys. Advanced Engineering Materials, **8(4)**: 235-240.
15. Bichler, L., Ravindran, C., Sediako, D., 2009. Onset of hot tearing in AE42 magnesium alloy. Canadian Metallurgical Quarterly, **48(1)**:81-90.
16. Peng, L., Yang, F., Nie, J.F., Li, J.C.M., 2005. Impression creep of a Mg-8Zn-4Al-0.5Ca alloy. Materials Science and Engineering A, **410-411**: 42-47.
17. Guo, Q., Yan, H.G., Chen, Z.H., Zhang, H., 2006. Elevated temperature compression behavior of Mg-Al-Zn alloys. Materials Science and Technology, **22(6)**: 725-729.

18. Blum, W., Zhang, P., Watzinger, B., Grossmann, B.V., Haldenwanger, H.G., 2001. Comparative study of creep of the die-cast Mg-alloys AZ91, AS21, AS41, AM60 and AE42. *Materials Science and Engineering A* **319-321**:735-740.
19. Seitz, F., 1943. *The physics of metals; Metallurgy and metallurgical engineering series*. McGraw-Hill Book Company Inc., London.
20. Jordon, J.B., Gibson, J.B., Horstemeyer, M.F., Kadiri, H.E., Baird, J.C., Luo, A.A., 2011. Effect of twinning, slip, and inclusions on the fatigue anisotropy of extrusion-textured AZ61 magnesium alloy. *Materials Science and Engineering A*, **528**:6860-6871.
21. Mukai, T., Yamanoi, M., Watanabe, H., Higashi, K., 2001. Ductility enhancement in AZ31 magnesium alloy by controlling its grain structure. *Scripta Materialia*, **45**:89-94.
22. Serope, K., Schmid, S.R., 2006. *Manufacturing engineering and technology*. Pearson Prentice Hall, NJ.
23. Jing, B., Yangshan, S., Feng, X., Shan, X., Jing, Q., Weijian, T., 2006. Effect of extrusion on microstructures, and mechanical and creep properties of Mg-Al-Sr and Mg-Al-Sr-Ca alloys. *Scripta Materialia*, **55**: 1163-1166.
24. Mabushi, M., Kubota, K., Higashi, K., 1994. Effect of hot extrusion on mechanical properties of a Mg-Si-Al alloy. *Materials Letters*, **19**:247-250.
25. Yan, J., Sun, Y., Xue, F., Bai, J., Xue, S., Tao, W., 2008. Creep deformation mechanism of magnesium-based alloys. *Journal of Material Science*, **43**: 6952-6959.
26. Laser, T., Hartig, Ch., Nürnberg, M.R., Letzig, D., Bormann, R., 2008. The influence of calcium and cerium mischmetal on the microstructural evolution of Mg-3Al-1Zn during extrusion and resulting mechanical properties. *Acta Materialia*, **56**: 2791-2798.
27. Wei, L.Y., Dunlop, G.L., Westengen, H., 1997. Solidification behaviour and phase constituents of cast Mg-Zn-misch metal alloys. *Journal of Materials Science*, **32**:3335-3340.
28. Gjestland, H., Nussbaum, G., Regazzoni, G., Lohne, O., Bauger, O., 1991. Stress-relaxation and creep behaviour of some rapidly solidified magnesium alloys. *Materials Science and Engineering A*, **134**:1197-1200.
29. Zheng, J., Wang, Q., Jin, Z., Peng, T., 2010. The microstructure, mechanical properties and creep behavior of Mg-3Sm-0.5Zn-0.4Zr (wt%) alloy produced by different casting technologies. *Journal of Alloys and Compounds*, **496**:351-356.
30. Gruzleski, J.E., 2000. *Microstructure development during metal casting*. American Foundrymen's Society, Inc., Illinois.
31. Bochenek, A., Braszczyńska, K.N., 2000. Structural analysis of the MgAl5 matrix cast composites containing SiC particles. *Materials Science and Engineering A* **290**:122-127.

32. Asl, K.M., Tari, A., Khomamizadeh, F., 2009. The effect of different content of Al, RE and Si element on the microstructure, mechanical and creep properties of Mg-Al alloys. *Materials Science and Engineering A* **523**:1-6.
33. Nami, B., Razavi, H., Mirdamadi, S., Shabestari, S.G., Miresmaeili, S.M., 2010. Effect of Ca and rare earth elements on impression creep properties of AZ91 magnesium alloy. *Metallurgical and Materials Transactions A*, **41A**:1973-1982.
34. Kabirian, F., Mahmudi, R., 2010. Effects of Zr additions on the microstructure and impression creep behaviour of AZ91 magnesium alloy. *Metallurgical and Materials Transactions A*, **41A**:3488-3498.
35. Murray, J.L., 1988. ASM Handbooks online; Volume 3; Alloy phase diagrams. ASM International. Available from <http://products.asminternational.org/hbk/index.jsp> [Cited February 8, 2012]
36. Powell, B.R., Rezhets, V., Balogh, M.P., and Waldo, R.A., 2002. Microstructure and creep behavior in AE42 Magnesium die-casting alloy. *Journal of Metals*, **54**(8): 34-38.
37. Mordike, B.L., 2002. Creep-resistant magnesium alloys. *Material Science and Engineering A*, **324**: 103-112.
38. Okamoto, H., 2007. ASM Handbooks online; Volume 3; Alloy phase diagrams. ASM International. Available from <http://products.asminternational.org/hbk/index.jsp> [Cited February 8, 2012]
39. Xue, S., Sun, Y.S., Ding, S.S., Bai, Q., Bai, J., 2005. Effects of Calcium additions on microstructure and creep behaviour of AE42 alloy. *Materials Science and Engineering A*, **21**(7): 847-853.
40. Dargusch, M.S., Zhu, S.M., Nie, J.F., Dunlop, G.L., 2009. Microstructural analysis of the improved creep resistance of a die-cast magnesium-aluminium-rare earth alloy by strontium additions. *Stripta Materialia*, **60**: 116-119.
41. Kirkland, N.T., Birbilis, N., Walker, J., Woodfield, T., Dias, G.J., Staiger, M.P., 2010. In-vitro dissolution of magnesium-calcium binary alloys: Clarifying the role of calcium additions in bioresorbable magnesium implant alloys. *Journal of Biomedical Materials Research B*, **1** (95B): 91-100.
42. Ninomiya, R., Ojiro, T., Kubota, K., 1995. Improved heat resistance of Mg-Al alloys by the Ca addition. *Acta Mater.*, **43** (2): 669-674.
43. Chino, Y., Nakaura, Y., Otori, K., Kamiya, A., Mabuchi, M., 2007. Mechanical properties at elevated temperature of a hot-deformed Mg-Al-Ca-Mn-Sr alloy. *Materials Science and Engineering A*, **452-453**:31-36.

44. Nayeb-Hashemi, A.A., Clark, J.B., 1988. ASM Handbooks online; Volume 3; Alloy phase diagrams. ASM International. Available from <http://products.asminternational.org/hbk/index.jsp> [Cited February 8, 2012]
45. Rokhlin, L.L., Dobatkina, T.V., Nikitina N.I., Tarytina, I.E., 2009. Calcium-alloyed magnesium alloys. *Material Science and Heat Treatment*, **51**(4):14-19.
46. Nami, B., Razavi, H., Miresmaeili, S., Mirdamadi, Sh., Shabestari, S., 2011. Impression creep properties of a semi-solid processed magnesium-aluminum alloy containing calcium and rare earth elements. *Scripta Materialia*, **65**:221-224.
47. Baril, E., Labelle, P., Pekguleryuz, M.O., 2003. Elevated temperature Mg-Al-Sr: Creep resistance, mechanical properties, and microstructure. *JOM*, **55** (11): 34-39.
48. Tkachenko, V., Kim, K., Moon, B., Vovchok, A., 2011. Design and microstructural analysis of magnesium alloys for dynamic applications. *Journal of Material Science*, **46**: 4880-4895.
49. Clark, J.B., Zabdyr, L., Moser, Z., 1988. ASM Handbooks online; Volume 3; Alloy phase diagrams. ASM International. Available from <http://products.asminternational.org/hbk/index.jsp> [Cited February 8, 2012]
50. Ryspaev, T., Trojanova, Z., Padalka, O., Wesling, V., 2008. Microstructure of superplastic QE22 and EZ33 magnesium alloys. *Materials Letters*, **62**: 4041-4043.
51. Shook, S., Sediako, D., n.d.. Analysis of stress evolution in high temperature creep testing of creep-resistant magnesium alloys.
52. Zhou, T., Xia, H., Chen, Z.H., 2011. Effect of Ce on microstructures and mechanical properties of rapidly solidified Mg-Zn alloy. *Materials Science and Technology*, **27**(7):1198-1205.
53. Allen, A.J., Bourke, A.M., Dawes, S., Hutchings, M.T., Withers, P.J., 1991. The analysis of internal strains measured by neutron diffraction in Al/SiC metal matrix composites. *Acta Metall. Mater.*, **40**(9):2361-2373.
54. Fitter, J., Gutberlet, T., Katsaras, J., 2006. *Neutron scattering in Biology; Techniques and applications*. Springer, Germany.
55. Sediako, D., Shook, S., Vogel, S.C., Sediako, A., 2010. Application of neutron diffraction in characterization of texture evolution during high-temperature creep in magnesium alloys. *In Canadian Nuclear Society Meeting 2010, Montreal*.
56. Yoon, K.P., Hwang, C.L., 1995. *Multiple attribute decision making; An introduction*. Sage Publications, Thousand Oaks, CA.

Appendices

Appendix A – Phase Diagrams

Phase diagrams for Mg-Ce, Mg-La and Mg-Pr alloy systems.

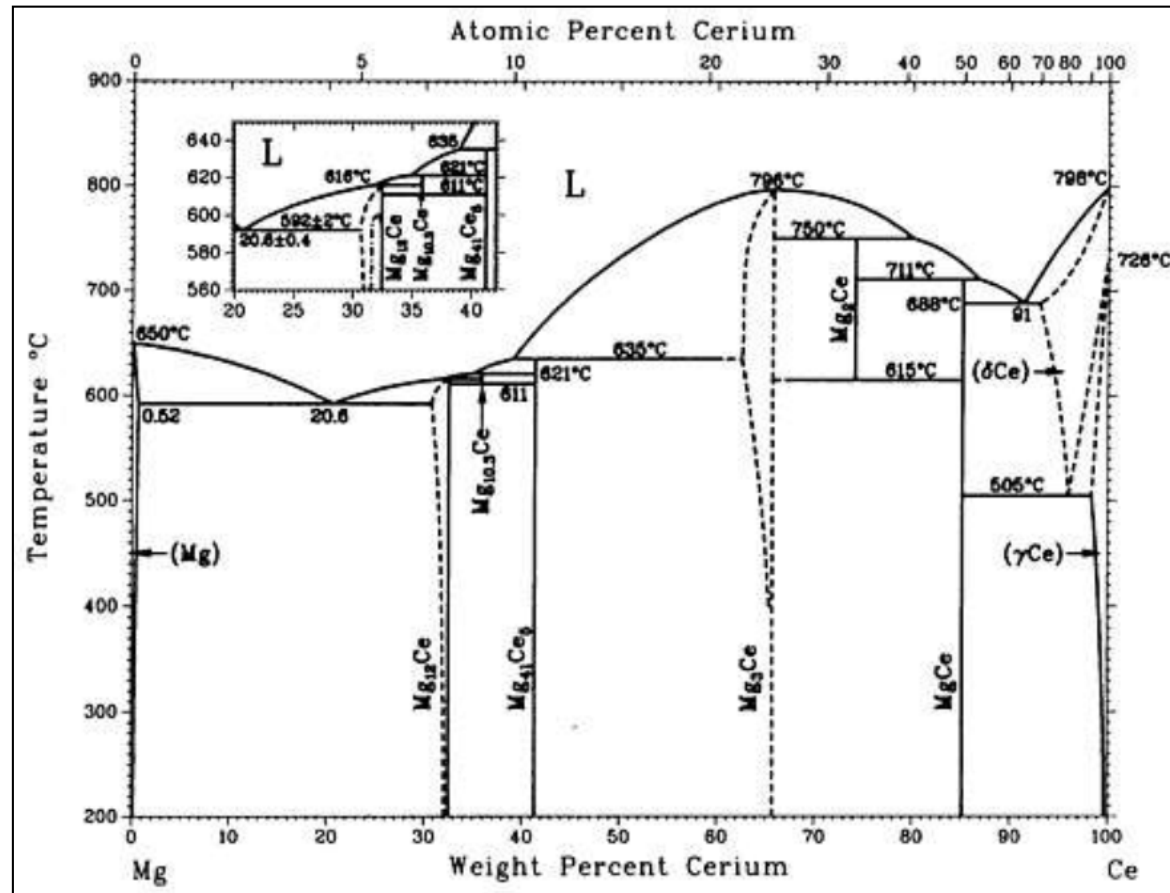


Figure 93. Mg-Ce phase diagram [46]

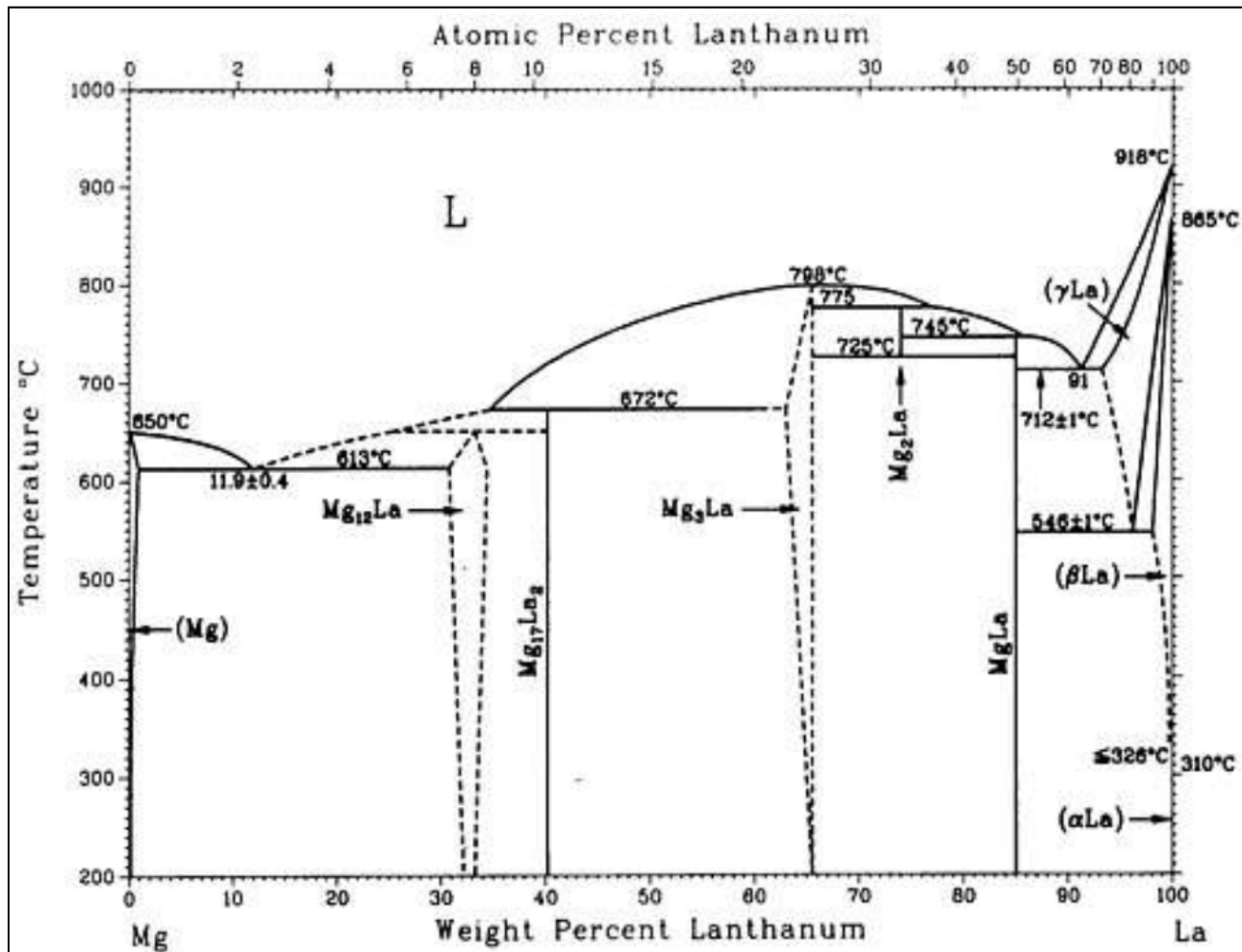


Figure 94. Mg-La phase diagram [46]

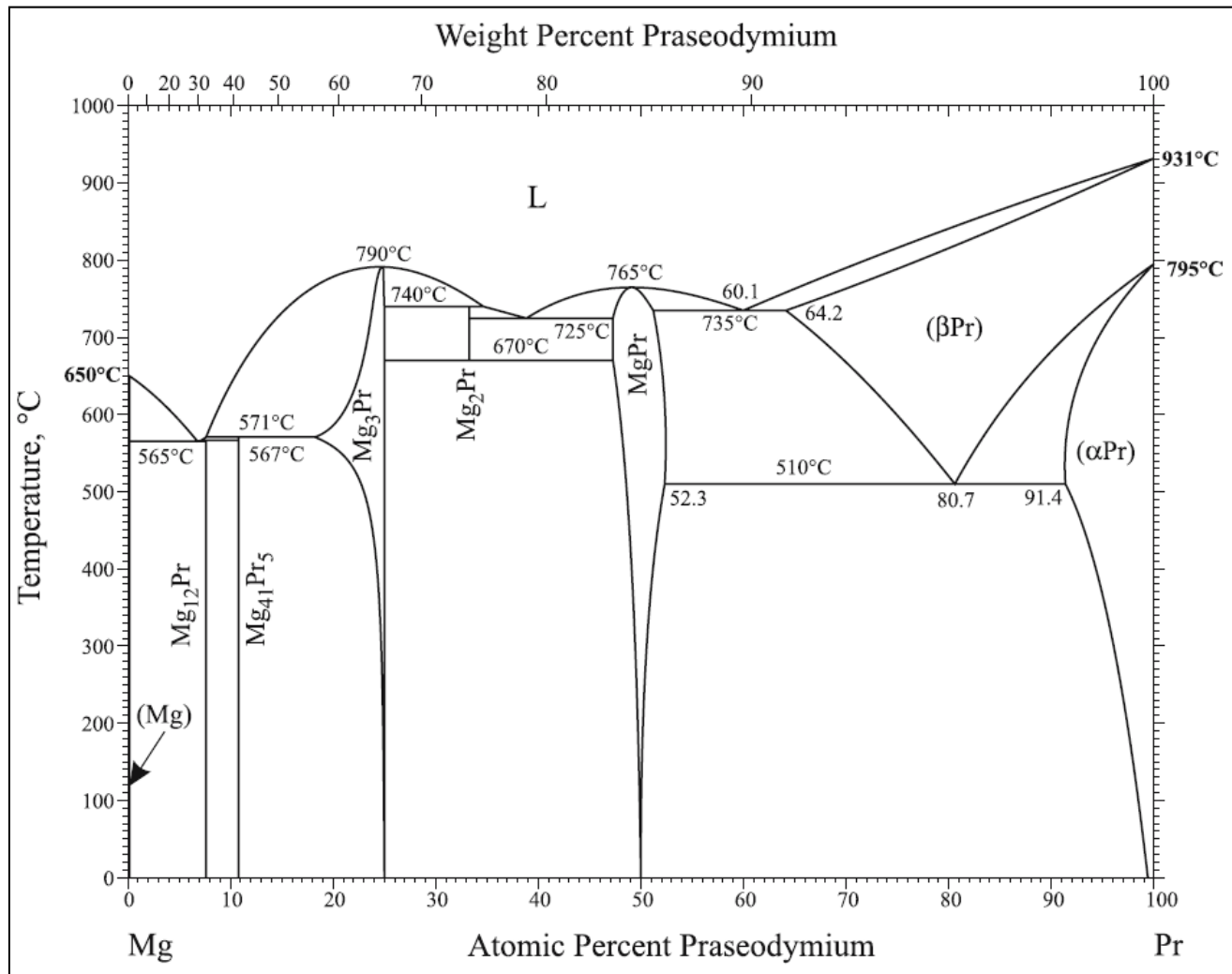
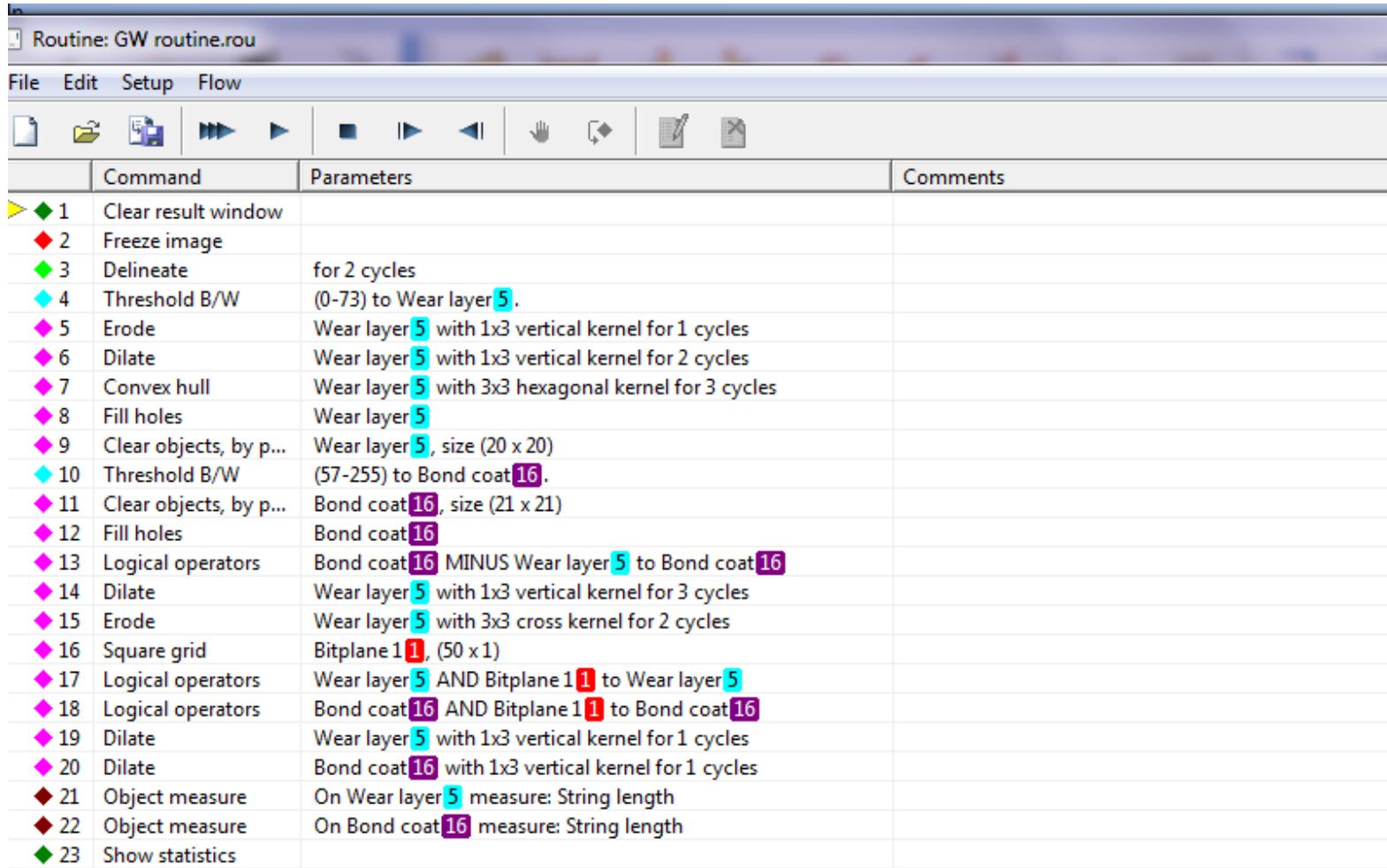


Figure 95. Mg-Pr phase diagram [40]

Appendix B – Optical Microscopy Routines

Routines used during image analysis (Buehler OmniMet software) are outlined in this section.



	Command	Parameters	Comments
1	Clear result window		
2	Freeze image		
3	Delineate	for 2 cycles	
4	Threshold B/W	(0-73) to Wear layer 5.	
5	Erode	Wear layer 5 with 1x3 vertical kernel for 1 cycles	
6	Dilate	Wear layer 5 with 1x3 vertical kernel for 2 cycles	
7	Convex hull	Wear layer 5 with 3x3 hexagonal kernel for 3 cycles	
8	Fill holes	Wear layer 5	
9	Clear objects, by p...	Wear layer 5, size (20 x 20)	
10	Threshold B/W	(57-255) to Bond coat 16.	
11	Clear objects, by p...	Bond coat 16, size (21 x 21)	
12	Fill holes	Bond coat 16	
13	Logical operators	Bond coat 16 MINUS Wear layer 5 to Bond coat 16	
14	Dilate	Wear layer 5 with 1x3 vertical kernel for 3 cycles	
15	Erode	Wear layer 5 with 3x3 cross kernel for 2 cycles	
16	Square grid	Bitplane 1 1, (50 x 1)	
17	Logical operators	Wear layer 5 AND Bitplane 1 1 to Wear layer 5	
18	Logical operators	Bond coat 16 AND Bitplane 1 1 to Bond coat 16	
19	Dilate	Wear layer 5 with 1x3 vertical kernel for 1 cycles	
20	Dilate	Bond coat 16 with 1x3 vertical kernel for 1 cycles	
21	Object measure	On Wear layer 5 measure: String length	
22	Object measure	On Bond coat 16 measure: String length	
23	Show statistics		

Figure 96. Buehler OmniMet routine for alloy grain width

Routine: michelles routine (% intermetallics).rou		
File Edit Setup Flow		
[Icons: File, Folder, Print, Play, Stop, Previous, Next, Hand, Refresh, Erase, Copy]		
	Command	Parameters
▶	1 Freeze image	
◆	2 Setup ROI	(3,3) to (767,767)
◆	3 Clear result window	
◆	4 Delineate	for 2 cycles
◆	5 Threshold B/W	(137-255) to Wear layer 5.
◆	6 Threshold B/W	(130-255) to Bitplane 8 8.
◆	7 Close	Wear layer 5 with 3x3 hexagonal kernel for 1 cycles
◆	8 Close	Bitplane 8 8 with 3x3 hexagonal kernel for 1 cycles
◆	9 Dilate	Wear layer 5 with 3x3 hexagonal kernel for 1 cycles
◆	10 Fill holes	Bitplane 8 8
◆	11 Erode	Wear layer 5 with 3x3 hexagonal kernel for 1 cycles
◆	12 Clear outside ROI	Wear layer 5
◆	13 Clear outside ROI	Bitplane 8 8
◆	14 Clear objects, by feature	Bitplane 8 8, String Length < 0.00 μm
◆	15 Logical operators	Wear layer 5 MINUS Bitplane 8 8 to Bitplane 8 8
◆	16 Relative bitplane area	Wear layer 5 relative to ROI area
◆	17 Object measure	On Wear layer 5 measure: Circular diameter
◆	18 Object measure	On Wear layer 5 measure: Circular diameter, Spherical diameter, Sphericity
◆	19 Field measure	On Wear layer 5 measure: Area fraction, Anisotropy, Average circular diameter, Average spherical diameter
◆	20 Object measure	On Bitplane 8 8 measure: Area, Circular diameter
◆	21 Relative bitplane area	Bitplane 8 8 relative to ROI area
◆	22 Field measure	On Bitplane 8 8 measure: Average circular diameter
◆	23 Show result window	
◆	24 Prune	Bitplane 1 1 with 3x3 hexagonal kernel for 1 cycles
◆	25 Border elimination	Bitplane 1 1
◆	26 Setup ROI	Whole image

Figure 97. Buehler OmniMet routine for intermetallic area percent

Appendix C – Metallographic Analysis

Metallographic analysis was performed using optical microscopy and scanning electron microscopy to analyze alloy grain morphology and intermetallic compounds.

Appendix C.1 – Optical Microscopy

Optical microscopic techniques were used to analyze general morphology, grain width, subgrain size and twinning angles. The raw data for the grain width measurements are provided in this section.

Table 12. Raw data for average grain widths

AE42 AE @100x Grain widths									
Site	1	2	3	4	5	6	7	8	
Mean	11.82	14.03	12.83	14.71	12.15	11.48	13.14	10.3	
Min	2.46	2.46	2.46	2.46	2.46	2.46	2.46	2.46	
Max	83.68	108.3	123.88	112.4	95.17	70.56	115.68	93.53	
St. Dev.	10.09	13.98	12.56	13.2	9.88	9.46	12.81	10.36	
#pts	1548	1542	1432	1401	1644	1326	1171	1545	
area	882229.7	882229.7	882229.7	882229.7	882229.7	882229.7	882229.7	882229.7	

AE42 PCC 175 @100x Grain widths										
Site	1	2	3	4	5	6	7	8	9	10
Mean	12.81	15.44	12.51	14.39	13.81	14.86	14.08	14.58	13.14	14.28
Min	2.46	2.46	2.46	2.46	2.46	2.46	2.46	2.46	2.46	2.46
Max	76.3	89.43	79.58	65.63	97.63	110.76	95.99	101.73	68.92	83.68
St. Dev.	12.28	15.06	12.38	12.46	13.76	14.74	12.58	12.97	12.57	13.43
#pts	1526	1290	1477	1428	1415	1305	1398	1417	1451	1426
area	882229.7	882229.7	882229.7	882229.7	882229.7	882229.7	882229.7	882229.7	882229.7	882229.7

AJ32 AE @100x Grain widths										
Site	1	2	3	4	5	6	7	8	9	10
Mean	16.31	19.72	19.3	19.84	16.82	21.29	18.13	20.04	19.62	20.29
Min	2.46	2.46	2.46	2.46	2.46	2.46	2.46	2.46	2.46	2.46
Max	77.12	99.27	79.58	76.3	113.22	114.86	118.9	121.4	81.2	125.5
St. Dev.	13.73	16.3	15.9	17.6	13.63	20.34	15.15	15.72	13.31	21.43
#pts	1447	1241	1260	1164	1226	1056	1175	1120	1153	1200
area	882229.7	882229.7	882229.7	882229.7	882229.7	882229.7	882229.7	882229.7	882229.7	882229.7

AJ32 PCC 175 @100x Grain widths										
Site	1	2	3	4	5	6	7	8	9	10
Mean	15.62	21.37	15.85	16.11	17.1	17.83	16.16	16.09	17.64	22.36
Min	2.46	2.46	2.46	2.46	2.46	2.46	2.46	2.46	2.46	2.46
Max	120.6	122.24	115.68	95.17	114.86	114.04	91.89	115.68	73.84	93.53
St. Dev.	16.37	22.17	17.17	16.22	16.54	18.43	16.17	17.49	15.79	19.73
#pts	1542	1159	1418	1156	1100	1387	1382	1363	1370	1086
area	882229.7	882229.7	882229.7	882229.7	882229.7	882229.7	882229.7	882229.7	882229.7	882229.7

AX30 AE @100x Grain widths										
Site	1	2	3	4	5	6	7	8	9	10
Mean	9.36	11.79	12.88	14.09	11.88	11.45	12.69	13.31	11.4	10.64
Min	2.46	2.46	2.46	2.46	2.46	2.46	2.46	2.46	2.46	2.46
Max	51.69	77.94	92.71	108.3	72.2	59.89	79.58	94.35	54.15	73.84
St. Dev.	8.29	11.55	14.57	14.99	11.16	10.7	12.14	13.84	9.96	10.43
#pts	1870	1872	1773	1589	1748	1769	1667	1642	1904	1758
area	882229.7	882229.7	882229.7	882229.7	882229.7	882229.7	882229.7	882229.7	882229.7	882229.7

AX30 PCC 175 @100x Grain widths										
Site	1	2	3	4	5	6	7	8	9	10
Mean	10.01	8.8	8.88	8.7	8.43	9.13	11	10.18	10.04	9
Min	2.46	2.46	2.46	2.46	2.46	2.46	2.46	2.46	2.46	2.46
Max	107.47	65.63	59.07	57.43	65.63	85.32	85.32	95.99	185.41	89.43
St. Dev.	12.2	9.4	9.15	9.21	8.75	9.99	13.36	12.17	14.89	11.05
#pts	1393	1830	1694	1499	1548	1854	1623	1707	1857	1758
area	882229.7	882229.7	882229.7	882229.7	882229.7	882229.7	882229.7	882229.7	882229.7	882229.7
EZ33 AE @100x Grain widths										
Site	1	2	3	4	5	6	7	8	9	10
Mean	8.42	8.07	8.57	8.56	9.31	9.58	9.13	8.97	8.69	9.03
Min	2.46	2.46	2.46	2.46	2.46	2.46	2.46	2.46	2.46	2.46
Max	51.69	83.68	59.89	70.56	58.25	74.66	72.2	59.07	79.58	67.27
St. Dev.	7.34	7.38	7.94	7.68	8.6	8.95	8.93	8.22	7.86	8.38
#pts	1827	1491	1837	1695	1902	1857	1987	1950	2006	1763
area	882229.7	882229.7	882229.7	882229.7	882229.7	882229.7	882229.7	882229.7	882229.7	882229.7
EZ33 PCC 175 @100x Grain widths										
Site	1	2	3	4	5	6	7	8	9	10
Mean	6.81	7.47	6.42	7.34	7.59	7.93	7.48	7.7	7.14	7.09
Min	2.46	2.46	2.46	2.46	2.46	2.46	2.46	2.46	2.46	2.46
Max	43.48	54.97	56.61	54.15	59.07	70.56	50.87	69.74	51.69	45.12
St. Dev.	6.62	7.22	6.12	6.9	7.39	8.4	6.93	7.65	6.75	6.83
#pts	2453	2317	2348	2451	2211	2205	2339	2249	2361	2179
area	882229.7	882229.7	882229.7	882229.7	882229.7	882229.7	882229.7	882229.7	882229.7	882229.7
ZE10 AE @100x Grain widths										
Site	1	2	3	4	5	6	7	8	9	10
Mean	17.01	16.79	19.22	13.63	17.73	16.18	16.7	14.66	15.5	17.74
Min	2.46	2.46	2.46	2.46	2.46	2.46	2.46	2.46	2.46	2.46
Max	118.14	109.94	119.76	85.32	141.93	114.04	150.14	110.76	117.32	122.24
St. Dev.	17.07	16.77	18.61	13.26	18.18	16.85	16.62	14.81	15.21	18.97
#pts	1730	1689	1574	1822	1609	1714	1732	1946	1857	1678
area	882229.73	882229.73	882229.73	882229.73	882229.73	882229.73	882229.73	882229.73	882229.73	882229.73
ZE10 PCC 175 @100x Grain widths										
Site	1	2	3	4	5	6	7	8	9	10
Mean	14.84	17.6	23.18	18.5	26.25	16.08	14.63	15.35	15.49	17.93
Min	2.46	2.46	2.46	2.46	2.46	2.46	2.46	2.46	2.46	2.46
Max	105.01	91.07	152.6	130.45	139.47	105.83	100.09	90.25	85.32	102.55
St. Dev.	14.66	17.15	22.35	18.53	26.66	16.37	13.46	14.63	14.21	15.4
#pts	1704	1594	1406	1663	1347	1832	1877	1813	1769	1709
area	882229.73	882229.73	882229.73	882229.73	882229.73	882229.73	882229.73	882229.73	882229.73	882229.73

Appendix C.2 – Scanning Electron Microscopy

SEM microscopy was used to analyze the general microstructure of the alloys, the morphology of the intermetallic compounds and solute segregation in the alloys. Additional micrographs are provided below to give an understanding of the overall microstructure of the AE42, AJ32, AX30, EZ33 and ZE10 alloys.

Appendix C.2.1 – General Microstructure

The general microstructure of each AE42, AJ32, AX30, EZ33 and ZE10 alloy in their as-extruded and post-creep conditions are provided below.

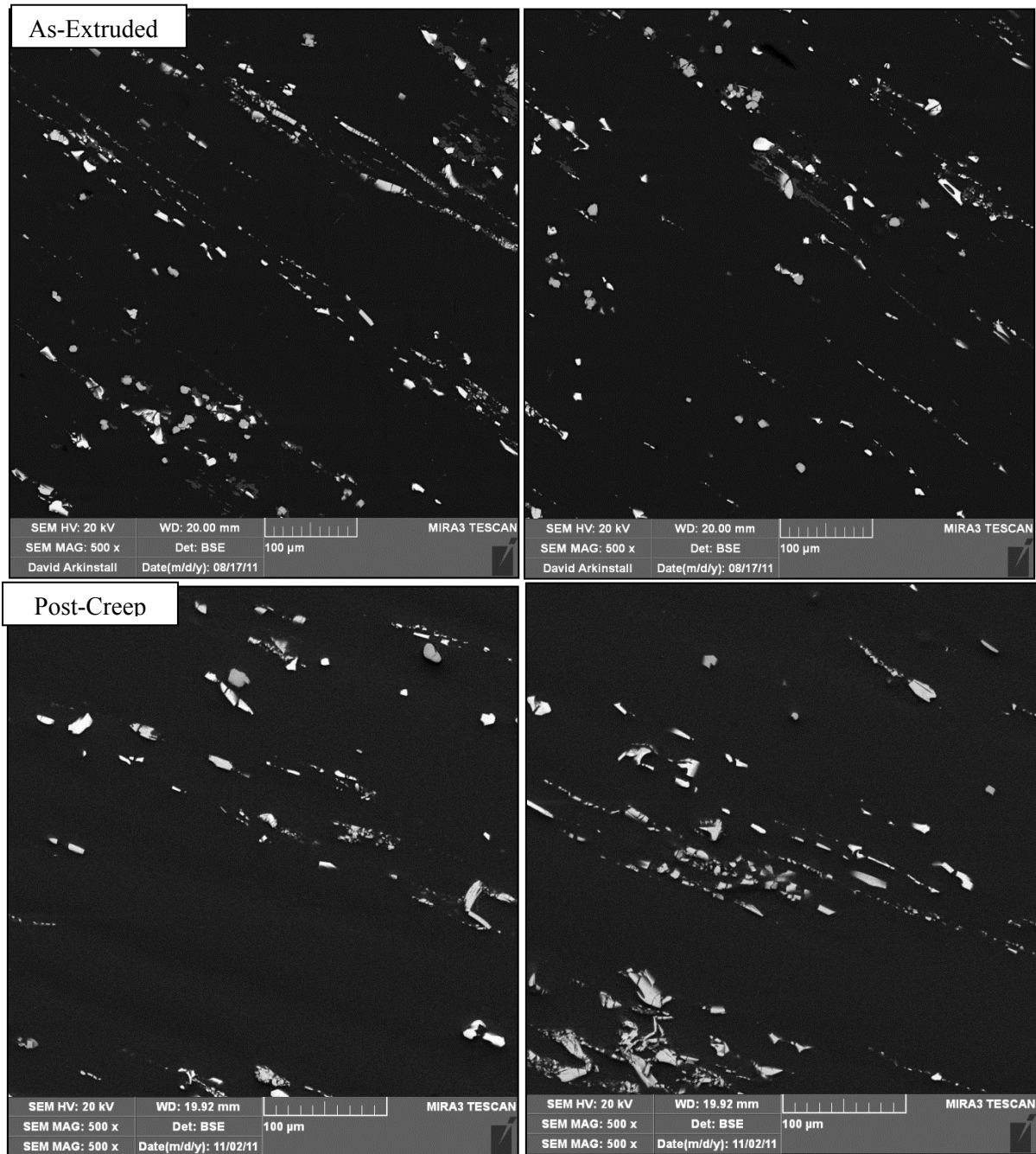


Figure 98. As-extruded and post-creep microstructure of AE42 (500x magnification)

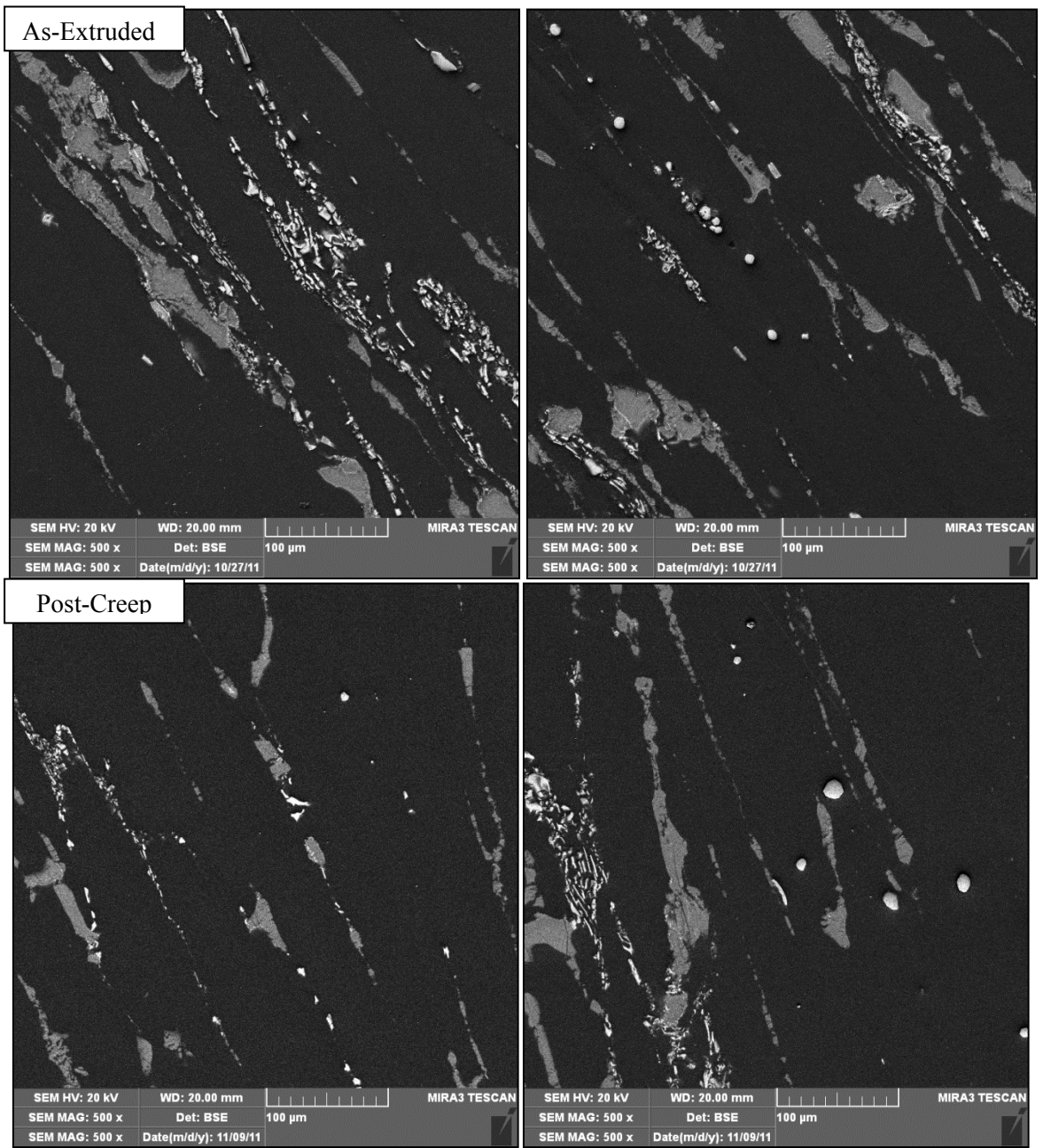


Figure 99. As-extruded and post-creep microstructure of AJ32 (500x magnification)

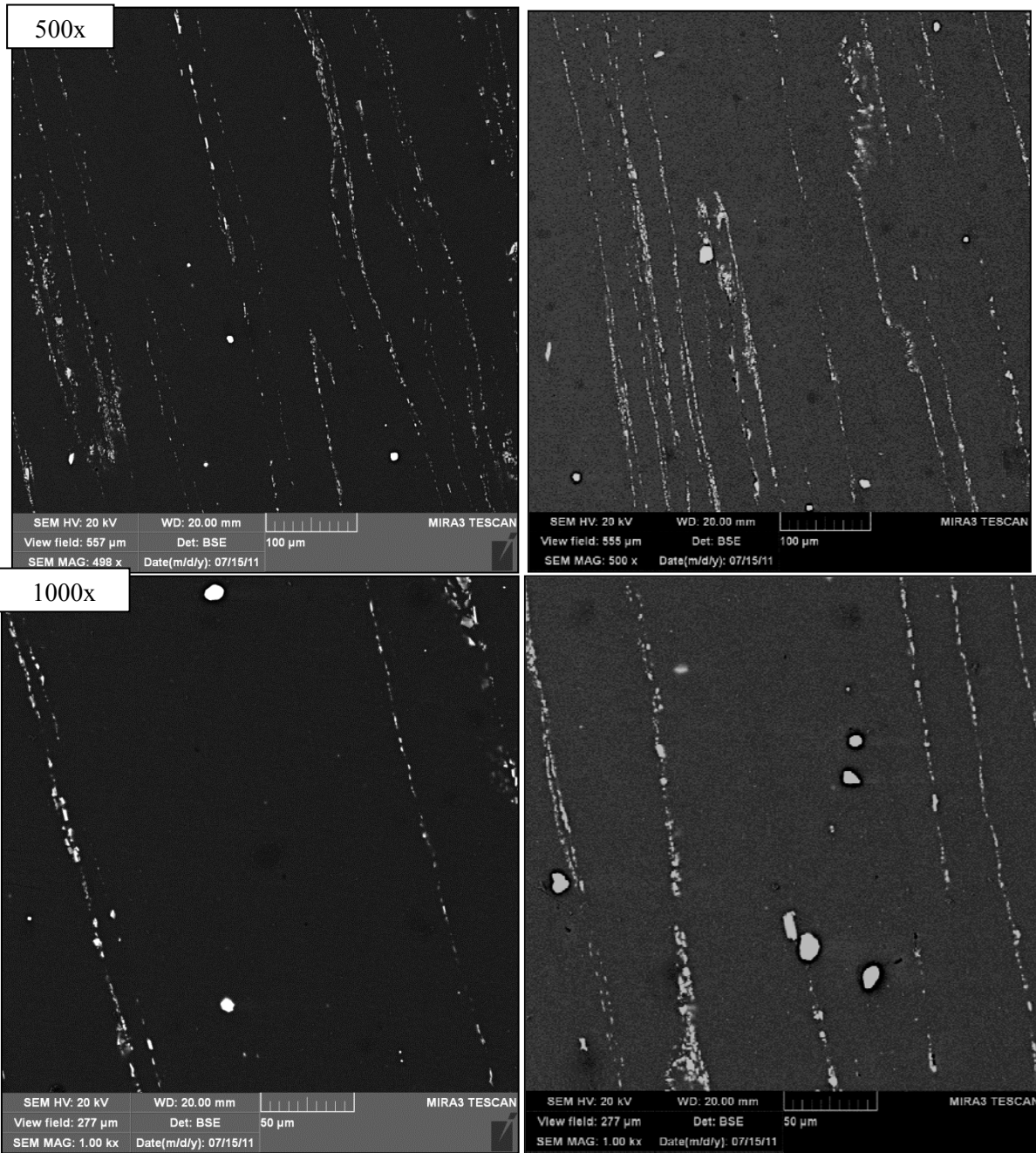


Figure 100. As-extruded microstructure of AX30 at 500x and 1000x magnification

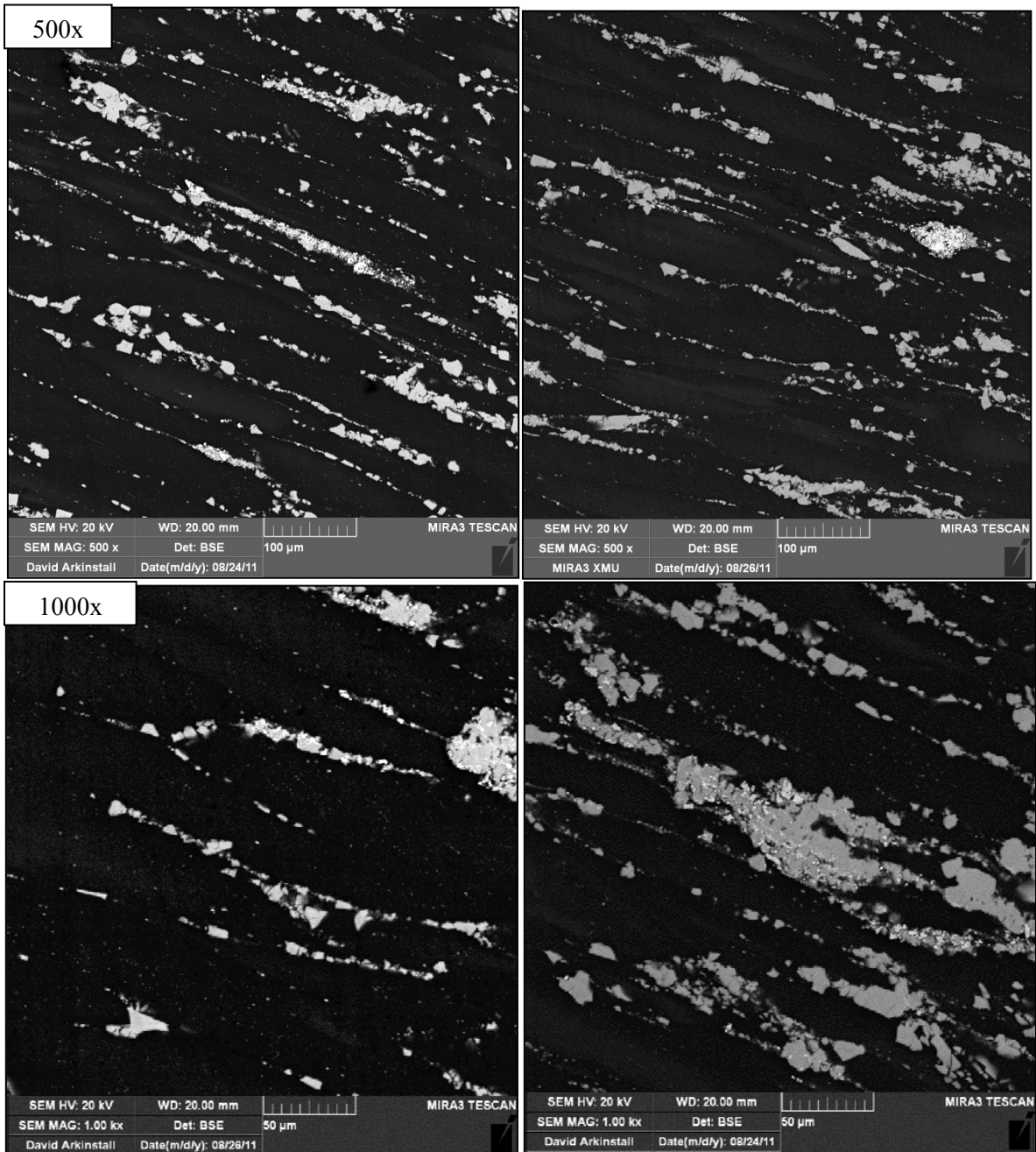


Figure 101. As-extruded microstructure of EZ33 at 500x and 1000x magnification

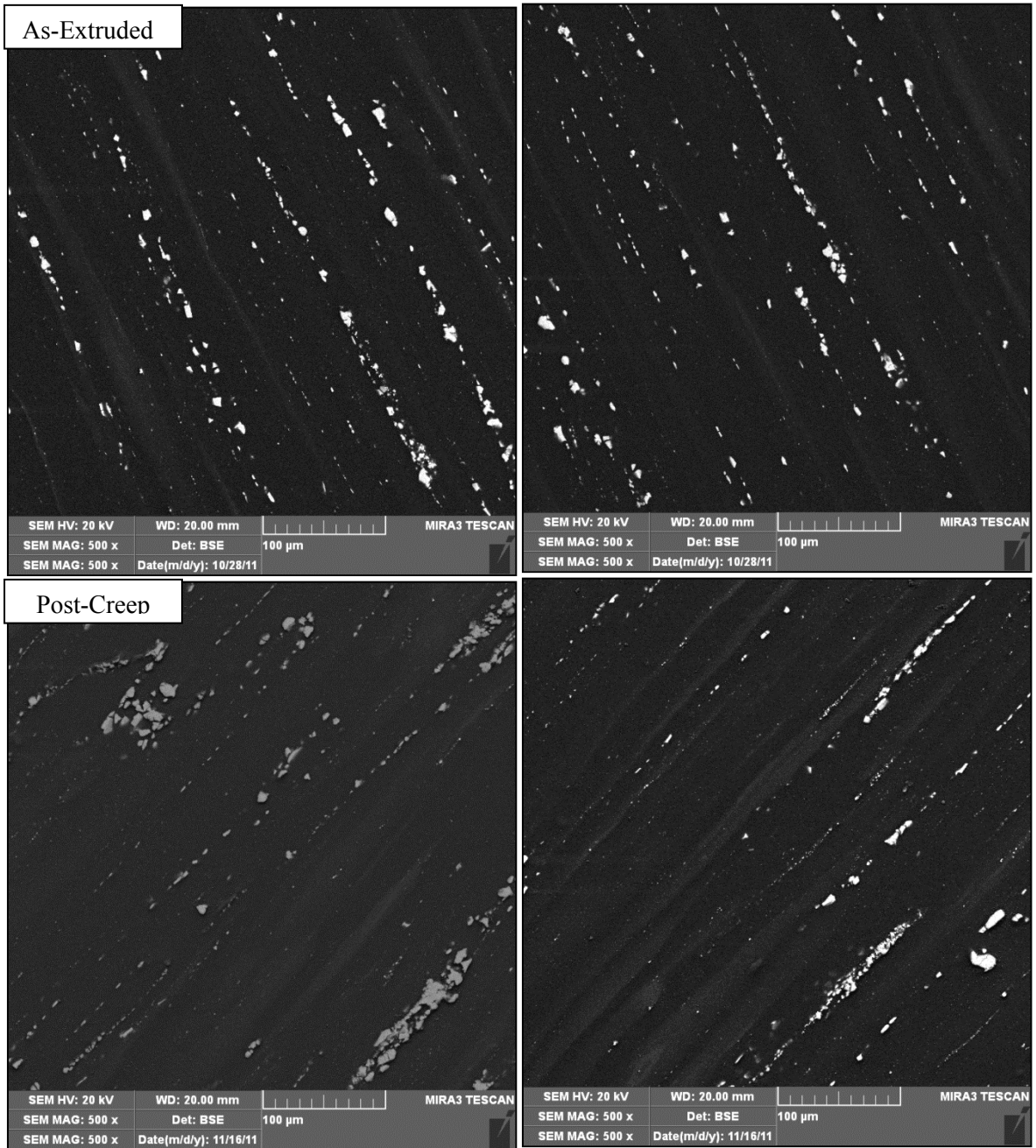


Figure 102. As-extruded and post-creep microstructure of ZE10 at 500x magnification

Appendix C.2.2 – AE42 Alloy Intermetallics

Two intermetallics were observed in the AE42 alloy: $Al_{11}RE_3$ and Al_6Mn_3RE . The structure of these intermetallics in the as-extruded alloy are provided herein. The $Al_{11}RE_3$ intermetallic compound was observed to have degraded during creep and the post-creep intermetallic structures are shown below.

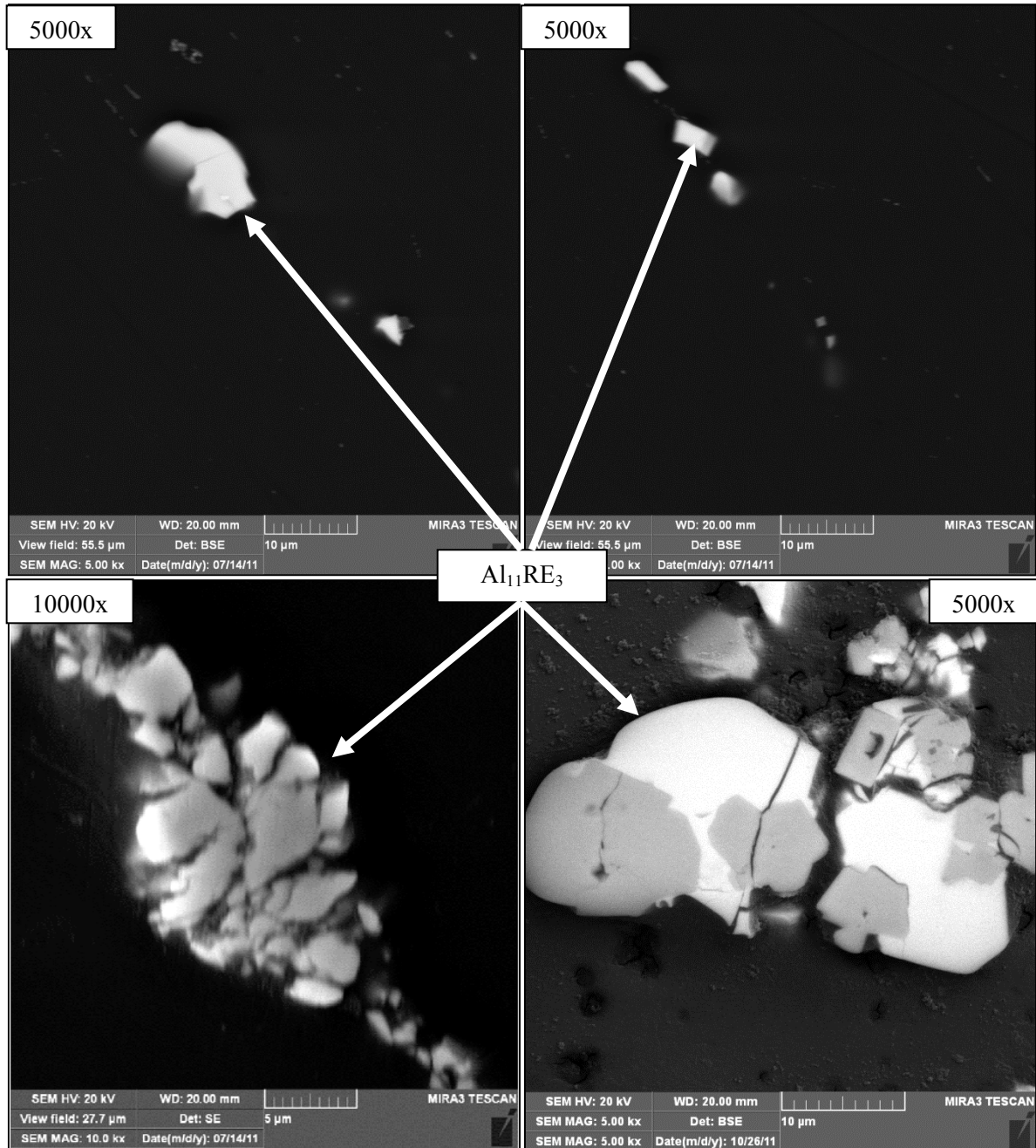


Figure 103. Structure of $Al_{11}RE_3$ in the as-extruded AE42 alloy

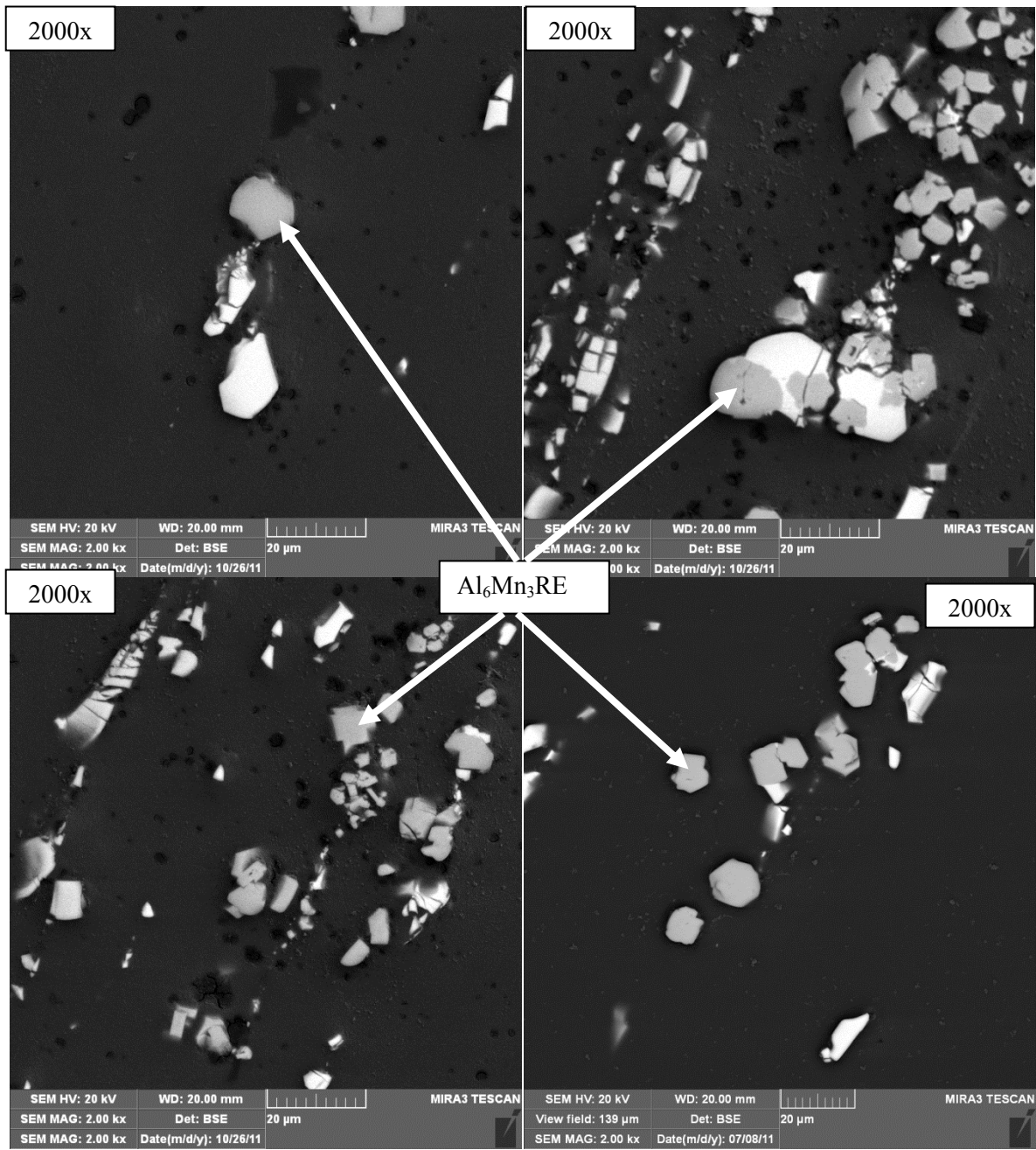


Figure 104. Structure of Al_6Mn_3RE in the as-extruded AE42 alloy

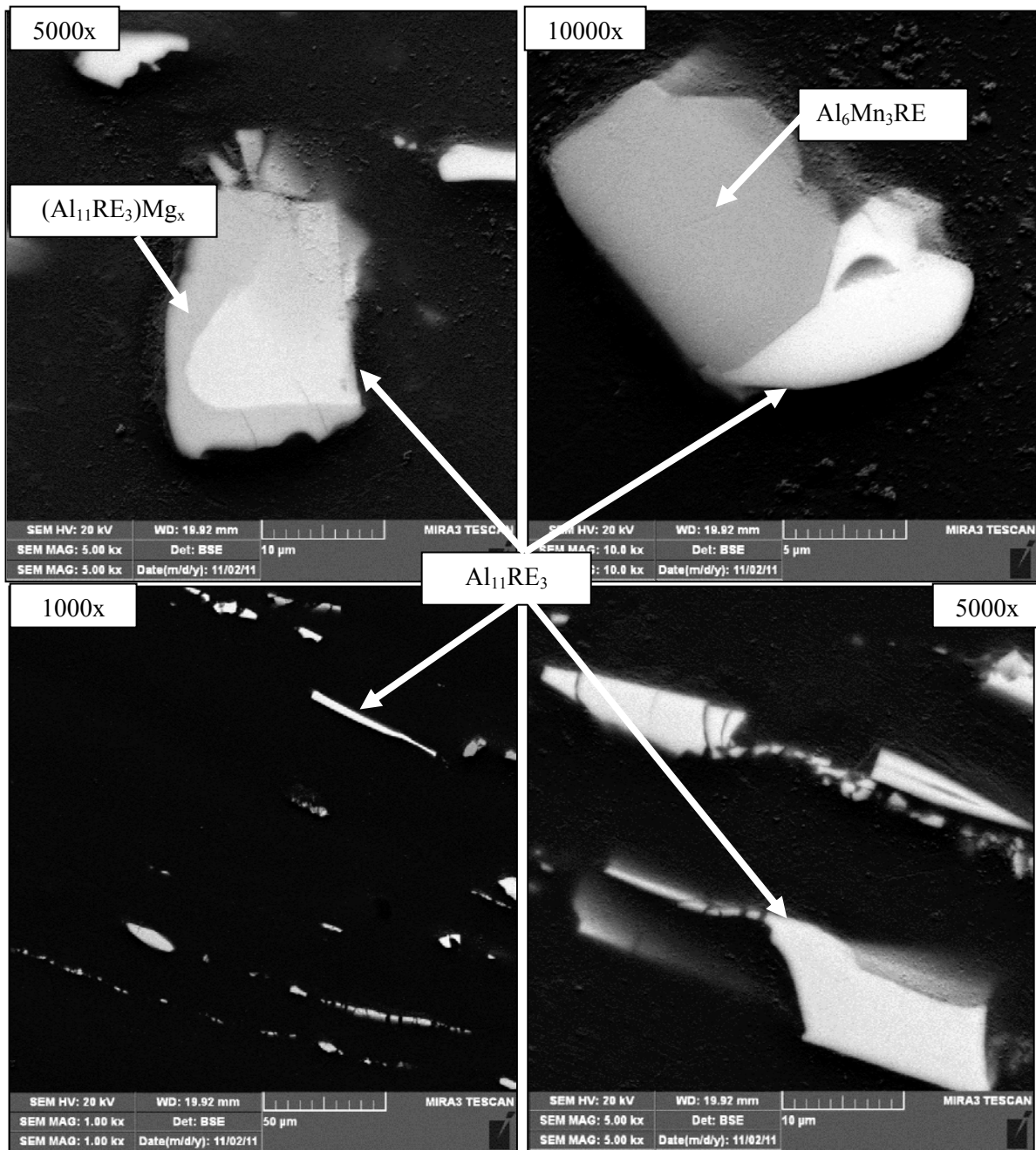


Figure 105. Structure of the post-creep intermetallics in the AE42 alloy

Appendix C.2.3 – AJ32 Alloy Intermetallics

Five distinct intermetallic compounds were identified in the AJ32 alloy. Micrographs showing the general structure of these intermetallics in the as-extruded and post-creep AJ32 alloy are provided below.

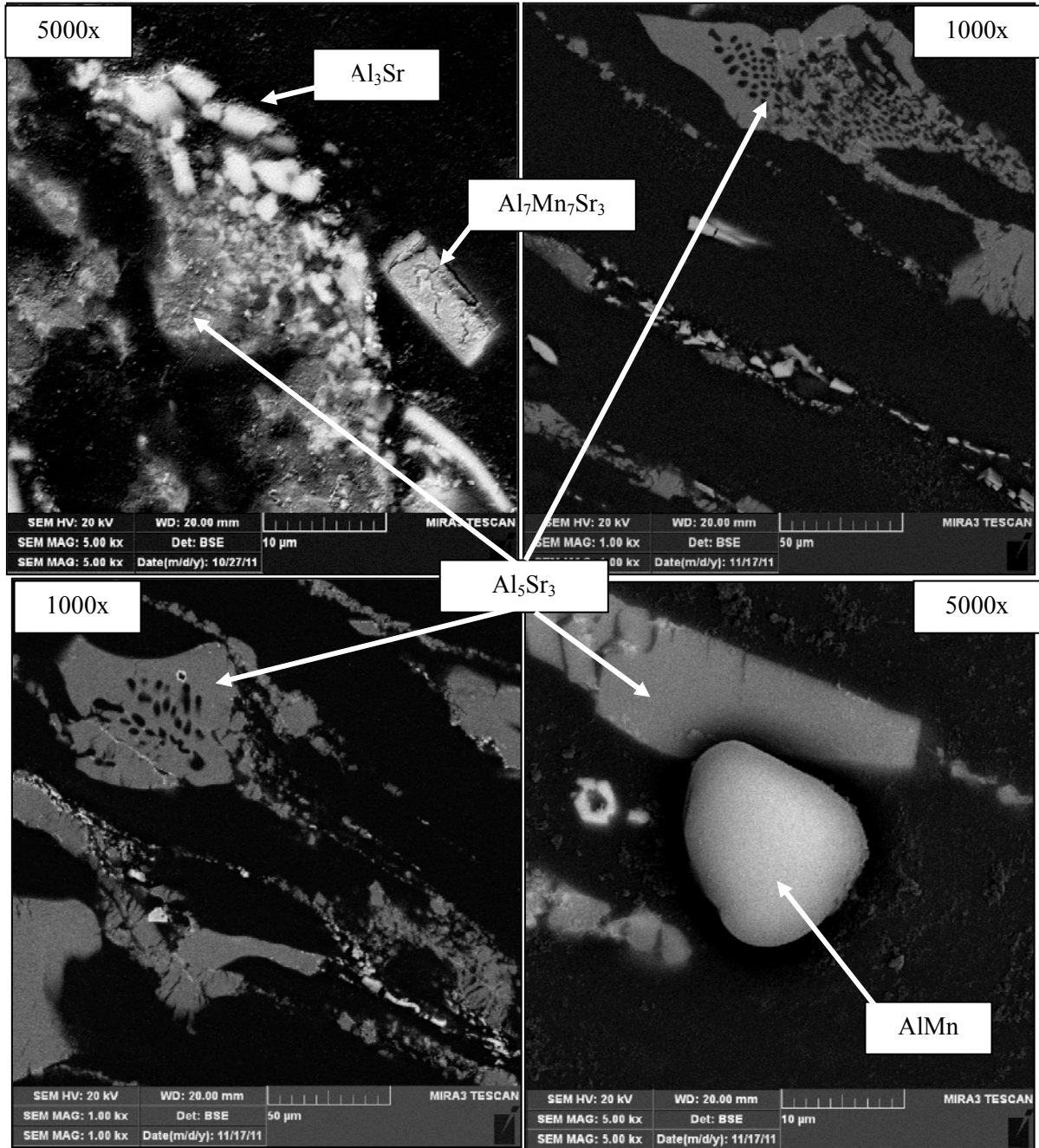


Figure 106. Structure of the as-extruded intermetallics in the AJ32 alloy

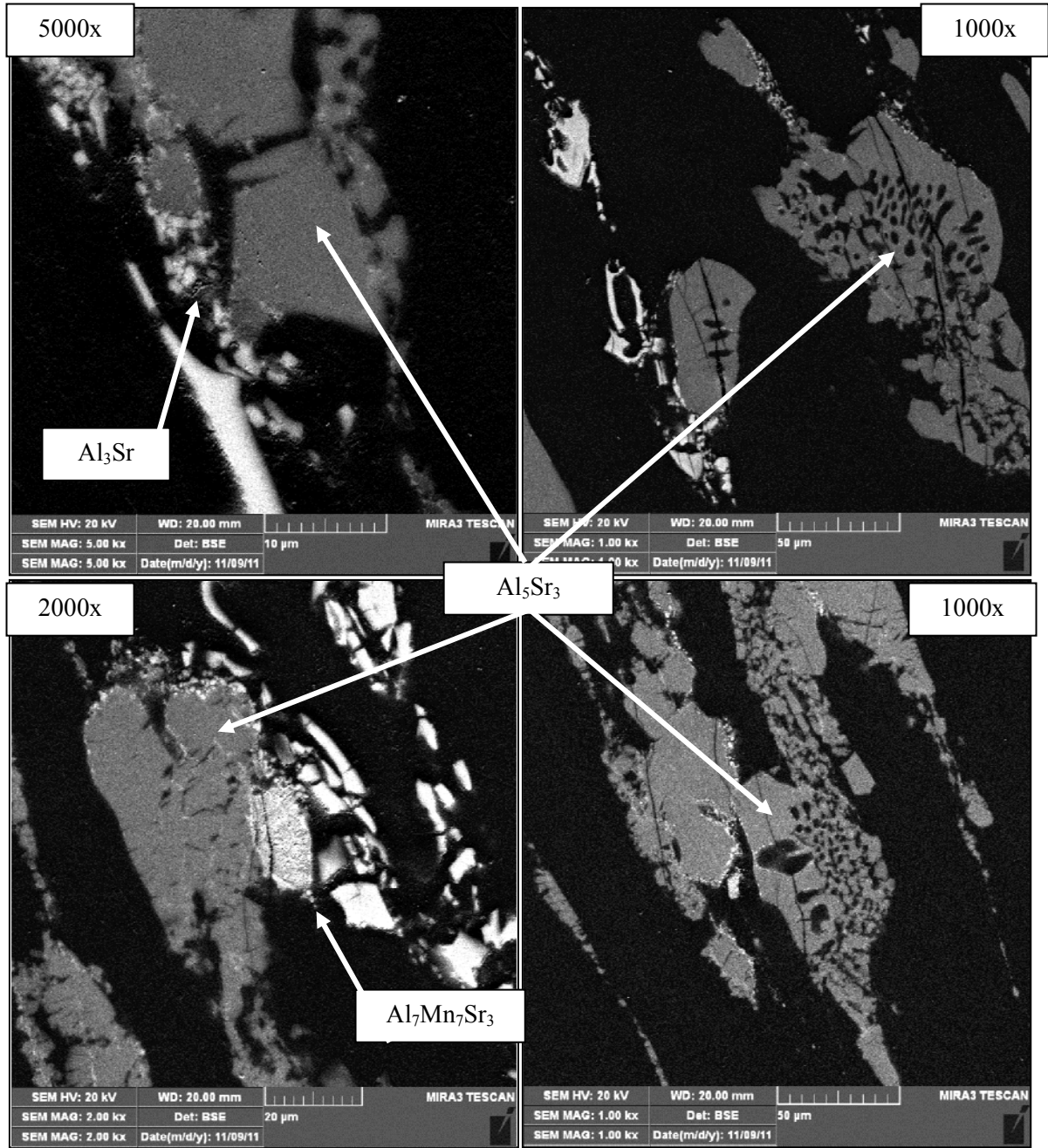


Figure 107. Structure of the post-creep intermetallics in the AJ32 alloy

Appendix C.2.4 – ZE10 Alloy Intermetallics

Four intermetallic compounds were found in the ZE10 alloy. Micrographs showing the general structure of the three most common intermetallics are provided in the as-extruded and post-creep ZE10 alloy below.

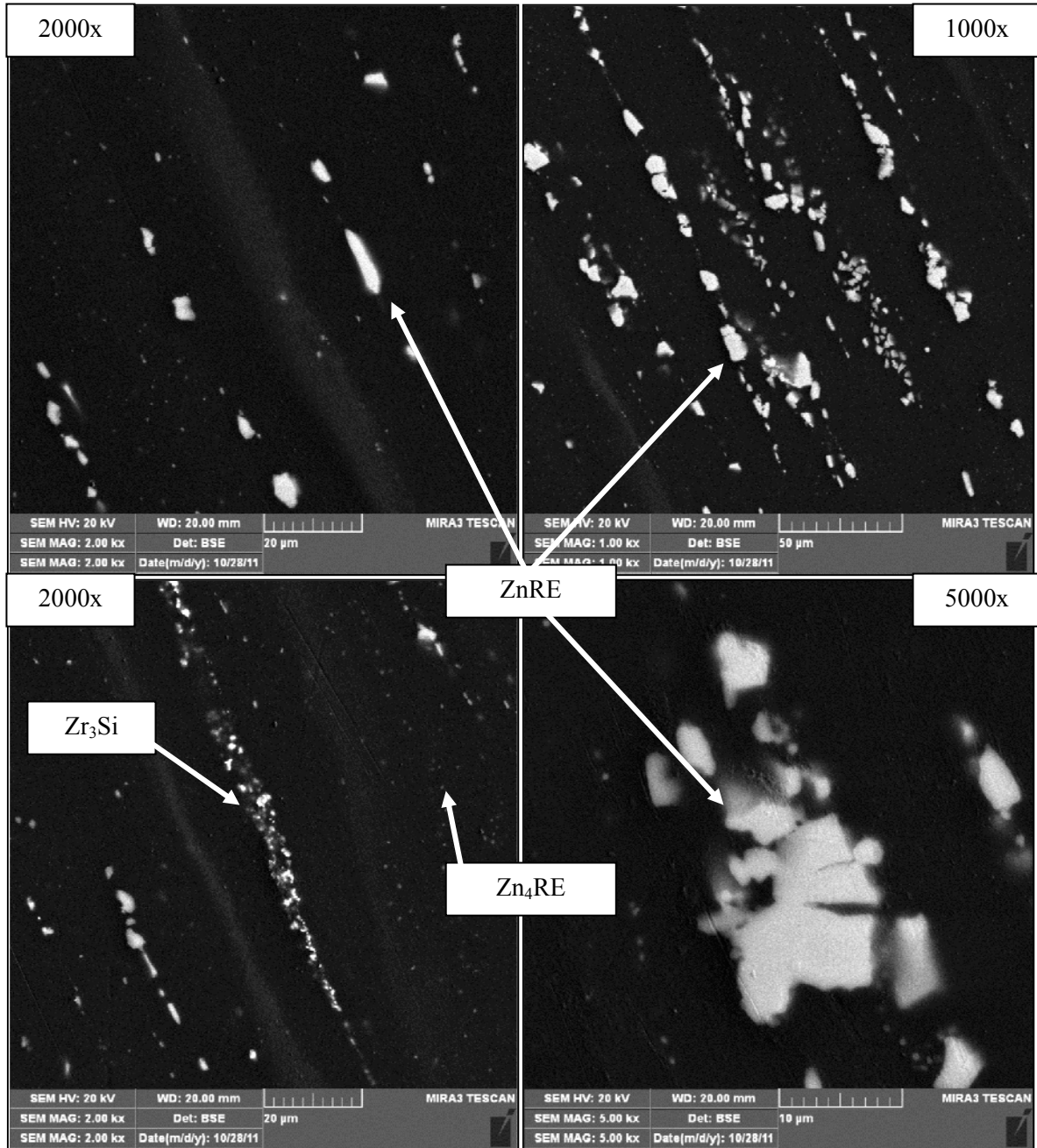


Figure 108. Structure of the as-extruded intermetallics in the ZE10 alloy

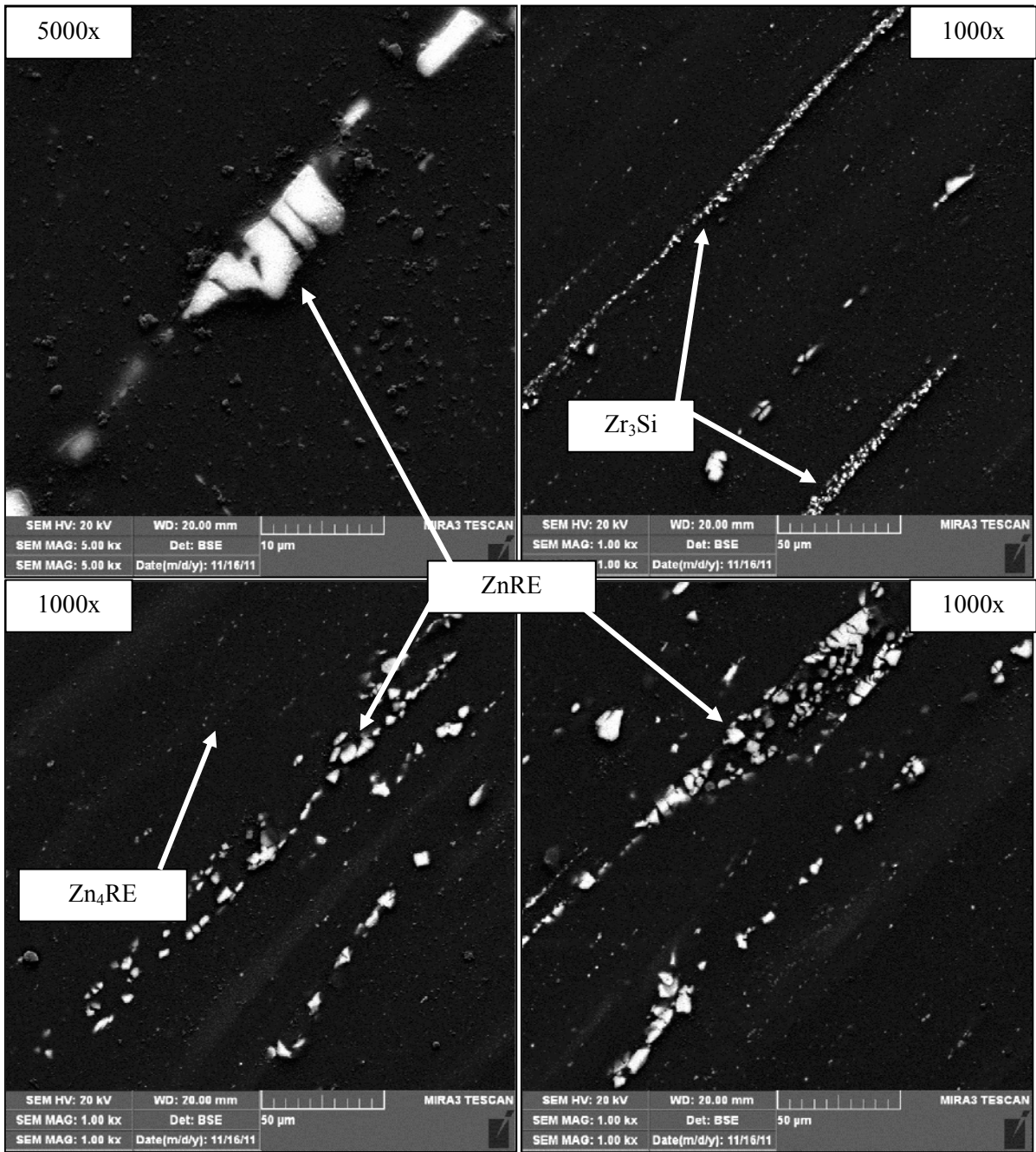


Figure 109. Structure of the post-creep intermetallics in the ZE10 alloy